Studies of Photoelectric Signals and Molecular Features of Bacteriorhodopsin and Electric-field Induced Patterns on Polymer Surfaces

A Thesis

Submitted For the Degree of

Doctor of Philosophy

by

Arun. N

Chemistry and Physics of Materials Unit
Jawaharlal Nehru Centre for Advanced Scientific Research
Bangalore – 560 064

JULY 2009

To my family & The 'Almighty'

DECLARATION

I hereby declare that the matter embodied in the thesis entitled "**Studies of Photoelectric Signals and Molecular Features of Bacteriorhodopsin**
and
Electric-field Induced Patterns on Polymer Surfaces" is the result of investigations carried out by me at the Chemistry and Physics of Materials Unit, Jawaharlal Nehru Centre for Advanced Scientific Research, Bangalore, India under the supervision of Prof. K. S. Narayan and that it has not been submitted elsewhere for the award of any degree or diploma.

In keeping with the general practice in reporting scientific observations, due acknowledgement has been made whenever the work described is based on the findings of other investigators.

Arun. N

CERTIFICATE

I hereby certify that the matter embodied in this thesis entitled "**Studies of Photoelectric Signals and Molecular Features of Bacteriorhodopsin**
and
Electric-field Induced Patterns on Polymer Surfaces" has been carried out by Mr. Arun. N at the Chemistry and Physics of Materials Unit, Jawaharlal Nehru Centre for Advanced Scientific Research, Bangalore, India under my supervision and that it has not been submitted elsewhere for the award of any degree or diploma.

Prof. K. S. Narayan
(Research Supervisor)

Acknowledgements

I am deeply indebted to ***Prof. K. S. Narayan***, my research supervisor for his constant support and guidance. I am grateful for his invaluable suggestions and discussions. His ability to push the limits of understanding and to constantly innovate has shaped my perspective of how to approach a scientific problem. He showed me different ways to approach a research problem and the need to be persistent to accomplish any goal. Also, I would like to thank his family for their moral support and wonderful hospitality.

I would like to thank *Prof. C. N. R. Rao*, for providing such wonderful facilities. His presence is a constant source of inspiration for me.

I am thankful to *Prof. Ashutosh Sharma* (IIT Kanpur), *Prof. Vijay Shenoy* (IISc) for useful and enlightening discussions and their guidance for solving problems. Special thanks to *Prof. Shenoy* specially for helping me out during my difficult times.

I would also like to thank *Prof. D. Cahen* and *Prof. M. Sheves* of Wiezmann Institute, Israel for providing me an opportunity to work in their lab for two months and *Prof. M. Sheves* for providing wild-type bR samples.

I thank all the CPMU faculty, TSU faculty and IISc faculty for their wonderful courses and general discussions.

I thank all my labmates - past and present: Dr. A. G. Manoj, Dr. S. Dutta, Dr. D. Kabra, Dr. D. Gupta, Manu, Sachi, Monojit, Shruti, Anshuman, Vini, Hemant, Jasmeet, Basavaraj, Satish, Radha, Dr. Balraju, Arun Rao, Dr. Bhatia, Shriram, Ankit and Sajini for providing a wonderful working atmosphere in the lab and with whom I have had many fruitful discussions.

I wish to convey my gratitude to all my friends in JNCASR, IISc and

other friends for their support, encouragement, discussions (both scientific and non-scientific) and making my stay enjoyable.

I would like to thank all the Technical, Academic, Administrative & Complab staff for their help during my stay here.

To my father, and my wife *Gayatri*, I thank you for always being there for me, enabling me to be who I am and where I am today. You have been the constant source of love, support and encouragement, which makes everything possible. A special thanks to my grandmom, who really wanted me to succeed in all of my endeavours.

Synopsis

The topics covering the optical activity, photoelectric signals and the effect of local electrostatic environment on the photophysical activity of a protein - retinal complex, Bacteriorhodopsin (bR) are described in the first half of the thesis. The response of soft polymeric films to an applied electric field leading to a surface deformation is described in the latter part of the thesis. The thesis concludes with a section describing the electric field induced deformation of a liquid alloy droplet as soft electrical contacts for studing electrical properties of bR films.

The first part involves the measurement of photoelectric signals from bR in mono- and multi-layer forms. Observation of photoelectric signals forms a direct evidence of the bR functionality. Photoelectric signals from monolayers of bR on conducting polymers in two terminal liquid cells were measured and correlated to the photoinduced process occurring within bR. Local photoelectric measurements were done using wide-field photocurrent imaging to provide insight on the functionality of a single monolayer patch. Further, photoelectric signals from dried bR patches were studied by fabricating a three terminal device, with two lateral electrodes across the polymer (PEDOT:PSS or PANI:DBSA) layer and multilayers of bR in the central region. The underlying polymer becomes electronically active upon photoexcitation of the bR region with the spectral and temporal characteristics of the signal corresponding to that of the bR molecule. The changes in conductance of the underlying polymer layer were correlated to the various doping processes. The temporal features across the lateral electrodes were attributed to the light-induced dipole fluctuations within bR that gets translated as local conductance changes in the polymer layer. In case of underlying polyaniline

(PANI:DBSA) films, which can be doped by protonic acids, a resistive increase in the current was observed. This was attributed to transient doping of the polymer surface by the bR-protons.

The next section involves, bR in the form of PM can be organized as patches with a large areal coverage on specifically treated substrates. Individual bR molecules within the patch are observed to be functionally active. The optical properties of the monolayers of bR oriented on different substrates such as quartz and conducting polymers were studied. The optical activity of a bR monolayer was probed by near-field microscopy in the transmission mode. In aperture based near-field microscopy, sample is typically illuminated via a small aperture (100 nm) which can provide an optical resolution in the scale of $\sim$ 40 nm. Optical constants were estimated from these single molecule measurements and were found to be higher than the bulk measurements. These single molecule effects were attributed to an additional interaction between the near-field and the transition dipole moment of the retinal chromophore. Upon, introducing an additional pump (corresponding to the excited state absorption) on the probing region, the absorption corresponding to the probe-wavelength is enhanced. This increased absorption was attributed to the dynamics of the photocycle and the quantum efficiencies of the photoconversion process. Further, the effect of local electrostatic environment on the optical activity and photocycle of bR were greatly modified when these protein molecules were oriented on a thin layer of polyaniline. Using this method of pump-probe near-field microscopy, the changes in bR optical activity and photocycle were followed.

The latter part deals with electric-field induced effects on polymer films, whose viscosity and elasticity was modified from a viscous like to elastic solid like films. Upon, application of electric field in parallel plate geometry, the film surface deformed to give patterns which characteristic hexagonal ordering whose wavelength depended on various factors. For viscous films, the wavelength depended on the applied electric field and the surface tension whereas for solid like films, the wavelength was found to be independent of the applied electric field as long as it was above the critical value. For higher shear moduli films, inclined plane geometry was used to study the electric

field induced deformation. The competition between the elastic strain energy and the van der waals interactions gives rise to a fingering pattern at the contact zone prior to the application of electric field. The distinct electric field induced morphological changes, leading to the formation of two-dimensional hexagonally arranged pillars, large-amplitude fingers, and straightening of contact edge were studied comprehensively.

The last chapter deals with deformation of a liquid alloy when an electric field was applied and this deformed alloy was used as contacts to measure the bR photoelectric signals. The thesis concludes with a brief summary and a section on future outlook.

List of Publications

N. Arun and K. S. Narayan, "Conducting Polymers as Antennas for Probing Biophysical Activities" Journal of Physical Chemistry B, **112**, 1564-1569 (2008).

N. Arun and K. S. Narayan, "Monitoring Intermediate States of Bacteriorhodopsin Monolayers using Near-field Microscopy" Submitted

N. Arun, Ashutosh Sharma, Vijay. B. Shenoy and K. S. Narayan, "Electric-Field-Controlled Surface Instabilities in Soft Elastic Films" Advanced Materials, **17**, 660-663 (2006).

N. Arun, Ashutosh Sharma, Partho S. G. Pattader, Indrani Banerjee, Hemant M. Dixit, and K. S. Narayan, "Electric field Induced Patterns in Soft Visco-elastic films: From Long Waves of Viscous Liquids to Short Waves of Elastic Solids" Physical Review Letters, **102**, 254502 (2009).

N. Arun, J. Sarkar, Ashutosh Sharma, V. B. Shenoy and K. S. Narayan, "Electric-Field Induced Morphological Transitions in Elastic Contact Instability of Soft Solid Films" Journal of Adhesion, **83**, 513-534 (2007).

M. Bag, D. Gupta, **N. Arun** and K.S Narayan, "Deformation of metallic liquid drop by electric field for contacts in molecular-organic electronics" Proceedings of The Royal Society A, **465**, 1799-1808 (2009).

List of Figures

Contents

Chapter 1

General Introduction

In this thesis, two research problems have been addressed. The first problem concerns the study of optical activity, photoelectric signals, molecular features and SNOM properties of a model protein, bacteriorhodopsin (bR), a light-driven proton translocator. These properties were greatly modified in the presence of a conducting polymer substrate.

The second problem described in the latter part of the thesis focuses on the effect of electric field on soft polymer films. The application of electric field modified the surface leading to the formation of a a wide variety of structures. The characteristic length scales of the morphological patterns depend on the elastic storage moduli of the films, while the dynamics of the response depend on the rheological parameters.

The understanding of these electric field induced patterns was adopted for droplets of soft metallic alloys, that deform upon the application of the electric field. These alloys were utilized as electrodes for bR-based devices to study the photoelectric signals.

The problem involving bR utilizes features of conducting polymers to study and modify its optical and photoelectric signals. Both systems, bR and conducting polymers (CP) have been extensively studied and well understood. A short introduction to the relevant aspects of conducting polymers, bacteriorhodopsin and optical microscopy is provided in the subsequent sections.

1.1 Conducting Polymers

In conjugated polymers, the chemical bonding (sp^2p_z) leads to one unpaired electron (the π electron) per carbon atom [1]. The p_z orbitals of successive carbon atoms along the backbone overlap, leads to electron delocalization along the backbone of the polymer. This electronic delocalization provides the route for charge movement along the backbone of the polymer chain. The classic example of such a polymer is polyacetylene, $(\text{-CH})_n$, in which each carbon is σ bonded to only two neighboring carbons and one hydrogen atom with one π electron on each carbon along the p_z orbital. However, the structure is dimerized primarily as a result of the Peierls instability with two carbon atoms in the repeat unit, $(\text{CH=CH})_n$ leading to an energy gap, E_g between the filled π and unfilled π^* bands. The bond-alternated structure of polyacetylene is characteristic of conjugated polymers (Fig. 1.1). Consequently, since there are no partially filled bands, pristine conjugated polymers are typically semiconductors [2].

The impact of the field of conjugated polymers on science in general was recognized by the awarding of the Nobel Prize for Chemistry in 2000, to the

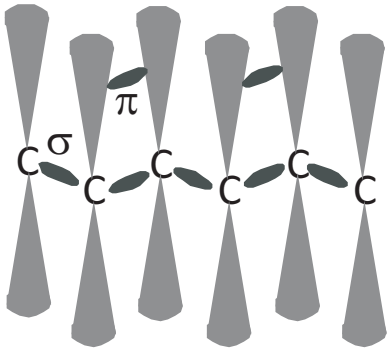

Figure 1.1: *sp^2 hybdridised carbon atoms with the presence of additional π conjugation due unhybridised p_z orbitals.*

three discoverers of conducting polymers: Alan MacDiarmid, Alan Heeger and Hideki Shirakawa.

1.1.1 Electronic Properties

The charge carriers in conjugated polymers have been interpreted in terms of localized excitation, which are quasi-particles with structural deformation over several repeat units. These excitations, classified mainly as (i) Solitons [3, 4] (ii) polarons [5] and bipolarons [6], contribute to charge transport in different cases.

(a) Solitons

Charge storage on the polymer chain leads to structural relaxation, which in turn localizes the charge. The simplest example of this structural relaxation is the soliton in trans-polyacetylene. The soliton can be considered as a domain boundary between the two possible degenerate ground-state configurations of trans-(-CH=CH-)$_N$, the "A" Phase and the "B" Phase. For simplicity, the chemical structure of the soliton was drawn as an abrupt

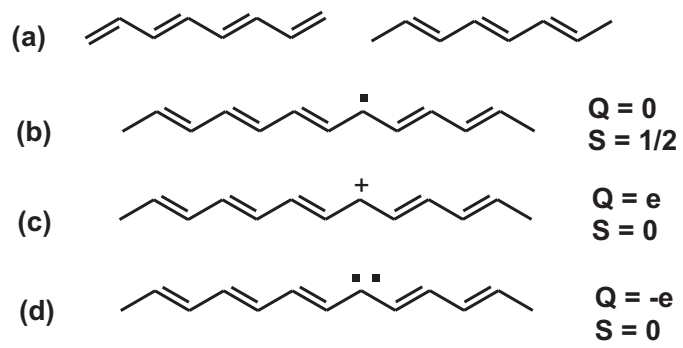

Figure 1.2: *Trans-polyacetylene. (a) Degenerate A and B phases. (b) Neutral, (c) Positive and (d) Negative solitons in trans-polyacetylene.*

change from A Phase to B Phase (Fig. 1.2). But, the structural relaxation in the vicinity of the domain boundary extends over approximately seven carbon atoms as observed from various experiments and theoretical calculations. The corresponding spin and charge distributions are similarly delocalized.

The localized electronic state associated with the soliton is a non-bonding state at an energy which lies at the middle of the π - π^* gap, between the bonding and anti-bonding levels of the perfect chain. On the other hand, the defect is both topological and mobile because of the translational symmetry of the chain [3,4,7]. If the state is unoccupied (doubly occupied), the carbon atom at the boundary is left with a positive (negative) charge, but there are no unpaired spins; the charged soliton is positively (negatively) charged and spinless. Single occupation of the soliton state neutralizes the electronic charge of the carbon nucleus, while introducing an unpaired spin onto the chain.

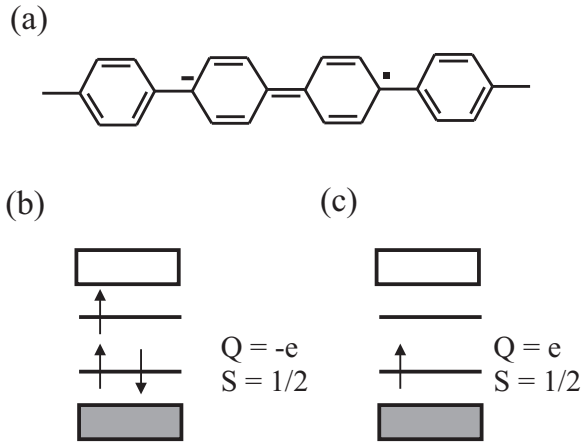

Figure 1.3: *(a) Schematic picture of a polaron in PPP. Band diagram of (b) electron polaron and (c) hole polaron.*

(b) Polarons and Bipolarons

In cases, such as poly(thiophene), poly(phenylene vinylene), poly(para-phenylene) and cis-polyacetylene, where the two possible bond-alternation structures are not energetically degenerate, polarons, and bipolarons, are the stable non-linear excitation and the charge-storage states [8]. A polaron can be thought of as a bound state of a charged soliton and a neutral soliton whose mid-gap energy states hybridize to form bonding and antibonding levels. The neutral soliton contributes no charge and a single spin and the charged soliton carries charge of ±e and no spin; the resulting polaron then has the usual charge-spin relationship; q=±e and s=1/2. The polaron in PPP is illustrated schematically in Fig. 1.3. The positive (negative) polaron is a radical cation (anion), a quasi-particle consisting of a single electronic charge dressed with a local geometrical relaxation of the bond lengths.

Similarly, a bipolaron is a bound state of two charged solitons of like

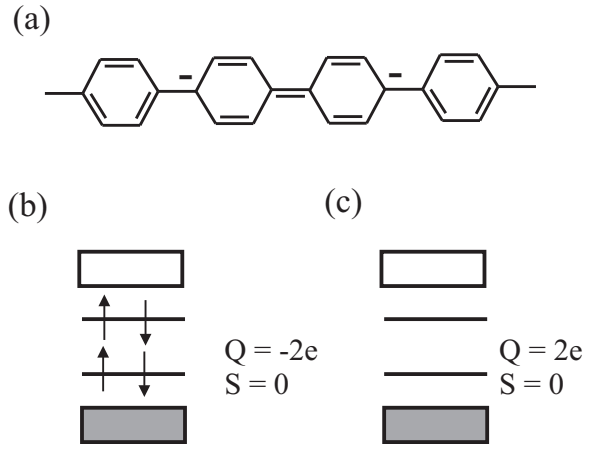

Figure 1.4: *(a) Schematic picture of a negative bipolaron, Bond diagram for (b) negative bipolaron and (c) positive bipolaron.*

charges (or two polarons) with two corresponding mid-gap levels, as illustrated in Fig. 1.4. Since each charged soliton carries a single electronic charge and no spin, the bipolaron has charge ±2e and zero spin. The positive (negative) bipolaron is a spinless dication (dianion); a doubly charged bound state of two polarons bound together by the overlap of a common lattice distortion (enhanced geometrical relaxation of the bond lengths).

1.1.2 Doping

Doping [i.e., addition (or withdrawal) of electrons to (or from) the conjugated chains] is the central process that governs the main properties of conducting polymers (CPs), in particular the crossover from an insulating to a conducting state [9]. Reversible doping of conducting polymers, with associated control of the electrical conductivity over the full range from insulator to metal, can be accomplished by various means: (1) Chemical doping, (2)

Electrochemical doping, (3) Photo-doping and (4) Charge injection at interface. Concurrent with the doping, the electrochemical potential (the Fermi level) is moved either by a redox reaction or an acid-base reaction into a region of energy where there is a high density of electronic states; charge neutrality is maintained by the introduction of counterion into the polymer matrix [1]. The electrical conductivity results from the existence of charge carriers (through doping) and from the ability of those charge carriers to move along the π-bonded network. Consequently, doped conjugated polymers are good conductors for two reasons [1]:

(i) Doping introduces carriers into the electronic structure. Since every repeat unit is a potential redox site, conjugated polymers can be doped n-type (reduced) or p-type (oxidized) to a relatively high density of charge carriers [10].

(ii) The attraction of an electron in one repeat unit to the nuclei in the neighboring units leads to carrier delocalization along the polymer chain and to charge-carrier mobility, which is extended into three dimensions through interchain electron transfer. Disorder, however, limits the carrier mobility and, in the metallic state, limits the electrical conductivity. Indeed, research directed toward conjugated polymers with improved structural order and hence higher mobility is a focus of current activity in the field.

(a) Chemical Doping

The initial discovery of the ability to dope conjugated polymers involved charge-transfer redox chemistry; oxidation (p-type doping), or reduction (n-type doping), [10–12] as illustrated with the following examples:

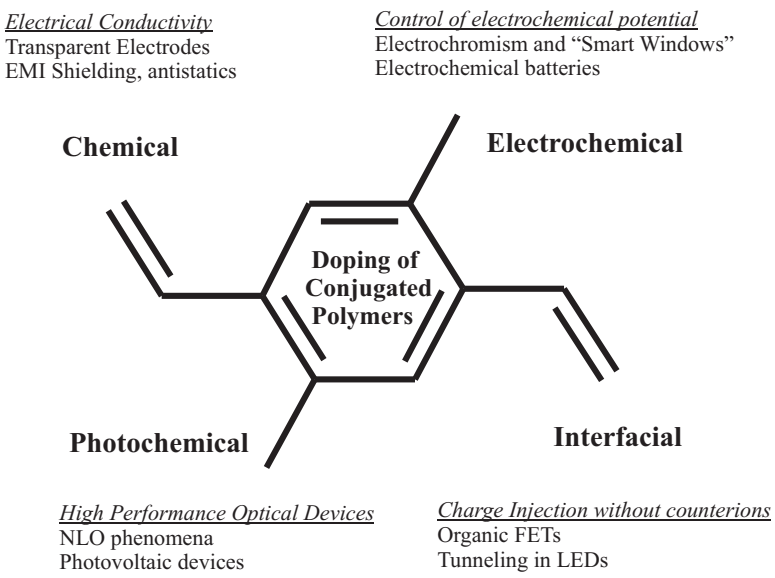

Figure 1.5: *Doping mechanisms and related applications as adapted from A. J. Heeger,* ***Rev. Mod. Phys.****, 2001, 73, 681.*

a) p-type doping by

$$(\pi - polymer)_n + 3/2ny(I_2) \rightarrow \left[(\pi - polymer)^{+y}(I_3^-)_y\right]_n \qquad (1.1)$$

b) n-type doping

$$(\pi - polymer)_n + \left[Na^+(C_{10}H_8)^-\right]_y \rightarrow \left[(Na+)_y(\pi - polymer)^{-y}\right]_n + (C_{10}H_8)^0 \qquad (1.2)$$

When the doping level is sufficiently high, the electronic structure evolves to that of a metal.

Both p-type and n-type doping have been obtained in CPs. Generally, however, p-doping leads to more stable compounds. In the case of n-doping

the dopants are alkali metals, which are unstable in air atmosphere. Furthermore, oxygen can act as an oxidant and neutralize n-doping. Even p-doping can be unstable in air if the oxidation potential of the polymer is higher [9].

(b) Electrochemical Doping

In electrochemical doping, the electrode supplies the redox charge to the conducting polymer, while ions diffuse into (or out of) the polymer structure from the nearby electrolyte to compensate the electronic charge. The doping level is determined by the voltage applied between the conducting polymer and the counter electrode; at electrochemical equilibrium the doping level is precisely defined by that voltage. Thus, doping of any level can be achieved by setting the electrochemical cell at a fixed applied voltage and waiting for the system to come to electrochemical equilibrium (as indicated by the current through the cell going to zero). Electrochemical doping is illustrated by the following examples [13–15]:

a) p-type doping

$$(\pi - polymer)_n + \left[Li^+(BF_4^-)\right]_{soln} \rightarrow \left[(\pi - polymer)^{+y}(BF_4^-)_y\right]_n + Li_{electrode} \tag{1.3}$$

b) n-type doping

$$(\pi - polymer)_n + Li_{electrode} \rightarrow \left[(Li^+)_y(\pi - polymer)^{-y}\right]_n + \left[Li^+(BF_4^-)\right]_{soln} \tag{1.4}$$

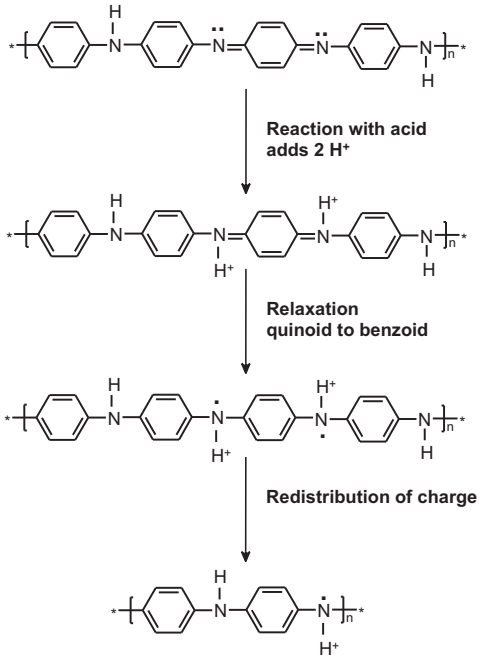

Figure 1.6: *Doping mechanism in polyaniline with the addition of acids, adapted from Macdiarmid et. al.,* ***Synth. Met.****, 1987, 18, 285.*

(c) Protonic Doping

A method of doping, specific to polyaniline, is "protonic" doping. In this case, the doping consists of a proton addition to the polymer chain with no change in the total number of electrons [16–18]. It was shown at that time that protonation of polyaniline in the emeraldine base form resulted in a tremendous increase in conductivity. The addition of a proton (to the imine nitrogen) acts as a trap for one of the two electrons of the nitrogen doublet. Thus, the number of electrons effectively available for the delocalized π-molecular orbitals diminishes. The Fermi level is then shifted and leads to a transition to the conducting state.

(d) Photo-doping & Charge Injection

The semiconducting polymer can be locally oxidized and reduced by photo-absorption and charge separation (electron-hole pair creation and separation into "free" carriers). The photogeneration process takes place primarily via an intermediate state, called the *exciton*, which is a quasi-particle consisting of an electron-hole pair with a finite binding energy. Photoinduced charge transport in semiconducting polymers follows: (i) exciton formation, (ii) exciton diffusion, (iii) exciton dissociation and finally (iv) transport of charge carriers to the respective electrodes.

Electrons and holes can be injected from metallic contacts into the π^* and π bands, respectively. In the case of charge injection at a metal-semiconducting (MS) polymer interface, the polymer is oxidized or reduced (electrons are added to the π^* band or removed from the π band). However, the polymer is not doped in the sense of chemical or electrochemical doping, for there are no counter ions.

1.1.3 Transport Mechanism

In a perfect crystal with periodic potentials, electron wavefunctions form delocalized Bloch waves. Impurities and lattice defects in disordered systems introduce backward scattering of these electron waves with resulting "Anderson localization" [19]. Even though there is a high density of conduction electrons at the Fermi level for the highly doped state, the carriers may be spatially localized due to the nanoscale disorder, so the carriers cannot participate in transport except through hopping [20–24].

When the Fermi level lies in the localized region, the conductivity at zero temperature is zero even for a system with a finite density of states. The Mott variable range hopping (VRH) [25] model is applicable to systems with strong disorder such that the disorder energy is much greater than the bandwidth. The general form of the temperature-dependent conductivity σ in Mott's model is described as

$$\sigma = \sigma_0 exp\left[-(T_0/T)^{1/(d+1)}\right] \tag{1.5}$$

where d is the dimensionality and for three-dimensional systems,

$$\sigma = \sigma_0^{3d} exp\left[-(T_0^{3d}/T)^{1/4}\right] \quad and \quad T_0^{3d} = c/(k_B N(E_F) L^3) \tag{1.6}$$

where c is the proportionality constant, k_B is the Boltzmann constant, L is the localization length, and σ_0 is a temperature (T) independent or weakly-temperature dependent prefactor. Eqn. 1.5 for $d = 1$ corresponds to the behaviour of quasi-one-dimensional variable range hopping (Q1D-VRH) for the circumstance where the charge carriers primarly hop along a "one-dimensional" chain and occasionally hop to a nearest-neighbour chain thereby avoiding energetically large barriers.

While, variable range hopping mechanism can be used to emperically describe the temperature dependence of conductivity for lightly to moderately doped conjugated polymers. For, highly doped polymers, the model of 'fluctuation-induced tunneling' introduced by Sheng [26] is more appropriate.

In that model, the material is considered a heterogeneously conducting system consisting of large highly conducting regins separated by potential

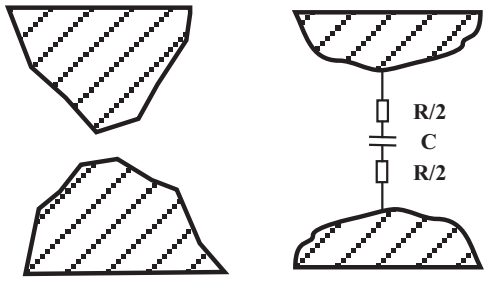

Figure 1.7: *A region of close approach between two conducting segments. Shaded area denotes conductor. In (a), the lines delineate the surface areas within which most of the tunneling occurs. This tunnel junction is is schematically depicted as a parallel-plate capacitor in (b), adapted from P. Sheng,* ***Phys. Rev. B.****, 1980, 21, 2180.*

barriers (Fig. 1.7). In the low temperature limit, a crossing of potential barriers is possible only due to quantum mechanical tunneling, leading to a finite value of the electrical conductivity. For the limit of high temperatures, thermally activated crossing of the barriers is possible, leading to an Arrhenius-type temperature dependence of σ with a saturation value [27].

$$\sigma(T) = \sigma_0 exp(-\frac{T_1}{T_0 + T}) \tag{1.7}$$

leading to the upper and lower boundary values:

$$\sigma(T \to \infty) = \sigma_0 \tag{1.8}$$

$$\sigma(T \to 0) = \sigma_0 exp(T_1/T_0) \tag{1.9}$$

1.1.4 Examples

Conducting polymers such as polypyrrole, polythiophene and polyanilines are complex dynamic structures whose properties can be modified to the needs of the applications. In this thesis, a modified form of thiophene, poly(3,4-ethylenedioxythiophene) (PEDOT) and polyanilines have been extensively used. A brief introduction for these polymers is given below.

(a) PEDOT:PSS

The polythiophene derivative, poly(3,4-ethylenedioxythiophene) (PEDOT) (Fig. 1.8) was originally designed to give a stable conducting polymer [28], from the point that chemical attack on the conjugated carbons (lacking the undesired α,β- and β,β-couplings) would be prevented by making a stable bond to the ether oxygen. Prepared using standard oxidative chemical or electrochemical polymerization methods, PEDOT was initally found to be an insoluble polymer yet exhibited some very interesting properties [29]. In addition to a very high conductivity, PEDOT was found to be almost transparent in thin, oxidized state [30–33]. The solubility problem was subsequently circumvented by using a water-soluble polyelectrolyte, poly(styrene sulfonic acid) (PSS), as the charge-balancing dopant during polymerization to yield PEDOT:PSS. This combination resulted in a water-soluble polyelectrolyte system with good film-forming properties, high conductivity, high visible light transmissivity and excellent stability.

The most practically useful, polymerization method for EDT is the so-called BAYTRON P synthesis that was develped at Bayer AG [34–37]. This

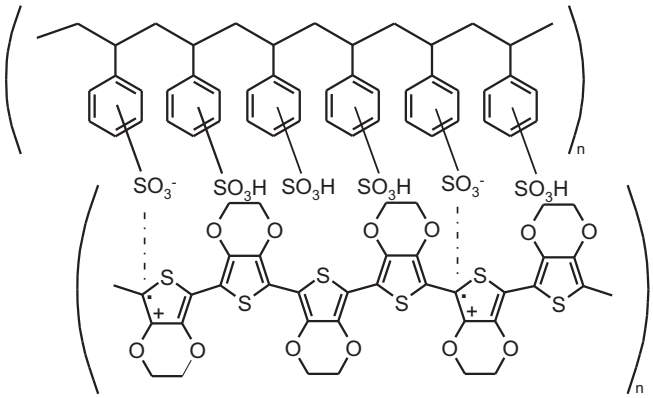

Figure 1.8: *Chemical structure of PEDOT:PSS.*

method utilizes the polymerization of EDT in an aqueous polyelectrolyte (most commonly PSS) solution using $Na_2S_2O_8$ as the oxidizing agent. Carrying this reaction at room temperature results in a dark blue, aqueous PEDOT:PSS dispersion, which is commercially available from Bayer AG under its trade name BAYTRON P (Fig 1.8). Even after drying, the remaining PEDOT:PSS film is highly conducting, transparent, mechanically durable, and insoluble in any common solvent [29].

Films cast from aqueous PEDOT:PSS solution have a high degree of mechanical integrity with conductivities ranging from 1 and 10 S/cm. These films are highly stable and can be treated for up to 1000 h at 100 °C with no change in conductivity. Secondary doping in PEDOT:PSS can be achieved by adding high-boiling point polyalcohol (sorbitol, glycerol, m-cresol, ethylene glycol). This polyalcohol aids the reorientation of the PEDOT:PSS chains to form better connections between the conducting PEDOT chains [38]. This conformational change results in the enhancement of charge-carrier mobility in the film and leads to an enhanced conductivity by two orders of magnitude

(100 - 1000 S/cm). It is a low bandgap material, with the gap in the visible-near infrared (NIR) transition region and shows an absorption maximum in the middle of the visible spectrum at 2.2 eV (600 nm), while neutral form has two absorption peaks, at 580 and 630 nm.

PEDOT:PSS has been extensively studied as the active material in lateral electrochemical diodes, triodes and transistors [39], as the charge injecting and extracting layer in organic light-emitting diodes [40] and organic solar cells [41], and as electrodes in organic field-effect transistors [42] and for various sensing activities.

(b) Polyaniline

Polyaniline (Pani) have been known for more than a century, since the synthesis of the so-called "aniline blacks". It differs from other conducting polymers in that it possesses three readily accessible oxidation states. These range from the fully reduced (y = 1) *leucoemeraldine* state to the half oxidized (y = 0.5) *emeraldine* form to the fully oxidized (y = 0) *pernigraniline* state (Fig. 1.9). The *leucoemeraldine* base form can be *p*-doped (oxidatively doped), the *emeraldine* base form can be protonic acid doped and the *pernigraniline* base form can be *n*-doped (reductively doped) to form conducting systems. These polyanlines are most commonly prepared through the chemical or electrochemical oxidative polymerization of the respective aniline monomers in acidic solution. Pani is unique among inherently conducting polymers in that it can be rapidly converted between base and salt forms by treatment with base or acid (Fig. 1.6).

The colours and UV-Vis absorption peaks of the various polyaniline films

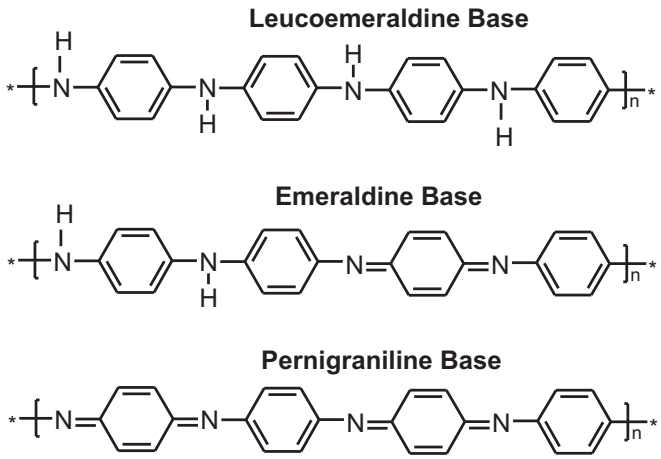

Figure 1.9: *Chemical structures of the different forms of Polyaniline.*

is summarized in Table below.

Polyaniline	**Colour**	λ_{max} **(nm)**
Emeraldine Salt	green	350, 430 and 810
Emeraldine Base	blue	340 and 620
Leucoemeraldine Salt	colourless	300
Leucoemeraldine Base	pale yellow-green	320
Pernigraniline Salt	blue	350 and 690
Pernigraniline Base	violet	340 and 540

Table 1.1: *Colours and UV-Vis absorption peaks.*

Chemical synthesis has the advantage of being a simple process capable of producing bulk quantities of Pani. In chemical polymerization, the oxidizing force is supplied by a chemical oxidant in the solution. The most widely employed chemical oxidant has been aqueous ammonium persulfate, $(NH_4)_2S_2O_8$, leading to the incorporation of the dopant anions (A^-) in the Pani.HA product. Acidic conditions (pH $\leq$ 3) are usually required to assist the solubilization of the aniline in water and to avoid excessive formation of undesired branched products [43]. The nature and concentration of the

protonic acids (HA) employed during aniline polymerization with $S_2O_8{}^{2-}$ have been reported to have a significant effect on the physicochemical properties and molecular weights of the Pani.HA emeraldine salt products [43]. Similarly, dodecylbenzenesulfonic acid (DBSA) salts of aniline (dissolved in chloroform) with $(NH_4)_2S_2O_8$ (in a small amount of water) was used for polymerization to yield a homogenious green/black suspension of the emeraldine salt form of Pani.DBSA [44].

These reversible redox and pH switching properties, together with the electrical conductivity of the emeraldine salt form, its ease and cheapness of synthesis, and its good environmental stability, have led to its becoming the most extensively studied organic conducting polymer over the past decade and a wide range of potential applications are being developed.

1.1.5 Intelligent Materials

Organic electronics distinguishes itself from traditional electronics because one can define functionality at the molecular level, process the materials from solutions and make displays and circuits that are completely flexible. Semiconducting polymers have been used in a wide variety of applications such as photovoltaics, light emitting diode and organic field-effect transistors. With the aid of chemists, properties of these polymers were tuned in requirement for the above mentioned applications. While, semiconducting polymers have been found useful in traditional device applications, replacing silicon based materials, conducting polymers have found their own unique and substantially different applications in newly emerging technologies, a

few of which are discussed below.

(a) Electromechanical actuators

Electromechanical actuators are materials that can change their physical dimensions when stimulated by an electrical signal. Conducting polymer electromechanical actuators were based on large dimensional changes that result from the electrochemical doping of various conducting polymers [45]. These dimensional changes, that can more than double the volume of the polymer electrode [46], are largely due to the volume required to accomodate anions or cations, together possibly with co-intercalating species. The charge transferred between the anode and cathode is the key parameter determining the electrically generated strain, and this charge transfer depends on the applied voltage and not on the applied field [47]. A very low possible operation voltage (of the order of a few volts) provides a major advantage of the conducting polymer actuators with respect to other actuators. Some of the disadvantages of conducting polymers are a slow response time and limited lifetimes.

(b) Electrochemical Transistors

The ion to electron converting action prevalent in organic electrochemical transistors (OECTs) was demonstrated nearly two decades ago and has been utilized to sense water vapor, glucose, and deoxyribonucleic acid [48–51] Recently, various analytes were sensed with these OECTs integrated with bilayer lipid membranes [52]. The transistor action has been explained in terms of an ion-leveraged transport mechanism [53, 54] or electrochemical

processes [55, 56]. In the ion-leveraged mechanism, positively charged ions, from the solution drift into the film and disrupt hole tunnelling. This causes a metal to insulator transition which results in a decrease in conductivity. According to electrochemical mechanism, a reaction takes place leading to a reduction process, that leads to the observed decrease in conductivity. The reaction is summarized as follows:

$$PEDOT : PSS + M^{+} + e \Leftrightarrow PEDOT + M : PSS \tag{1.10}$$

where M^{+} denotes the positively charged ion and e the electron. This allows the utilization of PEDOT:PSS in smart windows both, as one of the transparent electrodes, and as the electrochromic material.

(c) Controlled release devices

Conducting polymer films and coatings are ideal hosts for controlled release of chemical substates, including therapeutic drugs [57] and many others. By incorporating the target species as the dopant in the conducting polymer, the redox chemistry can be used to release the target species at the desired time. Both anionic and cationic species can be incorporated into the polymer and released at the desired time. The release can also be automatically stimulated by a change in the environment.

(d) Cellular communications

Conducting polymers have considerable promise as coatings for electronic biomedical devices because they facilitate charge transport between the metal

electrode (an electron conductor) and living tissue (an ionic conductor) [58]. It has been shown that electrical stimuli can be used to address living cells in culture and hence stimulate and regulate growth [59]. The incorporation of proteins, enzymes and antibodies has been readily achieved. Additionally, biological factors can be incorporated into the polymer films to encourage cell interaction with the electrode surface.

(e) Electrochromics

Another interesting application that uses the dynamic properties of conducting polymers is electrochromic devices [60–64]. For example, polythiophenes and polyaniline undergo distinct colour changes when an electrical potential is applied. Thin films of polythiophene can be switched from red (oxidized) to blue (reduced), and polyaniline transcends a spectrum of colours as different potentials are applied to it. This has possible applications in advertising displays and smart windows. This bi-stable material can also be used as a memory storage device for information storage.

The above areas of application and the ability to characterize and communicate with conducting polymers using emerging technologies highlight the versatile, dynamic, yet controllable nature of these materials. The chemical, electrical and mechanical properties of these polymers can be manipulated to tailor-make them for required applications. They undoubtedly possess properties that make their use in the pursuit of intelligent materials systems or structures. These conducting polymers also serve as soft electrode substrates for anchoring and orientating functional membrane proteins. In this thesis, this property was utilized to orient bacteriorhodopsin (bR), a

membrane protein that functions as a light-driven proton pump on various conducting polymers (PEDOT:PSS, PANI:HCl and PANI:DBSA).

1.2 Bacteriorhodopsin (bR)

Nature has optimized the binding sites of the retinal-based light transducing proteins to provide highly efficient bond-specific photochemistry. The rhodopsins and the cone pigments of the vertebrate and invertebrate photoreceptors have been optimized through evolution to select for and enhance the efficiency of the photochemical process. Bacteriorhodopsin (bR) from the archaen *Halobacterium salinarum* was discovered in 1966. It was recognized as a rhodopsin-like protein in 1970 and its function as an electrogenic, light-driven proton pump was established at 1972 [65]. The purple membrane, which contains the protein bR in a lipid matrix (3:1 protein:lipid), is grown by the bacterium when the concentration of oxygen in the salty water becomes too low to sustain the generation of ATP via oxidative phosphorylation [66]. bR converts the energy of "green" light (500-600 nm) into an electrochemical proton gradient, by translocating protons across the membrane, which in turn is used for ATP production by ATP-synthases. bR has been the focus of much interest and has become a paradigm for membrane proteins in general and transporters in particular [67].

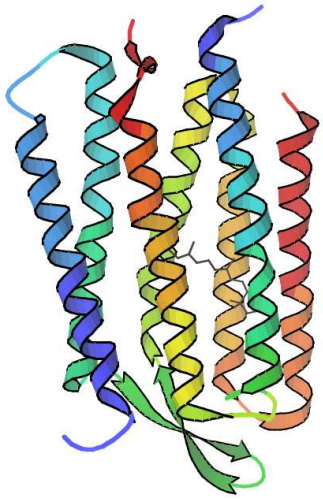

Figure 1.10: *Structure of bR on 1.55* Å *resolution from Protein Data Bank (entry code 1C3W).*

1.2.1 Structure

Bacteriorhodopsin is a small integral membrane protein consisting of seven transmembrane helices, A through G, and short interhelical loops [68]. Although all retinal proteins fold into a seven trans-membrane helix topology with short interconnecting loops, only bR naturally forms patches of two-dimensional crystals in the cell membrane, called purple membrane (PM). The helices are arranged in an arc-like structural model and tightly surround a retinal molecule that forms a Schiff base (SB) with a conserved lysine of helix G (K216 in bR). The retinal separates the cytoplasmic (CP) from the extracellular (EC) half channel that is lined by amino acids crucial for efficient proton transport. The geometry of the retinal, the protonation state of the Schiff base, and its precise electrostatic interaction with surrounding charges and dipoles tune the absorption maximum to fit its biological function [67].

Although the three-dimensional structural model of a protein determined with classical X-ray crystallography or electron diffraction is static, it is invaluable in understanding the function of a protein because it guides the interpretation of dynamic changes observed in time-resolved measurements. Over the years, the resolution of bR structure has been reduced from 3.5 to 3.0 to finally 1.55 Å. From the 1.55 Å crystallographic structure, it is evident that bR contains a continuous hydrogen bonded chain of residues and bound water molecules on the extracellular side of the centrally located retinal Schiff base, and a discontinuous chain on the cytoplasmic side. This arrangement provides both for the coupling of proton release upon deprotonation of the Schiff base, and for a barrier to proton conduction in the unphotolyzed protein. The proton release to the extracellular surface, which occurs early in the photochemical cycle, will utilize the interactions in the extracellular hydrogen-bonded network. Proton transfer from the cytoplasmic surface to the active site, which is delayed until later in the cycle, will depend, however, on forming a network not present in the unphotolyzed structure [69].

1.2.2 Photo-reaction Cycle

The kinetic events that constitute the cyclic reaction after photoisomerization of the retinal, the "photocycle" are described by the intermediate states and the sequence and rates of their intercoversion [70]. At ambient temperatures under low-light conditions, the purple membrane contains a binary mixture of two proteins, one containing the 13-*cis*-retinal and the other containing all-*trans*-retinal. Upon the absorption of light, bR converts from the

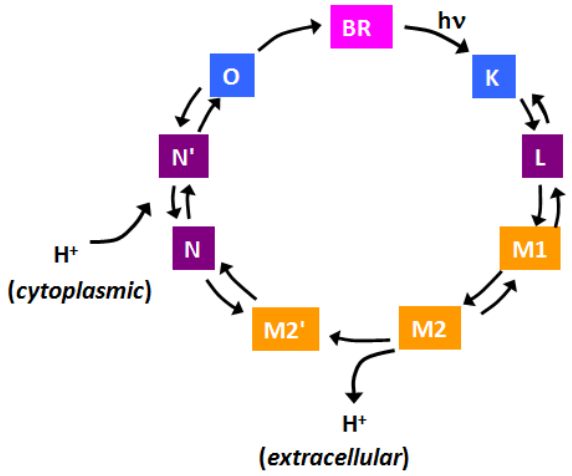

Figure 1.11: *Photocycle of the light-adapted bacteriorhodopsin.*

dark adapted state to a light-adapted state. Subsequent absorption of light initiates a series of different reactions, as are isomerization of the retinal and concomitant conformational changes of the protein, as well as the de- and re-protonation of the Schiff base group [71] with a net transport of proton from the inside (cytoplasmic) to the outside (extracellular) of the membrane. The resulting pH gradient ($\Delta = 0.2$) generates a protonmotive force which is used by the bacterium to synthesize ATP from inorganic phosphate and ADP.

Measurements with time-resolved spectroscopy after pulse photoexcitation and stationary spectroscopy of photostationary states at cryogenic temperatures have identified various photocycle intermediates, such as J, K, L, M, N and O (Fig. 1.11). The six intermediates exhibit distinct states of the chromophore with a red- or a blue-shift of its absorption maximum and are characterized at the molecular level by their FTIR [72], resonance Raman [73] and NMR [74] spectra.

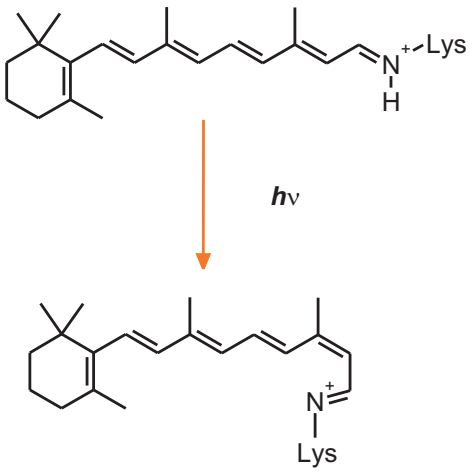

Figure 1.12: *Structural formula of the retinal chromophore bound to the protein via a protonated Schiff base.*

The phototransformation of bR to K is the 'primary event' in the photocycle. This involes an all-*trans* to 13-*cis* photoisomerization of the protonated Schiff base chromophore [75–77] (Fig 1.12). The isomerization of the chromophore creates an electrostatic environment that destabilizes the protonated Schiff base, resulting in deprotonation of the chromophore and protonation of the nearby Asp-85 residue [78]. This process generates the M state, which has the absorption maximum shifted because the chromophore is now unprotonated. Subsequent dark reactions transfer the proton from Asp-85 down to the Glu-194 and Glu-204 region. When Asp96 is reprotonated from the cytoplasmic medium, N relaxes back to O with reisomerization of the retinal to a still twisted all-*trans* form. Full relaxation and deprotonation of Asp85 occurs in the O $\rightarrow$ bR transition.

1.2.3 M-state

The key thermal intermediate in the photocycle is M, the formation of which co-incides with pumping of the proton. Resonance Raman, FTIR and other experimental investigations have established that the retinal chromophore is protonated in all the intermediates other than the M-state. Further, to allow vectoral proton transport, de- and reprotonation of the Schiff base, atleast two M intermediates must exist that differ in the accessibility of the Schiff base (M_1 & M_2). The M-state has an absorption maximum at $\lambda = 412$ nm and revert back to the initial B-state through thermal relaxation processes or by photochemical processes upon photoexcitation with blue light [79]. The thermal relaxation of the chromophore from the M-state is initiated by the reprotonation of the retinal molecule by aspartic acid in position 96 (Asp-96). The retinal then re-isomerizes and relaxes back to the all-trans B-state.

1.2.4 Photoelectric Signals

Photoexcitation of bR generates a proton-motive force upto 300 mV across the membrane. This proton-motive force is measured as photoelectric signals across the circuit as either photovoltage or as photocurrents. The first demonstration of photoelectric effect in bR was performed in 1974. In this experiment, oriented PM fragments were incorporated into a planar black lipid membrane and an electric potential across the membrane was observed during continuous illumination. Given capacitative systems and undistorted signals, the interpretation of the photoelectric responses is straightforward:

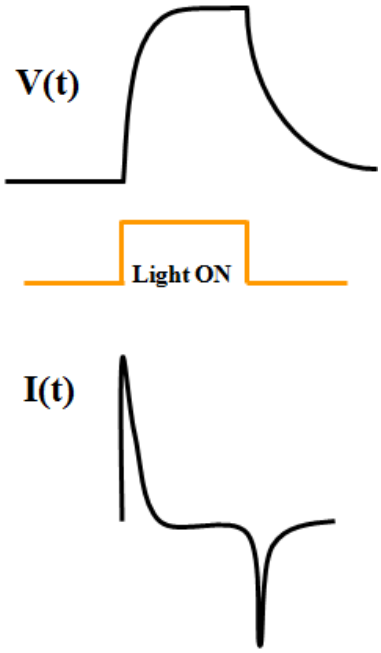

Figure 1.13: *Schematic representation of bR photoelectric signals, $V(t)$ and $I(t)$, for a long duration pulse.*

the photocurrent amplitude, $i(t)$, connected with a given transition is proportional to the product of the charge moved q, the velocity of the proton motion, v, and ϵ is the dielectric constant

$$i = \frac{qv}{\epsilon D} \tag{1.11}$$

whereas the photovoltage amplitude, $V(t)$, of a given component is directly proportional to the charge displacement [71].

$$V(t) \sim \int i(t)dt \tag{1.12}$$

Hence, photovoltage measurements display an approximately time-invariant

sensitivity (i.e. constant signal to noise ratio), whereas photocurrent measurements overvalue fast events and undervalue slow events.

Photoelectric studies have provided fruitful information for the understanding of the proton pumping mechanism in bR [71,80–83]. The photocurrent of bacteriorhodopsin induced by a pulsed laser has been extensively studied, and several components have been identified [71, 81–83]. The first component (B1) is ultrafast, with a rise time less than 100 ps. B1 is thought to originate from the charge separation as the result of retinal photoisomerization from all trans to 13-cis in bR [81, 84]. The second component (B2) has a decay lifetime of 40-100 μs. B2 is thought to be due to the vectorial proton translocation from the Schiff base to the counterion or due to proton release from an unknown proton-releasing group to solution.

On the millisecond time scale, a slower photocurrent component (B3) has also been observed [71, 80, 81, 83, 85–88]. Previous studies on B3, however, have provided little understanding of its origin and factors that affect its magnitude and lifetime. B3 is thought to originate from a different processes, e.g., slow charge-transfer events after the formation of M, the release or uptake of protons or other ions occurring on the surface of bR membrane, concomitant transient dipole moment change, or even secondary ionic events [89].

When excited with a modulated CW light pulse, a differential photocurrent (components D1 and D2 with decay times in milliseconds) is observed from the bR film. D1 is observed when the CW light is turned on, and D2 is observed when the CW light is turned off. However, there are conflicting opinions regarding the actual molecular mechanism of the differential

photocurrent.

Miyasaka and co-workers have suggested that the charge displacement within bR induces the differential current on the electrode adjacent to the bR molecule when bR is excited by light [90, 91]. Robertson and Lukashev, however, have reported that the differential current of bR results from an electrochemical current induced by the local pH change and not by charge displacement [92]. More recent evidence from El-Sayeed and co-workers suggest that the D1 and D2 components is due to the change in the proton concentration near the membrane-ITO interface [89]. This leads to the formation of a transient proton capacitor between the working and counter electrodes. The charging and discharging processes of the proton capacitor produces the differential photoelectric response of bR [93]. The formation of the M intermediate, which leads to an increase of proton concentration at the electrode/electrolyte interface due to proton release of bR, produces the light-on photocurrent; the decay of the M intermediate, which results in a decrease of proton concentration at the interface due to proton uptake of bR, contributes to the light-off photocurrent.

Another feature is the presence of a reverse proton translocation resulting in the opposite polarity of the photovoltage (current) during the back-photo reaction upon illuminating the M-state with blue light [94]. Blue light speeds up M-decay and studies have shown that only the slow component of M-decay kinetics is affected.

The efficiency of extracting and the characteristics of the photoelectric signal are controlled by the external environment, since the limiting factors include the electrochemical reaction kinetics at the bR-electrode interface.

Further, dehydration of PM suspension leads to essential changes in the photochemical cycle thereby modifying the photoelectric signals.

1.2.5 Immobilization of Bacteriorhodopsin

The main propertey of PM is the formation of a hexagonal crystalline array of trimers. Lipids fill the gaps between theses bR molecules. PM consists of 25% lipids and 75% bR molecules. In this kind of structure, bR does not denature below 80°C and retains its chromophoric properties in a pH range from 0.0 - 11.0.

The methods recently used for assembling the PM in the solid state or onto solid supports have included Langmuir-Blodgett (LB) deposition [95], electric field sedimentation (EFS) [96], chemiadsorption self-assembly [97], electrostatic layer-by-layer adsorption (LBL) [98], antigen-antibody molecular recognition [90, 91], sol-gel encapsulation [99] and using polymers as immobilizing matrices [100]. These assembly methods have been successful, in large part, because of the superior stability of the bR.

In this thesis, electric field sedimentation and electrostatic layer-by-layer assembly have been used to orient bR on various substrates. PM fragments have a net negative charge on both sides of the membrane. The generally accepted opinion is that the PM is always negatively charged, and the CP side is more negative than the EC side at $>$ pH 5 and vice versa at $<$ pH 5 [101]. This charge asymmetry of the PM results in a permanent dipole moment directed from the CP side to the EC side [102]. The application of an external electric field to an aqueous PM solution can hence result in the orientation of

the PM in the direction of the electric field, with an electrophoretic movement and sedimentation onto the cathode and forming an oriented PM film [96]. This method is simple, quick and effective for the fabrication of oriented PM film by the electric field sedimentation technique. The experimental procedure involved in growing oriented bR films is discussed in a detailed manner in Chapter 2.

The charge asymmetry, where CP side contains more negative charges than the EC side at pH values above 5, makes PM very suitable for layering using the layer-by-layer method. This asymmetry also provides for a high degree of orientation of the PM, similar to what is obtained using the electric field sedimentation technique. Since an external electric field is not required, layer-by-layer deposition is milder and more facile method for the fabrication of oriented PM assemblies. This layer-by-layer deposition occurs typically for a few monolayers. The experimental procedure involved in layer-by-layer assembly is discussed in Chapter 2.

1.2.6 Applications

Proposed applications of bR, besides being a model protein for ion transport through the transmembrane, can be grouped into four general categories, based on the physiological functions and properties. These are energy conversion, applications in optoelectronics, optical storage and information processing and nonlinear optics.

Since bR is a simple photosynthesis reaction center, one of the applications involves using it as an energy conversion system to transform light

energy into electrochemical energy. The different photovoltage and photocurrent responses of bR at various time scales that arise from the charge displacement and proton translocation can also be used in optoelectronic device applications.

The intermediate states of bR show different spectral shifts. Excitation at different wavelengths (corresponding to the intermediate states) can reversibly convert bR from various intermediates to the ground state. This photochromic nature of bR can be used for optical information processing and storage. The presence of π-electron system of the retinal can exhibit large second-order and third-order polarizabilities. In addition, it has been shown than PM can be oriented by various methods. This added degree of orientation of the retinal further enhances the non-linear optical properties of bR assemblies.

These extreme brine and high temperature growth conditions of the bacterium, together with the crystalline lattice structure of the PM, have resulted in bR that has exceptional stability against salt, high temperature, photochemical degradation, chemicals, and extreme pH media [103]. This stability has made bR an excellent candidate for the investigation of a number of diverse optical and photoelectric studies.

1.3 Optical Microscopy

The wealth of light-matter interactions allow for a variety of highly selective spectroscopic techniques. They provide information on the chemical organization and structure of the sample. The problem of optics, however, is

the difficulty of confining the electromagnetic energy to volumes sufficiently small for the purpose of nanometer-scale characterization and modification.

1.3.1 Far-field Optics

The resolution of a microscope is its ability to distinguesh between the smallest possible objects. This optical resolution is limited by the diffraction of light occurring from the object, due to the wave nature of light. In order to get the entire information on these small features, the objective lens has to collect light of all the diffraction orders. The resolution of an objective/microscope is defined as the distance, d between two adjacent particles which can be perceived as separate entities. Based on the limits of diffraction, the resolution is given by Rayleigh's criteria [104]

$$d = 1.22\,(\lambda/2NA) \tag{1.13}$$

This is directly related to the cone of light entering the objective from the sample. This acceptance angle of light is quantified by a parameter called *numerical aperture* (NA) of the objective. The numerical aperture is defined as

$$NA = n\sin(\theta) \tag{1.14}$$

Here, n is the refractive index of the medium from which the light rays enter the objective and θ is the maximum angle at which the light rays enter the objective. The bigger the cone of light that can be brought into the lens, the higher its numerical aperture.

Therefore, lenses with higher NA can give better resolution. In a far-field transmission microscope, the NA of the objective, together with the NA of the condensor lens providing the illuminating light, determines the resolution. From the above expression, it is clear that the maximum NA an objective can achieve is the refractive index of the medium. One way to improve the NA is to use an immersion medium with a higher refractive index than air. Numerical apertures of 1.3-1.4 are now obtainable with high-quality objective lenses, therefore, Eqn. 1.13 is usually simplified to $d = \lambda/2$. The maximal resolution is then approximately equal to half the wavelength of the radiation used, which for visible light applications results in a spatial resolution of 250-300 nm [105].

These limitations have been well-known for some time, and led many to begin exploring alternative ways of achieving higher resolution optical measurements. Early in the 20th century, Synge published a series of papers in which he proposed a new type of optical microscope designed to circumvent the limitations imposed by the diffraction limit [106]. Synge proposed forming a microscopic aperture with dimensions much smaller than the optical wavelength in an opaque screen [106]. By illuminating the backside of the screen with a high-intensity light source, light passing through the aperture would be confined by the dimensions of the hole. Once positioned in close proximity to the sample surface, the light emerging from the aperture could be used to image a specimen before it had time to diffract out and degrade the resolution. This concept was taken forward in near-field optical microscopy.

1.3.2 Near-field Optics

The resolution of far-field optical microscopy is fundamentally limited by diffraction. Improving the optical resolution beyond the diffraction limits asks for a radically new approach. The diffraction limit becomes less restrictive if the concept of free wave propagation is abandoned and *evanescent waves* are used. Evanescent waves are characterized by amplitudes that decay rapidly in at least one direction in space. The respective component(s), say k_z, of the wavevector are imaginary (more generally, complex). The residual component(s) k_x hence can be larger (in fact much larger) than $|k_i|$, and Δx can be much smaller than $\lambda/100$ nm: *the use of evanescent waves is the key to optics on the nanometre scale* [107]. The properties of evanescent waves are intimately connected to the object material beyond the surface. They exist because of the presence of matter and thus cannot exist in free space.

A typical structure of such non-propagating fields is

$$U(x,y,z,t) = A(x,y,z) \times exp - j(k_x x + k_y y) \times exp(-\alpha z) \times exp\,[j(\omega t)] \quad (1.15)$$

where, A is the amplitude of the field at the point (xyz), $exp - j(k_x x + k_y y)$ corresponds to the propagation term in the plane (xy); $exp - (\alpha z)$ expresses the decrease of the field along the z-axis. The co-efficient α depends upon the material properties and upon its spatial structure.

The experimental feasibility of high-resolution imaging using a subwavelength aperture was first demonstrated by Ash and Nicholls using microwave

radiation [108]. The development of lasers and the use of single mode optical fibers for the propagation of light and the simultaneous development of atomic force microscopy, where force-feedback mechanisms were used to remain in close proximity with the sample, led to the possibility of SNOM development. In the 1980s, Pohl's laboratorory at IBM Zurich first reported sub-diffraction optical measurements [109, 110].

1.3.3 Near-field Microscopy (SNOM)

The central idea of near-field optical microscopy is to retain the spatial frequencies associated with evanescent waves thereby increasing the bandwidth of spatial frequencies. In order to extend the spectrum of spatial frequencies, evanescent waves have to be taken into account. These waves do not propagate and thus cannot be guided towards the sample by using standard optical elements. Evanescent waves are bound to the surfaces of materials, which necessitates that the "evanescent wave carrying object" is brought in close proximity to the sample in order to extend the spectrum of spatial frequencies. In SNOM, this is achieved by different modes of operation that are characterized by the

(i) Type of probe (aperture, scatterer, flourescent particle, etc.).

(ii) Path of the probe during scanning: constant height mode (CHM), constant gap-width mode (CGM), or constant signal-intensity mode (CIM).

(iii) Observation in transmission, reflection, or an indirect mode, e.g. induction of electrical conductivity, heating.

(iv) Contrast mechanism (absorption, phase, polarization, flourescence,

Raman scattering).

The most commonly used mode of near-field microscope is the illumination mode, where the sample is illuminated through a small aperture and light (transmitted or flourescence) is collected from beneath the transparent sample. The field in the neighbourhood of the aperture is laterally confined to dimensions of the size of the aperture, the exposed area of the sample, and thus the resolution of SNOM, is determined by the aperture size rather than by the wavelength of light. By raster-scanning the probe closely over the sample and monitoring the transmitted light or the flourescence emitted by the sample, a microscopic image is obtained. Also, SNOM has the advantage of being operable under ambient conditions. The combination of location, orientation, and time-resolved spectroscopic information of single molecules makes it possible to study chemical reactions on individual molecules in their specific local enviroments.

(a) Theory

The near-field probe can be considered as an oscillating dipole located at the origin of the coordinate system with the dipole orientation along the z-axis (Fig. 1.14). It is easier to represent electric field $E = (E_r, E_\phi, E_\varphi)$ in the spherical vector co-ordinates. In this system, the field components E_φ and H_r, H_ϕ are identical to zero and the only non-vanishing field components are [104]

$$E_r = 2\left(\frac{[p]}{R^3} + \frac{[\dot{p}]}{cR^2}\right)\cos\phi \tag{1.16}$$

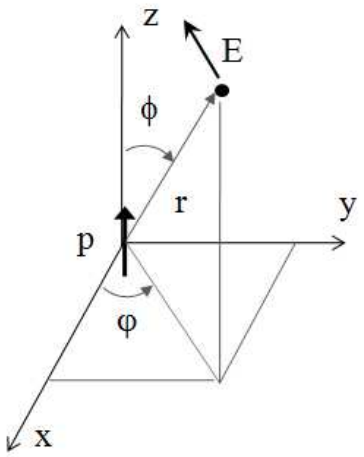

Figure 1.14: *The fields of a dipole are represented in a shperical coordinate system (r, ϕ, φ) in which the dipole points along the z-axis (φ=0).*

$$E_\phi = \left(\frac{[p]}{R^3} + \frac{[\dot{p}]}{cR^2} + \frac{[\ddot{p}]}{c^2 R} \right) \sin\phi \tag{1.17}$$

$$H_\varphi = \left(\frac{[\dot{p}]}{cR^2} + \frac{[\ddot{p}]}{c^2 R} \right) \sin\phi \tag{1.18}$$

where, $[p]$ is the oscillating retarding function of time describing the field propogation and $[\dot{p}]$ and $[\ddot{p}]$ are its derivatives. The structure of the field varies strongly when the point is near the surface, that is for values of R such as:

$$R << cp/\dot{p}, \quad R << c\dot{p}/\ddot{p} \tag{1.19}$$

Assuming that p can be written as:

$$[p(t)] = p_0 \cos(\omega t - R/c) \tag{1.20}$$

where ω is the light pulse duration, inequalities (Eqn. 1.19) leads to the condition

$$R << \lambda/2\pi \tag{1.21}$$

where λ is the wavelength associated with the field. For a dipole emitting a wavelength of 532 nm, R must be smaller than 85 nm to detect the near-field. In the direct proximity of the aperture, for $0 < r < 2a$, a is the aperture radius or the dipole separation, the on-axis intensity decreases approximately exponentially with increasing distance from the screen given by the below Eqn. 1.22

$$I(0,0,r) = \left(\frac{8ka}{3\pi}\right) exp\left(-\frac{3\pi z}{4a}\right) \tag{1.22}$$

In the intermediate region, the aperture field can be approximated by exact dipole fields, including quasistatic, induction and radiation terms. In the intermediate zone, the intensity decay is proportional to z^{-4}. In the usual case of far-field detection ($R >> \lambda/2\pi$) Eqns. 1.16,1.17,1.18 reduces to:

$$E_R = 0 \tag{1.23}$$

$$E_\phi \ \sim \ H_\varphi \ \sim \ \frac{[\ddot{p}]}{c^2 R} \sin\phi \tag{1.24}$$

Hence, in the far-field, E and H are of equal magnitude and perpendicular to each other and to the radius vector, which now coincides with the direction of the Poynting vector [104]. The aperture field behaves as far-zone dipole

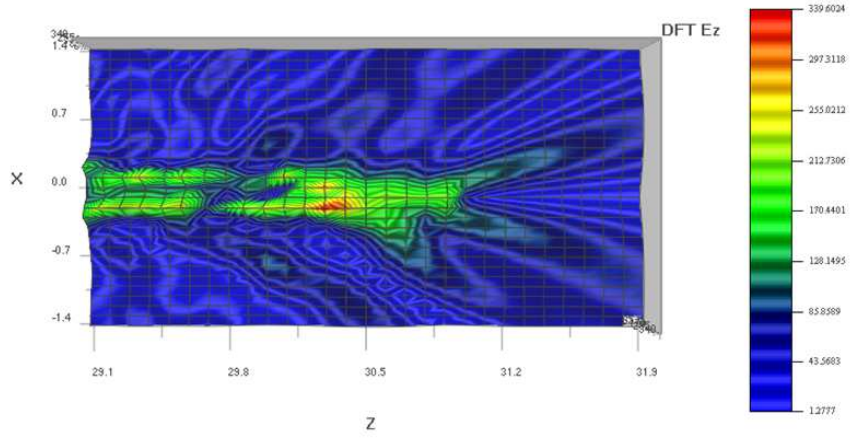

Figure 1.15: *Calculations of E_z through a glass wedge surrounded by aluminum.*

fields. Hence, the intensity falls off as z^{-2}.

Further, a simple model based on the assumption that the electric field $Eexp\,[-i\omega t]$ produced by the tip is essentially static (satisfying the potential condition $\Delta \times E = 0$) can be used to qualitatively explain the observed intensity [111]. The electric field E produced by such a surface charge distribution is given by

$$E = \frac{1}{4\pi\epsilon_0} \int \int \frac{\sigma dS}{r^3} r \tag{1.25}$$

where r is the distance vector from the surface element dS. This integral can easily be evaluated numerically by solving the Maxwell's equation using the finite-difference time-domain (FDTD) method. This model produces two intensity lobes for the total electric field. The x component is highest in the image center (where the z component is negligible), while the z component is highest at the lobes (Fig. 1.15 (where the x component is weak)). The radiation remains collimated to the dimensions of the aperture to a distance

of alteast one aperture radius. For such a separation between aperture and object one may expect a resolution of about 2× the size of aperture.

(b) Applications in Biology

The simultaneous flourescence and force mapping capabilities of SNOM seem particulary well suited to probe biological samples and provide new insights into complex structure-function relationships. These capabilities often complement other techniques used in the analysis of biological samples. For instance, confocal microscopy, while having single molecule detection limits and sectioning capabilities, has lower spatial resolution and does not provide a force mapping of the surface topography. AFM is remarkably sensitive to surface topography but yields little specific chemical information. Used in conjunction with other techniques, SNOM should provide an informative new tool for exploring many biological structures and processes.

1.4 Thesis Outline

A proof of the functionality of bR is in the measurement of photoelectric signals from it. Chapter 2 discusses the photoelectric measurements of bR on various conducting polymer substrates. Photoelectric signals from monolayers of bR on conducting polymers were measured. Further, to study the ion motion to electron conversion across the interface of the signal on the conducting polymer layer a three terminal device architecture was fabricated with two lateral electrodes across the polymer layer and a bR patch in the

middle of it. The concept of passive and active biomolecular signal transduction was used to probe the internal processes of the biomolecules.

The optical activity of monolayers of bR oriented on passive (quartz) and on active (conducting polymers) have been studied using a transmission based scanning near-field optical microscopy based approach in Chapter 3. The transmission changes were correlated to the electronic processes occurring within bR. The role of substrate in the photocycle quantum efficiencies was investigated by carrying out the studies on various different substrates, polymer and quartz layer.

Chapter 4 deals with the electric field induced effects on soft polymeric films. Upon application of an external electric field, the polymer film surface undergoes deformation to produce various morphological changes. The role of visco-elasticity in the electric field induced spinodal pattern formation process was studied by varying the viscous and elastic shear modulus over a wide range. Differences in the elctric field response for different rheological paramters were studied. The understanding of these effects has been used to make molecular contacts, using a liquid alloy, to bR based devices.

Chapter 2

Photoelectric Measurements of Bacteriorhodopsin-Conjugated Polymer Hybrid Structures

Bioelectronics is a subfield of molecular electronics that investigates the use of native as well as modified biological molecules (chromophores, proteins, etc.) in electronic or photonic devices. Long-term stability against thermal, chemical, and photochemical degradation, together with desirable photoelectric and photochromic properties, has made bR one of the most promising biological candidates for device applications.

An additional proof of bR stability and functionality is the presence of photoelectric signals. Photoelectric signals carry valuable information about the photocycle and completments information from other techniques (Visible and UV absorption kinetics, CD, resonance Raman spectroscopy and FTIR). The accurate characterization of the photoelectric properties of bR films is

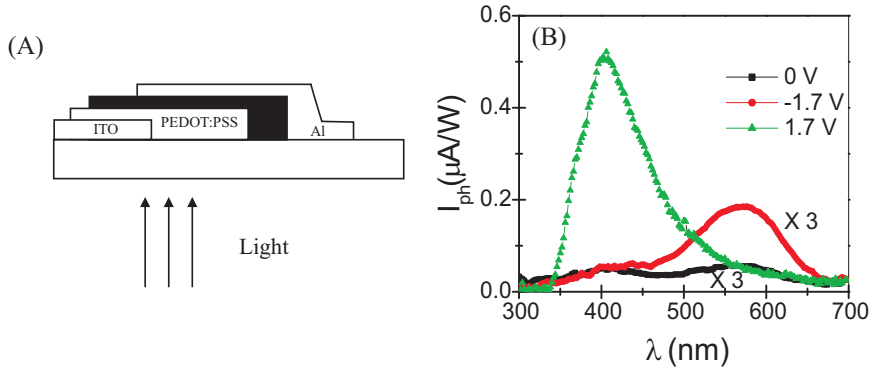

Figure 2.1: *(A) Schematic layout of the device structure on the glass substrate, dark region denotes the bR layer. (B) Normalized modulated $I_{ph}(\lambda)$ of the ITO/PEDOT:PSS/bR/Al sandwich device, adapted from Manoj et. al.* ***Appl. Phys. Lett.****, 2003, 83, 3614.*

essential for designing and developing viable light sensitive devices. In order to acquire information processing at the molecular scale, it is desirble to study photoelectric signals arising from a single patch of bR.

A transient photoelectric response, in the form of a differential response, is measured when bR sandwiched between two metal electrodes, is subjected to light excitation. Earlier results from our laboratory involving bR-conducting polymer structures in the form of solid-state two-terminal sandwich devices using an ITO substrate and top Aluminium electrode revealed distinct enhanced photoelectric signals, and the spectral and temporal characteristics depended on the polarity of the bR-polymer interface (Fig. 2.1) [112]. The spectral features of these bias dependent signals in these sandwich structures were interpreted in terms of the intermediate states appearing in the bR photocycle [113]. The ability of the polymer layer to enhance the photoelectric signal of bR was observed. However, it was not very clear whether the polymer acted as a mere buffer layer or took an active part in the photoelectric

process.

In this chapter, a correlation between the bR photoelectric signal and the electrical transport processes in the polymer layer using a three-terminal configuration is discussed. The conductance modulation of the polymer layer is observed to be directly correlated to the photoinduced activities within the bR molecule. An extension of these studies, is the measurement of photoelectric signals from monolayers of bR on conducting polymers.

2.1 bR based Photoelectric Device Fabrication

Two different types of devices were fabricated, (1) bR based two terminal photocells and (2) 3-terminal devices with the conducting polymer as the active material with bR at the center of the conducting polymer patch.

2.1.1 Two Terminal Devce

The photocell device based on monolayers of bR was fabricated using the electrostatic layer-by-layer assembly. The monolayers of bR on polyaniline were grown on ITO glass. The ITO glass was first cleaned using organic solutions like acetone, iso-propyl alcohol and ethanol amine. Further, these ITO glass substrates were cleaned using RCA treatment, where the ITO substrates were boiled in (NH_4OH:H_2O_2:H_2O 1:1:5) for half an hour and then cleaned with copious amount of water and finally blow dried under nitrogen flow.

Polyaniline and bR are charged polycations and polyanions respectively. They can be grown in a controlled manner using LBL techinque. Monolayers of bR were grown on polyaniline substrates using the electrostatic LBL assembly. An alternative to Langmuir-Blodgett deposition and SAMs is layer-by-layer (LBL) assembly, introduced by Decher, Hong, and co-workers in 1992 [114] for preparing structure-controlled thin films. In LBL assembly, spontaneous sequential adsorption of polycations and polyanions is carried out from dilute aqueous solutions onto charged surfaces. The technique is extremely versatile as the structure, components, and thickness of the films can be controlled through judicious choice of electrolytes and processing conditions. The LBL technique is based on the strong electrostatic interaction between oppositely charged polyelectrolytes. The steps used during LBL technique is as follows:

(a) A charged solid support is immersed into an oppositely charged polyion solution. Electrostatic attraction occurs between the charged surface and the oppositely charged molecule in solution leading to a complete charge reversal at the solid support surface.

(b) The support surface is thoroughly rinsed in water or the respective buffer solution.

(c) The support is then exposed to a solution of the oppositely charged polyion. Electrostatic attraction now occurs between the charged polyion coated solid support surface and the oppositely charged polyion, giving a thin layer of the polyion coating.

(d) This support is now rinsed thoroughly in water.

And the process is repeated until the desired number of layers is achieved.

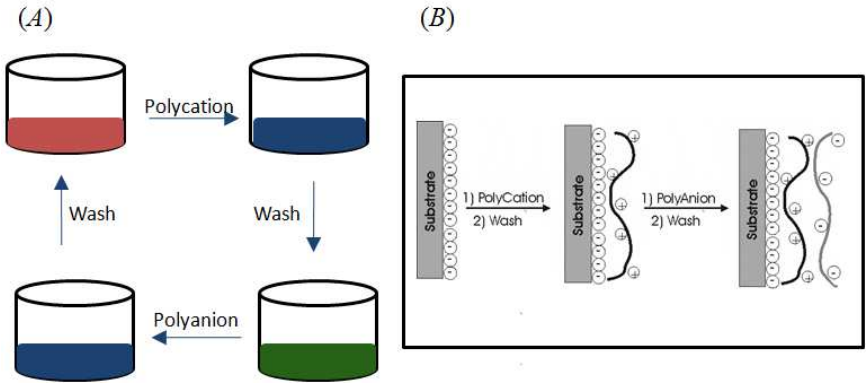

Figure 2.2: *(A) Scheme of the LBL film-deposition process using glass slides and beakers. (B) Simplified molecular picture of the first two adsorption steps, depicting film deposition starting with a negatively charged substrate. The polyion conformation and layer interpenetration are an idealization of the surface-charge reversal with each adsorption step.*

In this adsorption technique, the main concern is to make sure that complete charge reversal occurs after each deposition into the polymer solutions in order to obtain continuous and homogeneous multilayer films (Fig. 2.2).

The LBL technique, in our present case is as follows:

(a) Cleaned ITO substrates were sonicated in a solution containing a mixture of EtOH:$(CH_3)_2O$:$CHCl_3$ in the ratio 2:1:1 for 2 hrs followed by 2% KOH solution sonication. The ITO substrate was then blow dried using nitrogen. This procedure makes the surface of ITO negatively charged.

(b) This negatively charged ITO substrate was then immersed in the polymer (PANI) solution solution for 15 mts to form a thin layer of polyaniline.

(c) The film was then gradually rinsed with 0.1 M HCl solution for 2 mts and then dried under nitrogen flow.

(d) This polyaniline coated quartz substrate was then immersed in TRIS (tris-(hydroxymethyl)aminomethane) buffer solution for 10 mts to obtain the

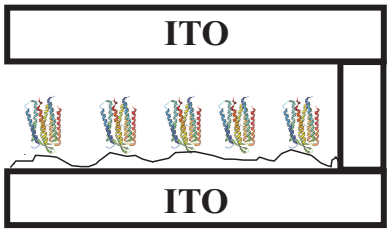

Figure 2.3: *Schematic of the device used for electrolyte based measurements.*

original base form and again dried under nitrogen flow.

(e) This polyaniline coated quartz substrate was then immersed in the bR solution (15 mts) to obtain a monolayer of bR on the polyaniline film.

(f) This bR coated polyaniline film was rinsed again using copious amounts of Tris solution and dried under nitrogen flow.

The top contact in this device was an another ITO glass subsrate placed at distance using spacers. The device was then glued together with araldite (Fig. 2.3) to prevent the movement of the electrodes and also the leakage of the electrolyte. Finally, electrical contacts were taken from these ITO plates using wire contacts and silver paste and this was also covered with araldite to avoid shorting. The space between these two electrodes was filled with 100 mM KCl electrolyte solution.

2.1.2 Three Terminal Device

The three terminal bR-CP based photoelectric device (Fig. 2.4) was fabricated in the following way. On a precleaned glass substrate, gold (Au) strips were thermally evaporated to form an interelectrode gap of 8 mm. PEDOT:PSS, commercially available as Baytron P, was filtered to an obtain homogeneous solution, which was then spin-coated on these Au-coated

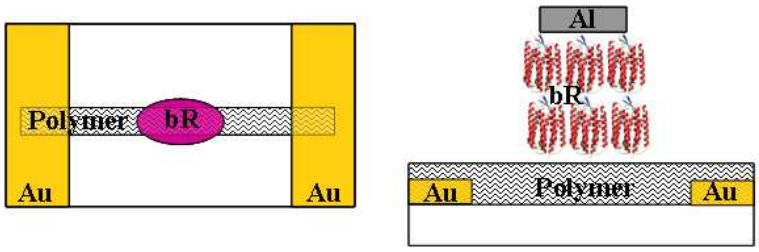

Figure 2.4: *Schematic of the device used for 3-terminal measurements.*

glass substrate. These films were thermally annealed at 140 °C for 1 hour to obtain good quality uniform PEDOT:PSS films of $\sim$ 100 nm thickness. PANI:DBSA, commercially available as Panipol W, was diluted using 1:1 ratio of water and polymer and used for spin-coating and then thermal annealed at 120°C for 10 min to obtain smooth uniform films. The absorption spectra of the respective polymers is shown in Fig. 2.6.

Multilayer bR films were grown using the electric field sedimentation technique. Since PM is known to have a net electric dipole moment, addition of an external electric field to an aqueous PM solution results in the orientation of the PM fragments in the direction of the electric field. Furthermore, if PM suspension was placed between two electrodes and then an electric field of 20-30 V/cm is applied, the PM fragments will electrophoretically move (because of the net negative charge), sediment onto the cathode, and form an oriented PM film [96]. This method is simple, quick, and effective for the fabrication of oriented PM films. In addition, control over which side of the PM (EC or CP) faces the electrode may be obtained through simple adjustment of the pH of the PM suspension [88,89]. Fig 2.5 illustrates the standard setup for preparing an oriented PM film by the electric field sedimentation technique. Typically the thickness of the film is dependent on the time of the

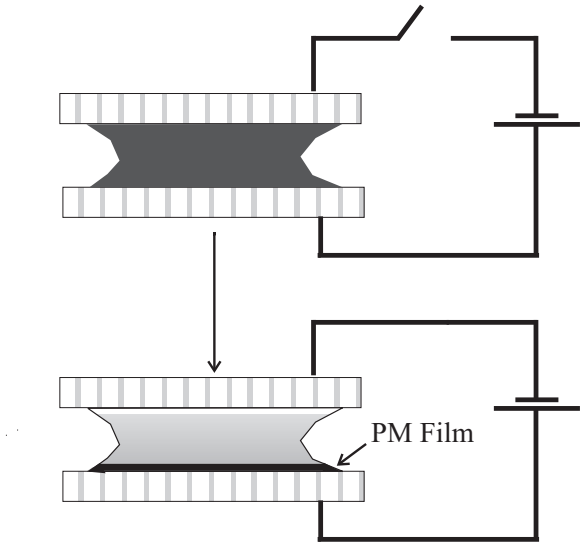

Figure 2.5: *Setup for the fabrication of oriented PM films by the electric field sedimentation method. Due to the net negative charge of the PM, the PM fragments will move and attach to the conducting polymer substrates to form a dense PM film.*

applied DC electric field; a 10 mm thick film can be obtained by application of a 20-30 V/cm DC electric field for about 1 min.

Twenty-five microliters of aqueous suspension of bR (MIB, 10 mg/mL) was deposited on the center (5 mm diameter) of the polymer film. The electric field sedimentation procedure involving a bias potential ($\approx$ 0.1 V) across the droplet, with an Au coated cover slip as the counter electrode was used to orient bR ($\sim$ 200 nm thickness) on substrates during the drying stage, was used to form the bR-conducting polymer structures (Fig. 2.5). The absorption spectra of bR after drying is shown in Fig. 2.6 and is very similar to the solution form, showing that the protein is intact in the dried form.

It is speculated that the anionic component in the polymer blends that

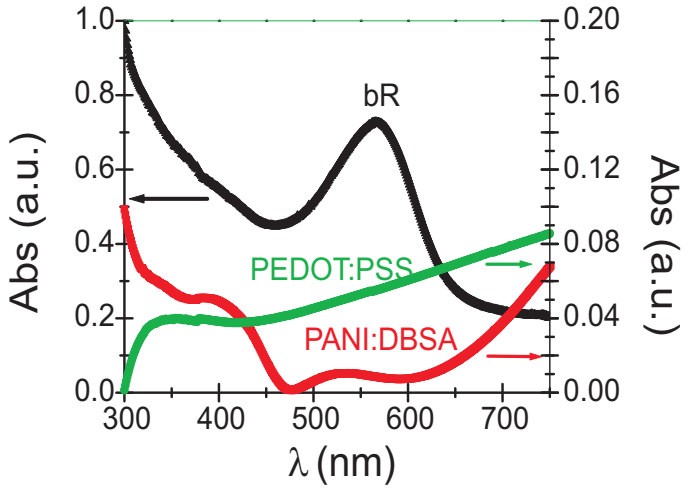

Figure 2.6: *Absorption Spectra of bR, PEDOT:PSS and PANI:DBSA.*

forms the surface layer of the film assists the orientation process. An Aluminium (Al) layer (<bR dimensions) was then evaporated on the bR on some of the devices. The schematic of the device is shown in Fig. 2.4.

2.2 Device characterization

A wide variety of techniques were used to measure the photoelectric signals, both in continuous and pulsed mode. Also, photocurrent profiling was done in order to study the photoelectric signals from local areas (single patch).

2.2.1 Intensity Modulated Photocurrent Spectroscopy

The absorption of photons, of the appropriate wavelength, by bR initiates its photocycle, giving rise to photoelectric signals. These photoelectric signals at specfic wavelengths can be picked up to give us a spectral profile. Photocurrent spectroscopy reveals a direct correlation to the absorption process

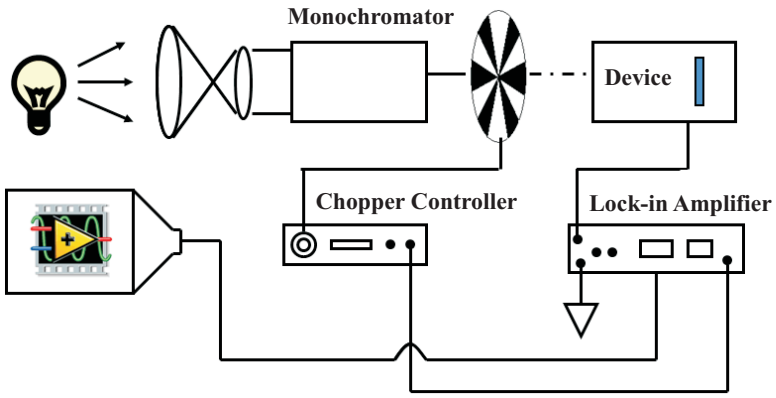

Figure 2.7: *Intensity modulated photocurrent spectroscopy setup.*

the state of bR molecule. These measurements were carried out on a wide variety of 2- and 3-terminal bR based devices (as described in the previous section), using a lock-in technique. A chopper (SRS) was used to modulate the monochromatic light and this was used as the excitation source and photoelectric signals were measured using a lock-in amplifier (SRS 830) with the chopper frequency as the reference. Sufficient interval was given between two consecutive wavelength to avoid any history effects. This technique gives very high signal-noise ratio as the amplifier used amplifies signals with frequency similar to that of the reference and cuts out all other signals of other frequencies. Further, the photoelectric response was also measured with a pump beam of continuous wave (CW) at $\lambda = 532$ nm. Light levels of low intensity (1 mW/cm^2) were used to minimize thermal effects. The standard experimental setup is shown in Fig. 2.7.

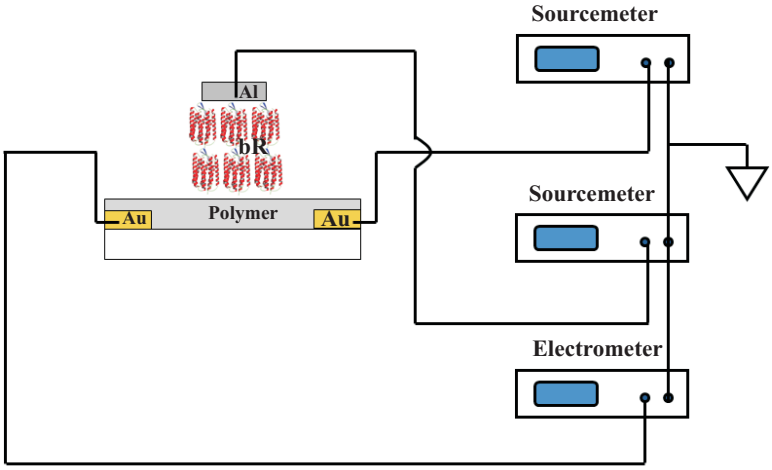

Figure 2.8: *Schematic diagram for bR based three terminal device characteristics measurements.*

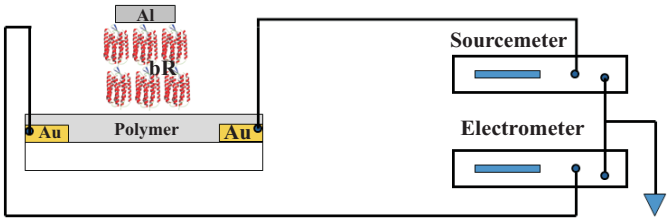

Figure 2.9: *Schematic of the transient measurement setup.*

2.2.2 I-V Measurements

Two identical sourcemeters SM1 and SM2 (Keithley 2400) along with a high impedance electrometer (Keithley 6512) were used for measuring the output characteristics of 3-terminal bR based devices and to study the changes in conductivity of the underlying polymer layer. The schematic of the experimental set-up is shown in Fig. 2.8.

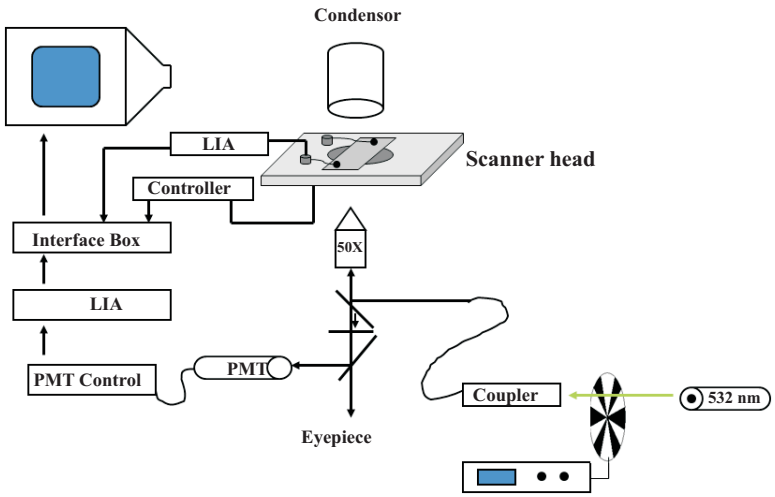

Figure 2.10: *Home built wide-field optical scanning microscopy setup.*

2.2.3 Transient Measurements

Transient responses of bR based devices give insight into the microscopic picture of the charge transport and movement, when illuminated light. A high impedance (10^{14} Ω) electrometer (Keithley 6512), which has a large integration time constant, was used to carry out the measurements in the millisecond regime by illuminating the sample for around 50-100 sec. Different light sources such as lasers at λ = 405 nm and 532 nm were used. A, typical experimental setup is shown in Fig. 2.9.

2.2.4 Wide-Field Optical Scanning Microscope

Photocurrent contrast microscopy on monolayers of bR on conjugated polymer based devices was carried out using a home built setup was assembled around the OLYMPUS inverted microscope as shown in Fig. 2.10. Scanner head (NIS-70) and the software (Nanoview 2.2v) was procured from Nanonics Inc, Israel. The scanner head (dimension 7 cm $\times$ 7 cm $\times$ 0.5 cm, with

a circular optical opening) has a scanning range of 70 μm in all the three directions. The interface box records data corresponding to each x-y position simultaneously from many channels. In most of the experiments carried out in our laboratory, two channels were used to simultaneously measure the photocurrent as well as the reflected light intensity. Both the measurements were done using a lock-in technique (SRS 830). The reflected light was collected using the camera port, where a high sensitivity photomultiplier tube (Perkin Elmer, Model No. MP962) was mounted. The wavelength of the excitation used for local photocurrent measurements was $\lambda = 532$ nm which had a spot diameter of ~ 500 nm.

2.3 Photoelectric Measurements of Monolayer bR films

The short-circuit photoelectric spectrum ($I_{ph}(\lambda)$) (Fig. 2.11), measured across the two ITO electrodes, was similar to the absorption spectra of the pristine bR showing a maximum value at $\lambda \approx 580$ nm. The transient response of monolayer of bR on conducting polymer coated ITO substrate upon photoexcitation, was similar to that of the pristine bR response (Fig. 2.12). Upon, switching ON the light, a fast increase in the current was observed, which decays back to the initial value within a few secs. Further, upon switching OFF the light, a negative spike was observed [88]. The photoexcitation of bR, leads to proton translocation from the cytoplasmic side to the extracellular side. This proton motion leads to the charge fluctuations

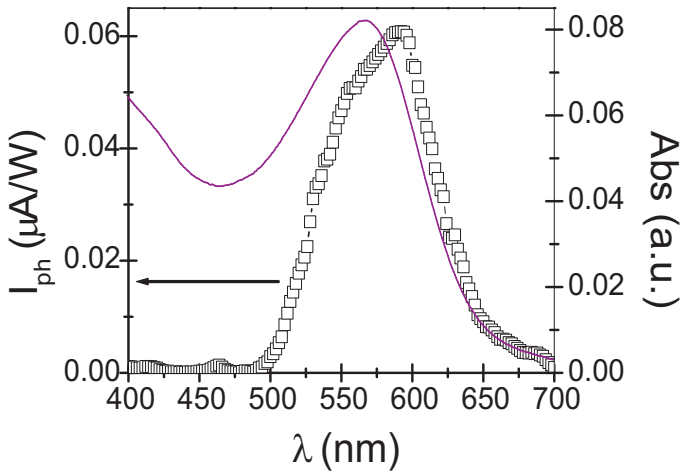

Figure 2.11: *Short-circuit photoelectric spectral response ($I_{ph}(\lambda)$) of ITO/CP/bR/electrolyte/ITO based device.*

within the vicinity of the membrane and these charge fluctuations are then amplified by the electrolyte ions and was measured as photoelectric signals across the two electrodes.

To study the photoelectric signals arising due to a single patch, wide-field photocurrent imaging was done using a home-built set up (Fig. 2.10) as described in the earlier section. Fig. 2.13a shows the high resolution photocurrent image of bR monolayers on the conducting polymer substrate when the sample was illuminated with $\lambda = 532$ nm. The corresponding line profile of the photocurrent image is shown in Fig. 2.13c. Fig. 2.13b shows the reflection contrast image of the same area with the corresponding life profile shown in Fig. 2.13d. The reflection image is negatively correlated to the photocurrent image. The photocurrent essentially arises from the limited number of bR molecules within the beam area. Upon illumination with $\lambda =$ 532 nm, the bR molecules in the B-state absorb light and the movement of protons within the molecule gives rise to charge fluctuations that is picked

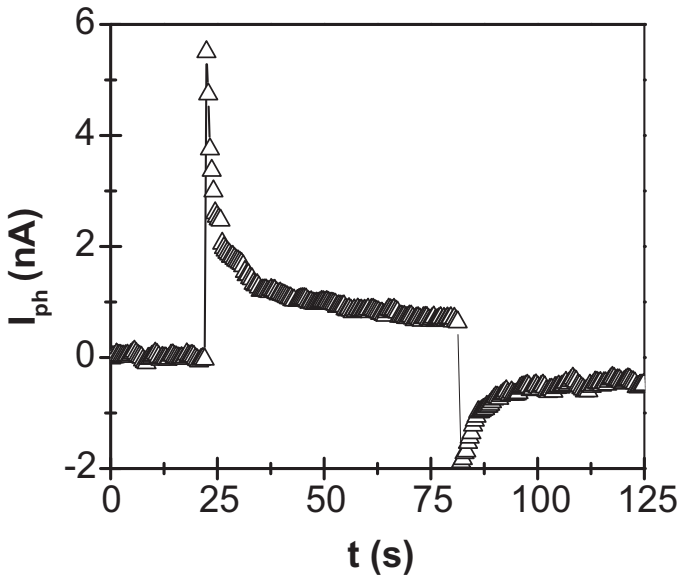

Figure 2.12: *Photoelectric response ($I_{ph}(t)$) as a function of time of the ITO/CP/bR/electrolyte/ITO based device at λ = 532 nm (Power = 1mW/cm^2) in short circuit mode.*

up as photoelectric signals in the external circuit.

2.3.1 Photoelectric Measurements of Multilayer bR films

(a) bR on PEDOT-PSS

A clear feature of the interplay between bR and the polymer layer was the striking presence of a photoelectric signal (0.5 mV, 10^8 amplification from a current to voltage preamplifier) between the two lateral Au-electrodes bridging the PEDOT:PSS polymer film (Fig. 2.14) even in the absence of any external bias in the circuit. The local bR origin of these signals was also verified by carrying out measurements on plain polymer structures without bR where the signal was absent. A spatial profile carried out by scanning the light source locally on the PEDOT:PSS strip confirmed the bR-origin of

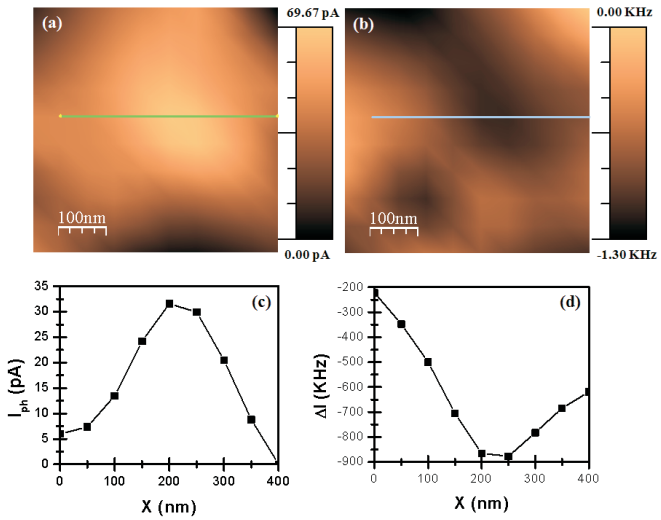

Figure 2.13: *(a) High resolution scanning photocurrent contrast image of bR monolayers on polyaniline coated ITO substrate. (b) Reflection image of the same area. (c) and (d) The corresponding life profiles of photocurrent and reflection images, respectively. Scan area - 500 nm × 500 nm.*

the signal in the circuit.

The introduction of Al electrode on the bR patch (Fig. 2.15) further enhances the lateral signal across the Au terminals (I_{Au-Au}). The lateral short-circuit ($I(t)_{Au-Au}$) transient signal with Al electrode floating, expectedly revealed characteristics analogous to the transmembrane bR differential response (Fig. 2.15). The photoelectric response spectrum, $V_{ph}(\lambda)$, across the Au electrodes clearly corresponds to the bR ground state (570 nm) (Fig 2.16). Upon additionally pumping the sample, a spectral weight transfer from the ground state (B-state) to the intermediate M-state (410 nm) was observed (Fig 2.16) giving a quantum efficiency of 74% for the B to M conversion for a pump beam at $\lambda = 532$ nm with 1 mW/cm^2 power density.

The presence of Al electrode was utilized to probe the transverse process across the bR-conducting polymer interface by measuring the signals across

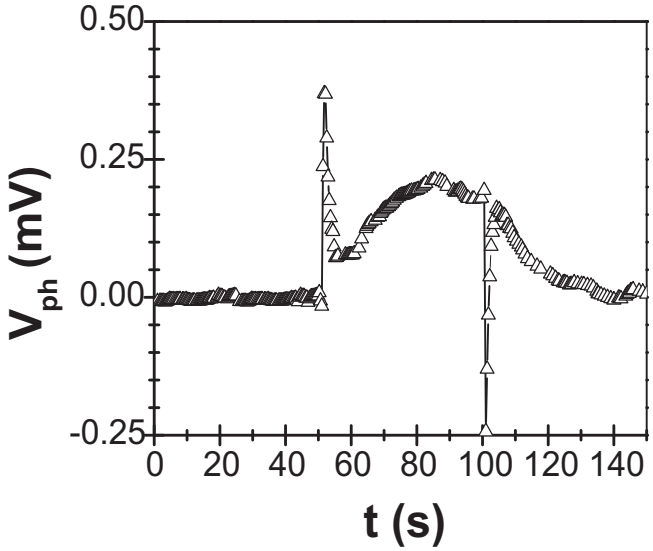

Figure 2.14: *The lateral DC (V_{Au-Au}) transient response to a light source (532 nm, 1 mW/cm^2) along the PEDOT strip, without the top Al electrode.*

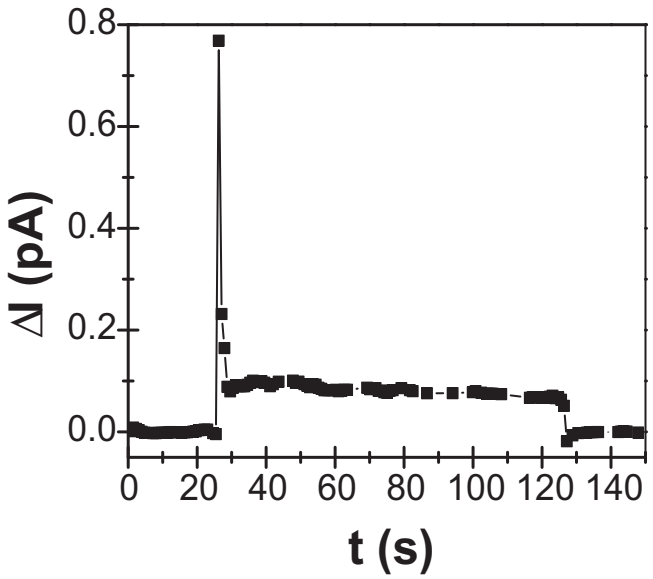

Figure 2.15: *The lateral, short-circuit DC (I_{Au-Au}) transient response to a light source (λ = 532 nm, 1 mW/cm^2) along the PEDOT strip, with the top Al electrode floating.*

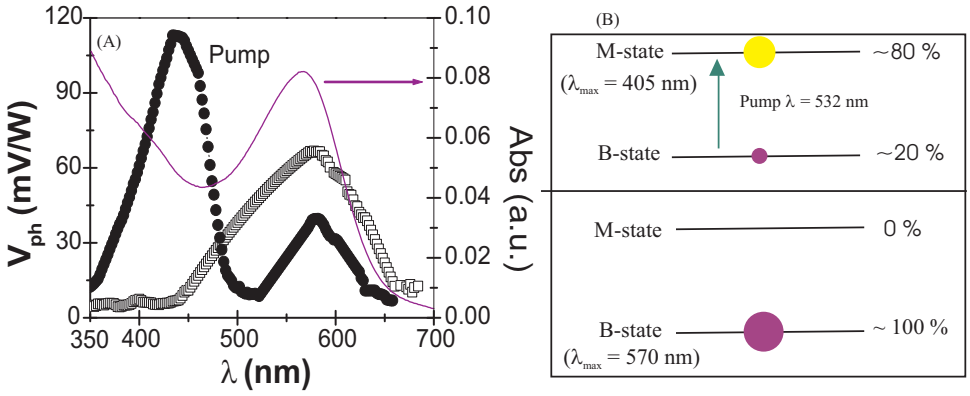

Figure 2.16: *(A) Spectral response $V_{ph}(\lambda)$ (measured using lock-in technique, ω = 18 Hz) across the lateral Au electrodes (Al - floating). (B) Shows the population in each state, presence and absence pump laser.*

the top Al electrode and the shorted the bottom Au electrodes. Sizable DC photoelectric bR signal across $I_{Au,Au-Al}$, was observed even in absence of an external bias. The $V_{ph}(\lambda)$ measured between the shorted Au electrodes and the top Al electrode emphasizes the bR origin of the photoelectric signals in lateral circuit. Upon applying an additional bias to the top Al electrode, the photoelectric signals were further enhanced due to the contribution from the bulk of the bR and the photoelectric response (Fig 2.17) approached that of a 2-terminal diode (sandwich) configuration. Measurements in this configuration with bias, converge to the earlier observations on the 2-terminal devices, where the polymer and bR layer were sandwiched between an ITO and Al electrodes [112]. In, the present case, the difference is the marginally lower magnitude of the photo-signal due to a signal drop across the conducting polymer layer ($\sim$ 200 MΩ) compared to the drop across the ITO electrode (20 ohms) and the contact spot in the earlier report [112].

In order to understand interfacial processes, the changes in the lateral conductance of the conducting polymer layer upon photoexciting bR were

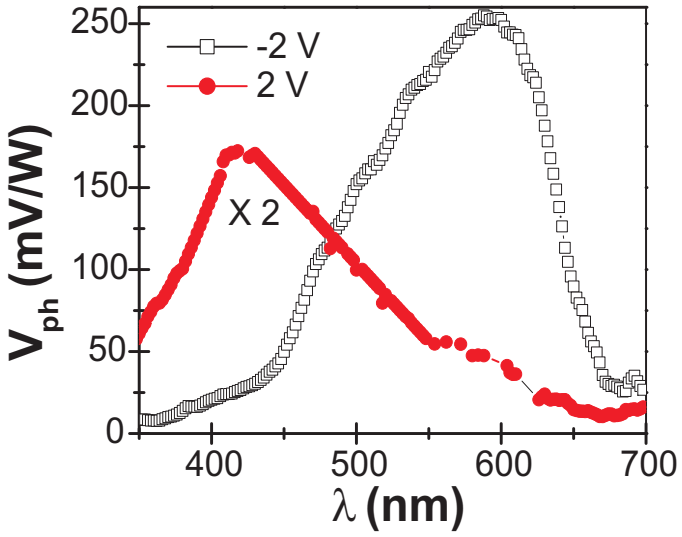

Figure 2.17: *Transverse $V_{ph}(\lambda)$ measured between Al and shorted Au electrodes. Pump laser: 532 nm, 1 mW/cm^2.*

monitored ($I(t)_{Au-Au}$) of the polymer layer (V_{Au-Au} = 0.5 V). An important point of note is that the application of the Al-gate bias without any photoexcitation did not cause any electrochemical change (de-doping) in the polymer layer, i.e. the conductivity of the polymer (within 5%) was not modified. In the dry bR patch, the structurally bound and the relatively low concentration of residual water molecules [115] are not sufficient to promote electrochemical reduction of PEDOT:PSS. Upon photoexcitation, an asymmetric response was observed (Fig 2.18) suggesting a preferred direction of H^+ displacement (towards the polymer layer). The signal changed from differential response at V_{Al-Au} = 0 V gradually to a resistive character at higher positive (+Al) voltages (Fig 2.18). However, upon removal of the photoexcitation, the conductance changes did not persist and the conductivity of the polymer layer reverted to its original value (Fig. 2.18). Upon terminating the photoexcitation, the exponential decay of the current was

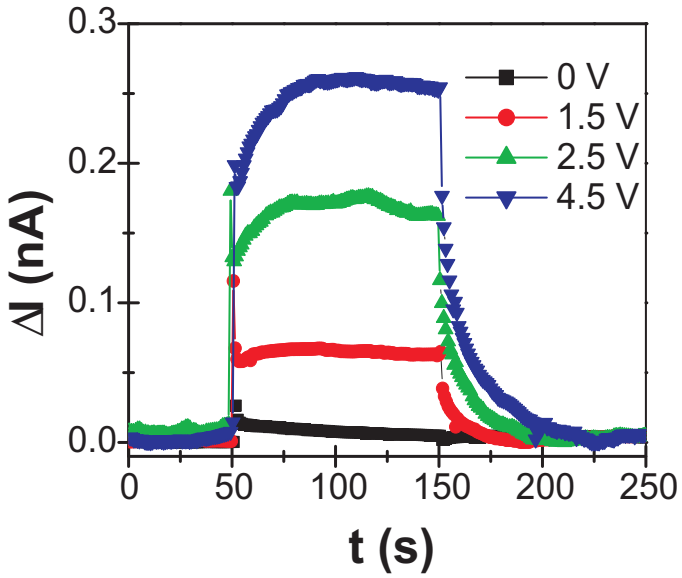

Figure 2.18: *Transient response* $\Delta I(t)_{Au-Au}$ *(*V_{Au-Au} *= 0.5 V) of a three-terminal PEDOT/bR device upon photoexcitation (532 nm, 1 mW/cm*^{2}*) at different* V_{Al-Au}*.*

modeled in terms of the diffusion of the protons in bR away from the interface, $I \propto A * exp(-\frac{t}{\tau})$ with a single time constant that increased with the applied bias (8.4, 11.9 and 14.6 s for 1.5, 2.5 and 4.5 V respectively).

(b) bR on PANI:DBSA - 2-terminal

The steady-state photoelectric signal ($V_{ph}(\lambda)$) (Fig. 2.19) is easily observable in the two-terminal bilayer sandwich structure ITO/PANI/bR/Al structure. The photoelectric spectrum in these devices were similar to that of the pristine bR case. A clear transfer of the spectral weight from the B-state to the M-state was observed upon introducing an additional pump of $\lambda = 532$ nm (Fig. 2.19).

Upon switching ON the light, a differential photocurrent in the form of a positive spike is observed (Fig. 2.20A) during the transient measurements.

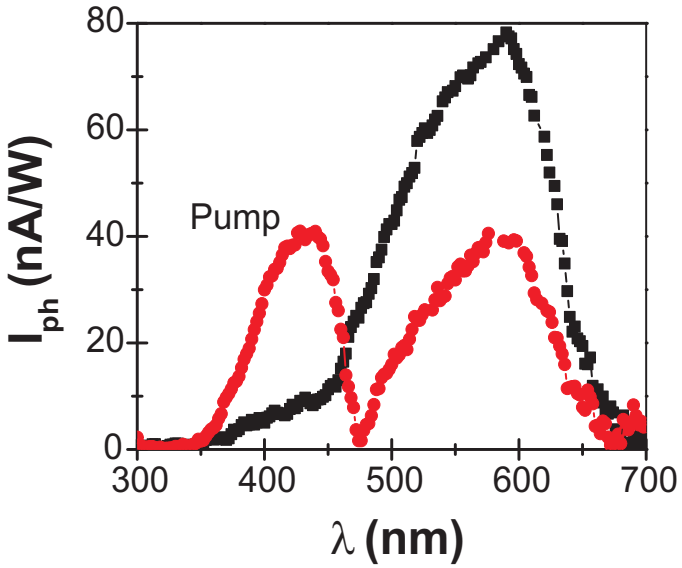

Figure 2.19: *Photocurrent spectrum, $I_{ph}(\lambda)$ of the bilayer device consisting of bR on conducting polymer PANI (ITO/PANI/bR/Al).*

The photocurrent does not decay back to its initial value, which is attributed to some diffusive components. Upon switching OFF the light, a negative differential photocurrent was observed. The positive and negative spike upon switching ON and OFF of the light resembled that of the pristine bR case. An important observation in the bilayer structures was the gradual decrease of the steady-state photoelectric voltage ($\lambda = 532$ nm) in magnitude over a period of time, which was attributed to the PANI-doping process. This indicated that the photocycle is not completed and the bR is frozen in the M-state (Fig. 2.20B). The frozen M-state was observed in the form of a small steady-state photoelectric signal at $\lambda = 405$ nm. The transitory PANI-doping process implied that the pumped protons are not readily available for reprotonation of the bR molecule leading to a decrease in the bR cycle completion rate and the appearance of a slowly decaying V_{ph}.

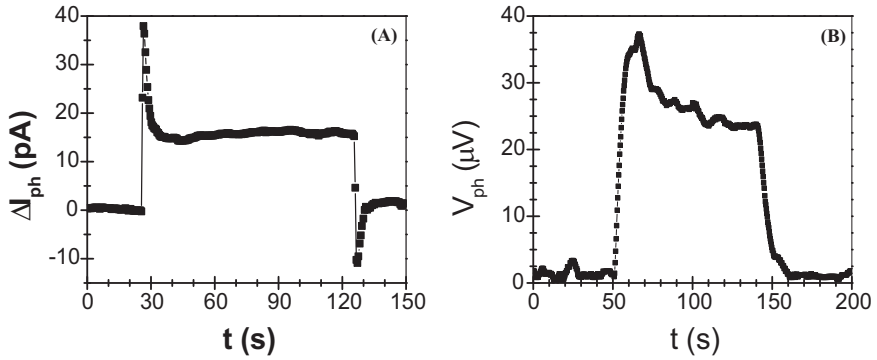

Figure 2.20: *(A) Transient Photoelectric Response ($\Delta I_{ph}(t)$) as a function of time of the bilayer device consisting of bR on conducting polymer PANI (ITO/PANI/bR/Al) at λ = 532 nm in short circuit mode. (B) Photoelectric voltage V_{ph} as a function of time.*

(c) bR on PANI-DBSA - 3-terminal

Transient DC measurements of three-terminal device structures based on PANI/bR, between the top Al electrode and the shorted Au electrodes, revealed a direct increase in $I_{Au,Au-Al}$ upon photoexcitation instead of the differential response as observed in PEDOT:PSS/bR structures (Fig. 2.21). Note that the steady-state frequency domain technique was not suitable to observe these photochemical effects on the PANI surface, since the slow diffusion and reaction process within the polymer films were not correlated to incident photoexcitation rates. It was observed, after carrying out studies on a large number of devices, that the photomodulated lateral signal, which was observed in the case of conducting polymers based on PEDOT:PSS/bR, was absent in the case of PANI/bR. The absence of the steady-state lateral signal as well as in the transverse case was partially attributed to larger resistance of the polyaniline films, which is greater than an order of magnitude than that of the PEDOT:PSS films for similar device dimensions.

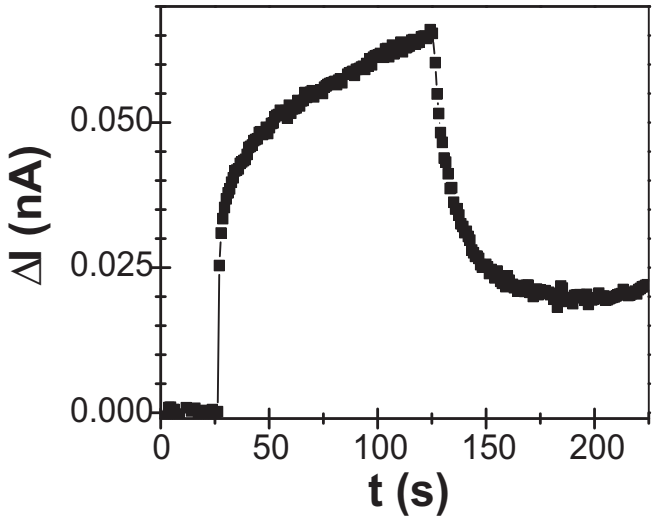

Figure 2.21: *Transverse $\Delta I(t)_{Al-Au}$ upon photoexcitation across the bottom shorted Au electrodes and the top Al electrodes.*

The results get modified upon introduction of bias to the top Al electrode, with a larger signal for positive bias, whereas in the negative bias the conductance remains unchanged. In the three-terminal device structures involving PANI/bR, the lateral DC I_{Au-Au} ($V_{Au-Au} = 0.5$ V) increased upon illumination, indicating features of active doping of the polymer surface initiated by the bR-proton pumping activity. Upon switching off the light, $I(t)_{Au-Au}$ followed a characteristic decay profile (Fig. 2.22). Note that the current value after the exposure to a brief duration of light was higher than the initial value (Fig. 2.22). This residual increase in the conductivity appeared to be a function of the applied transverse voltage (Fig. 2.22). The decay $I(t)_{Au-Au}$ upon the termination of the photoexcitation followed the double exponential profile, $I \propto A[exp(-t/\tau_1) + exp(-t/\tau_2)]$, indicative of two independent processes. The decay parameters and the bias voltage cannot be correlated because of the persistent residual fraction of the current that appears as an

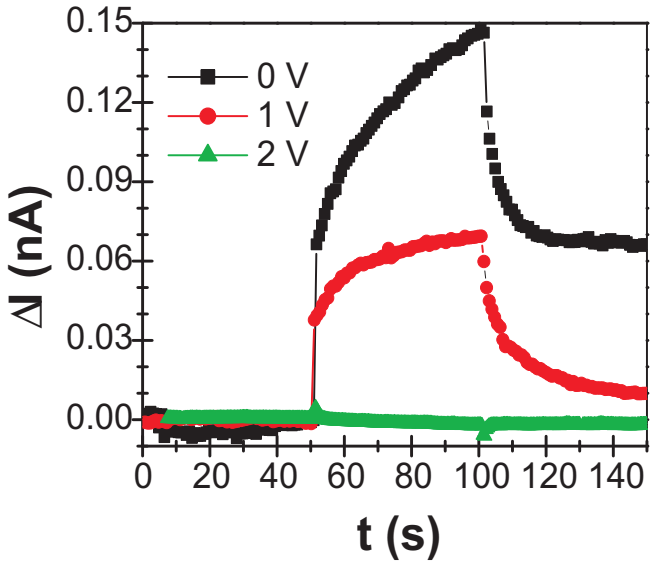

Figure 2.22: $\Delta I(t)_{Au-Au}$ *(V_{Au-Au} = 0.5 V) of a three-terminal PANI/bR device at different* V_{Al-Au} *upon photoexcitation (532 nm, 1 mW/cm^2).*

additional parameter.

2.4 Discussion

2.4.1 bR on PEDOT:PSS

The general microscopic picture of the current induced by photoexciting bR can be attributed to the charge motion of the retinyl chromophore that effectively causes changes in its dipole moment [116]. The orientation of the dipole moments due to photoinitiation of bR causes a time-varying electric and magnetic field in space (Fig. 2.23). The conducting polymer antenna picks up these variations in the form of displacement currents across its lateral electrodes (similar to the conventional metal antenna). The transduction parameters are dependent on the extent of interaction and are inherently

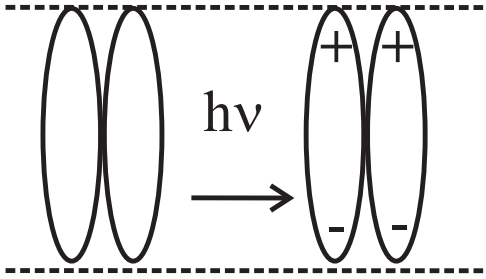

Figure 2.23: *The oriented dipole mechanism. The photoelectric signal is a manifestation of charge separation during the formation of a transient array of electric dipoles.*

lossy. The polymer layer acts like a microstrip line, picking up the charge fluctuations in bR upon photoexcitation.

The observed transient photoelectric signals across the lateral electrodes (Fig. 2.14) was simulated using a simple circuit model, consisting of resistors and capacitors. The PEDOT:PSS channel is modeled as resistor with resistance ($\sim$ 200 MΩ, as observed in our devices). The microscopic circuit of bR consists of an voltage sourcce, resistors and capacitors. The multilayer bR patches can be modeled by a highly interconnected network of resistors and capacitors, which was further reduced or simplified into a common irreducible equivalent circuit consisting of a single resistor ($\sim$ 1 GΩ) and capacitor ($\sim$ 100 pF) in parallel with a voltage source (Fig. 2.24) [117, 118]. Upon photoexcitation of bR patch, the change in its membrane potential gives rise to an external voltage in the circuit, which decays back to the initial value upon terminating the light.

This circuit (Fig. 2.24) can be simulated using PSPICE circuit simulator. The changes in the lateral circuit current were observed, when a square pulse (0.1 V, width = 100 ms) is given to voltage source V1. The simulation

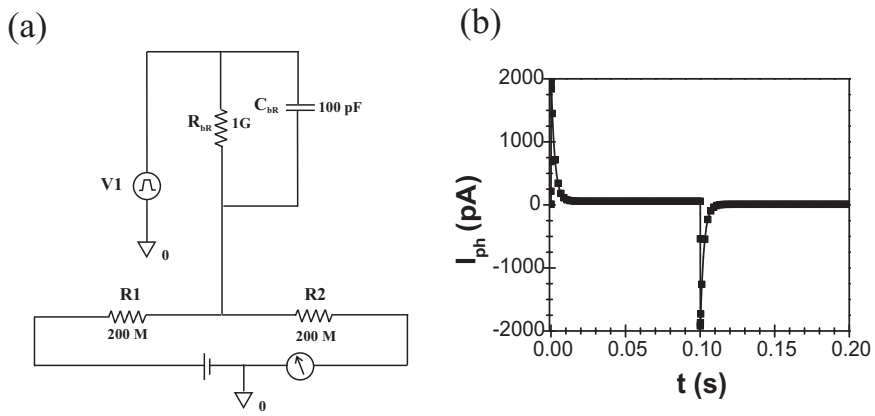

Figure 2.24: *(a) The schematic of the circuit model with the top representing bR while the bottom represent the PEDOT:PSS layer. (b) Simulation results show the change in the lateral circuit current upon pulsing the voltage source, V1.*

results show a differential response in the lateral circuit (Fig. 2.24B), that is qualitatively similar to the one observed in Fig. 2.14.

It is speculated that the initial fast spike in the lateral signal across the PEDOT strip arises from the change of dipole moment within the adjacent layer of bR molecules upon photoexcitation [119]. The change in the dipole moment induces an electric field which modifies the interface potential between bR and the PEDOT:PSS layer. These changes in the surface potential of bR temporarily modify the local transport pathways in the PEDOT:PSS layer that in turn results in a transient change in the conductivity of the polymer layer. Other factors that may influence include photoinduced ionic leakage and thermal effects, which is small in the present case [120].

The time constants observed in these cases were similar to the ones observed by Macdiarmid et. al and Epstein et. al in their field effect transistors based on PEDOT:PSS as the active material [53, 54]. The transient profiles, indicating differential nature of the photoinduced current and the

$V_{ph}(\lambda)$, corresponding to the bR signatures in both the configurations clearly reveals the interplay between the lateral and transverse processes. No permanent change in conductivity of the PEDOT:PSS layer was observed after the light exposure experiment on the bR patch. Experimental observations do not point to the possibility of H^+ reducing PEDOT:PSS or compensating PSS^- [55,56]. The surface morphology and the electrical transport characteristics of PEDOT:PSS appears to be a factor for observing the photoelectric features. Dried PEDOT:PSS film in its pristine form is known to phase segregate with the surface richer in PSS^- component. Addition of solvent agents such as sorbitol and glycerol results in films with more uniform surface and higher conductivity [121]. The signal transduction was not observed for device structures with the higher conducting form of PEDOT:PSS (blended with glycerol) films. These results point to the importance of the dimensional and impedance matching conditions. Engineering the polymer film surface can then optimize the signal efficiencies.

2.4.2 bR on PANI:DBSA

In the case of PANI, it is known that introduction of protonic acids, in addition to controlling the oxidation state, increases the conductivity due to the protonation at the nitrogen site [18]. The acid-based doping mechanism is different from the oxidative doping achieved in other conducting polymer systems [1, 18]. PANI:DBSA films are generally aggregated nanoparticles. The hydrophobic tails of free and bonded DBSA molecules are arranged in a way so that they all turn towards each other, while the hydrophilic groups of

the free DBSA turn to the surrounding medium [122]. In these nanoparticles, the anilinium cation resides in the shell complexed with sulfate ion. The anilinium cations are oriented with the phenyl moiety toward the core and the NH^3 to the outer side [123]. The excess DBSA acts as surfactant in the solution and plays a role of plasticizer in the film. This represents an appropriate situation for the bR-conducting polymer film interface, where the bR upon photoexcitation, can possibly source protons from its environment and transfer them across the interface. The efficiency of this process is likely to be affected in dried films, but signature of this interplay is indicated in the results.

The results from these bulk measurements can be attributed to a transient surface doping phenomena, representing only a fraction of conducting polymer film. Additionally, the excess space charge on the polymer due to the proton diffusion-limited process can reduce the efficiency of the doping mechanism. The observation that a voltage bias across the bR patch alone does not activate changes in conducting polymer but requires the appropriate photoexcitation points toward a correlation between the bR photoactivity and electrical property of PANI. The PANI/bR structures provide an example of a hybrid system with the results arising from a combination of interdependent physical processes of each system.

2.4.3 Proton pumping in bR

From the biophysical perspective, it is known that proton pumping efficiency of bR in the solid state is reduced [67,124]. The signature of proton displacement in bR upon photoexcitation in different media is well documented. However, the spatial degree of freedom for the proton pumped into the extracellular region is not known in great detail. There have been reports that indicate rapid pH variation on the surface of bR accompanied by very slow changes in the bulk outside in the medium [125, 126]. The existence of $V_{ph}(\lambda)$ features representing the two states (B and M) along with the absence of commensurate nonreversible changes in the polymer indicate a constrained spatial degree of freedom for the proton. The protons are reabsorbed by the retinal chromophore either directly or indirectly through percolating pathways present in the purple membrane, thereby maintaining the charge neutrality.

2.5 Conclusions

In conclusion, the possibility of efficient signal transduction of a biophysical process in bR to the adjacent conducting polymer layer is demonstrated. Mechanism of the bR*-induced conductance changes in PEDOT:PSS appeared to be different from that of PANI. Steady state measurable photoelectrical signals in the polymer (PEDOT:PSS) circuit represented internal changes of the proximal biomolecule upon photoexcitation. The light-induced dipole fluctuations within bR are translated into conductance changes in the

PEDOT:PSS case. A simplified circuit simulation done using PSPICE circuit simulator qualitatively reproduces the observed experimental transient profiles. A signature of transient doping of the polymer surface due to the proton displacements in the bR system was observed in the PANI:DBSA case, where the surface H^+ concentration changes are picked up by the polymer.

Chapter 3

Microscopy of Bacteriorhodopsin Monolayers

Single-molecule studies of functional proteins, especially in their native environment are considerably important and yield valuable information on the structure-property correlations [127]. These single molecule studies yield results that can be different from measurements on an ensemble or bulk collection of molecules in a subtle manner, where the individual characteristics cannot be distinguished and only the average behavior is measured [128]. Single-molecule fluorescence has emerged as a useful tool for probing various processes which cannot be fully understood on the bulk level, such as the movement of myosin on actin filaments in muscle tissue [129] or the details of individual local environments in solids [128]. The merit of this new technique is that the problem of ensemble averaging, found in standard spectroscopic techniques, is totally removed. Hence, in many cases, SMS reveals

fluctuation phenomena that are totally obscured by conventional measurement techniques (e.g., fluctuations in photon counts, photon antibunching, bunching, blinking, quantum jumps, spectral jumps, etc.). Analysis of these fluctuations reveals important information on dynamical processes occurring in the condensed phase as well as important information on the distribution of nanoenvironments [130].

Another crucial single-molecule technique is single-molecule force spectroscopy, where single molecules (or a pair of interacting molecules, oligomers and polymers) are mechanically stretched and their elastic response is recorded in real time [131]. In single-molecule force techniques, the structural property can be studied in detail, but the functional aspect is not known whereas in single molecule fluorescence studies, the functionality is studied, but the structure or morphology normally ignored [132]. In this context, scanning near-field optical microscopy (SNOM) has emerged as the tool in which both structure as well as the functionality of the single molecules can be studied simultaneously [105]. Typically, the resolution of SNOM imaging is well beyond the classical diffraction limit. Furthermore, the simultaneous topographical mapping provides insight into the structural landscape surrounding the molecule under study.

bR patches can be grown as an oriented-monolayer on different substrates [93, 133]. The molecules within this patch are oriented, leading to a large optical anisotropy (in plane/out-of plane). The macroscopic patch-properties are representative of the oriented single molecule and not an ensemble average of isotropic un-oriented molecular system. The change in the

photophysical parameters or the local environment can change the absorption spectrum of bR. The shifting of the absorption spectrum will generate amplitude fluctuations in the detected transmission signal, which can be analyzed to provide insight into the underlying photophysical processes. The quantum efficiencies for the proton translocation can be determined and the reasons for deviations from the ensemble averaged values can be examined. The long-lived M-state of the protein can be tapped specifically using an additional photo-excitation source and its contribution can be used to identify the actual active-region from the entire scanned region. *This pump induced feature on top of a regular probe-scan is a clear signature that can be used to identify and quantify the protein functionality.*

In this chapter, a transmission SNOM based technique to identify and study bR monolayers on various underlying substrates, active (conducting polymer) and passive (quartz) is demonstrated. The technique compliments existing methods to study such functional membrane proteins by providing additional insights into the electronic processes and estimates of the quantum efficiencies of the photocycle of the molecule.

3.1 Electrostatic Layer-by-Layer Assembly

Polyaniline and bR are charged polycations and polyanions respectively. They can be grown in a controlled manner using LBL techinque. Monolayers of bR were grown on both quartz and polyaniline substrates using the electrostatic LBL assembly as described in the following sections.

3.1.1 bR on Quartz

The purple membrane (PM) patches were suspended in Milli-Q water, ≈ 0.5 mg/ml, pH ≈ 9.2 with TRIS (tris-(hydroxymethyl)aminomethane) as the buffer to maintain the pH. Quartz substrates were cleaned using piranha solution (H_2SO_4:H_2O_2 3:7) and rinsed with copious amount of water. The cleaned quartz substrates were stored in a beaker filled with Milli-Q water. This cleaned quartz substrate was blow dried using nitrogen gas and was immersed in 1:10 APTMS (3-aminopropyl triethoxy-silane):methanol solution for 3 hrs. This dipped quartz substrate was rinsed with copious amount of methanol to wash off the excess APTMS. This APTMS treated quartz substrate was then immersed in 0.1 M HCl solution for 5 mts. The APTMS on the surface of the quartz acquired a positive charge due to the protonation of the amine nitrogen by the acid solution. This positively charged quartz subsrtate was then immersed in PM solution (15 mts) and followed by a 2 mts rinsing process in a buffer solution of equivalent pH. This was followed by a drying procedure (using nitrogen flow) to obtain monolayers of PM patches [133]. These films were characterized by absorption spectroscopy to ascertain the presence of bR and to obtain a rough estimate the thickness ($\sim$ 13 nm) (Fig. 3.1).

3.1.2 Polyaniline

Polyaniline, emeraldine base powder, from Aldrich (Mw = 20,000), was dissolved in NMP (20 mg/ml) to form a homogenous solution. This solution was then sonicated for 3 hrs and this sonicated solution was then filtered in

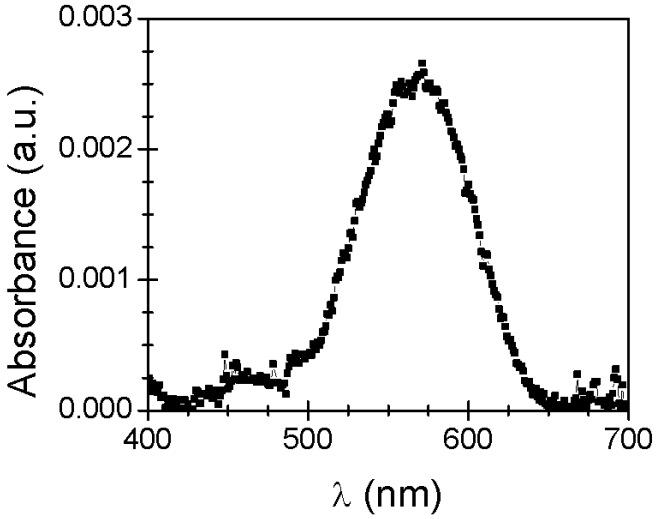

Figure 3.1: *Absorption spectra of monolayer of bR on quartz.*

a 0.45 μm filter. To this filtered solution, water at $\sim$ 3-3.5 pH was added (9:1, water:polyaniline solution). The pH of this solution was decreased to $\sim$ 2.5-2.6 using 1M HCl thereby transforming the polyaniline solution from the base to salt form (non-conducting to the conducting). This pH 2.5 solution was then filtered using a 0.22 μm filter [134] and this solution was used for the preparation of the polyaniline thin film using LBL technique.

3.1.3 bR on Polyaniline

The procedure adopted by us to prepare monolayers of polyaniline was first shown by Rubner et. al [134]. Precleaned quartz substrate was sonicated in a solution containing EtOH:$(CH_3)_2O$:$CHCl_3$ in the ratio 2:1:1 for 2 hrs followed by sonication for 2 hrs in 2% KOH solution. The quartz substrate was then blow dried using nitrogen to give a negatively charged quartz substrate. This negatively charged quartz substrate was then immersed in the polyaniline

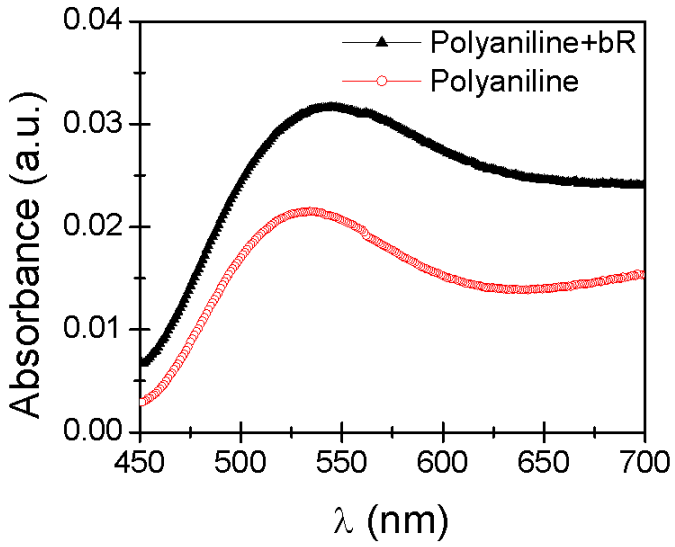

Figure 3.2: *Absorption spectra of polyaniline and bR on polyaniline.*

emeraldine salt solution for 15 mts to form a thin layer of polyaniline. The film was then gradually rinsed with 0.1 M HCl solution for 2 mts and then dried under nitrogen flow. This polyaniline coated quartz substrate was then immersed in a Tris buffer solution for 10 mts to obtain the original base form and the films were again dried under nitrogen flow. These films were then characterized by absorption spectroscopy (Fig. 3.2).

This polyaniline coated quartz substrate was then immersed in the bR solution (15 mts) to obtain a monolayer of bR on the polyaniline film. This bR coated polyaniline film was rinsed again using copious amounts of Tris solution and dried under nitrogen flow. These films were characterized by absorption spectroscopy (Fig. 3.3) to find out whether PM patches adhered to the polyaniline films and the thickness of the PM films estimated roughly was $\sim$ 6 nm.

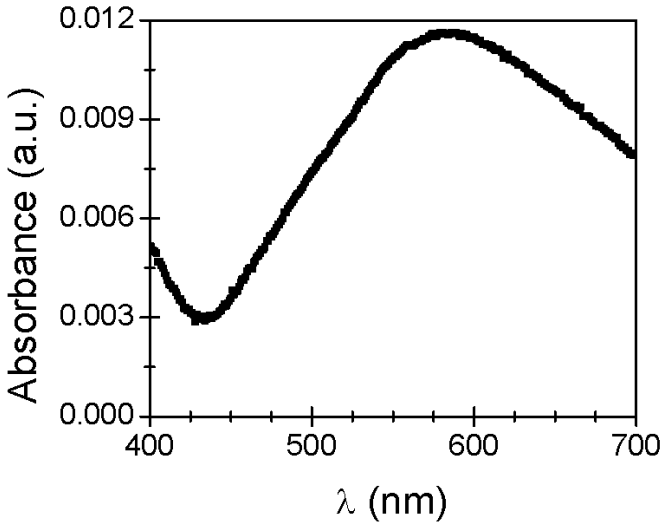

Figure 3.3: *Difference spectra from Fig. 3.2.*

3.2 Near-field Microscope

The experimental set-up around SNOM is unique in many different aspects and has been designed to target the specific problem of a two state molecule. The setup used for near-field optical microscopy (Multiview 4000, Nanonics Inc.) was based on an inverted optical microscope (OLYMPUS) that is combined with a scanner base and a scan head. A normal force feedback mechanism provided tip-sample distance control. In a typical experiment, 532 nm laser was coupled to the SNOM probe tip (diamter $\sim$ 100 nm) using a fiber optic cable. The optical signal (transmission in the present case) was measured using a PMT through the objective (50X, N.A = 0.45). Simultaneous optical and topographical information were obtained from the Near-field Optical Microscope by raster scanning the sample using the piezo scanner in such a way that the tip and the objective lens are maintained at the same position with respect to each other.

A transmission-SNOM procedure used to study the 3-level transmembrane protein was as follows (Fig. 3.4): The topography and corresponding optical map of the sample (probe laser, λ = 532nm or 405 nm) were simultaneously recorded using a custom made software provided by Nanonics Inc. An additional laser (λ = 405 nm or 532 nm, depending on the experimental conditions) was introduced through the objective of the inverted microscope (Fig. 3.4) to illuminate the same spot as that of the SNOM probe. The diameter of the spot of the additional pump beam was $\approx$ 1.5 μm. Hence, the pump beam completely envelops the probe beam. Band pass filters specific to probe wavelengths were used to cut-off the pump wavelengths. Also, it was noted that there was no change in the PMT values upon introducing the pump laser. Raster scanning was done with the presence and absence of a pump to obtain the PI-SNOM and SNOM images.

The data was analyzed using WS×M software [135]. In the cases of SNOM and PI-SNOM, the regions devoid of bR, as expected had the maximum transmission values. This maximum value of the PMT counts was set to 0 kHz. When the tip was positioned on the bR patch, the PMT counts decreased due to the finite absorption from the sample. Thus, the recorded counts on PMT was lower than that of the bare quartz and hence the values obtained after subtraction corresponds to negative numbers and these values in the negative range are essentially due to the normalization procedure adopted by us.

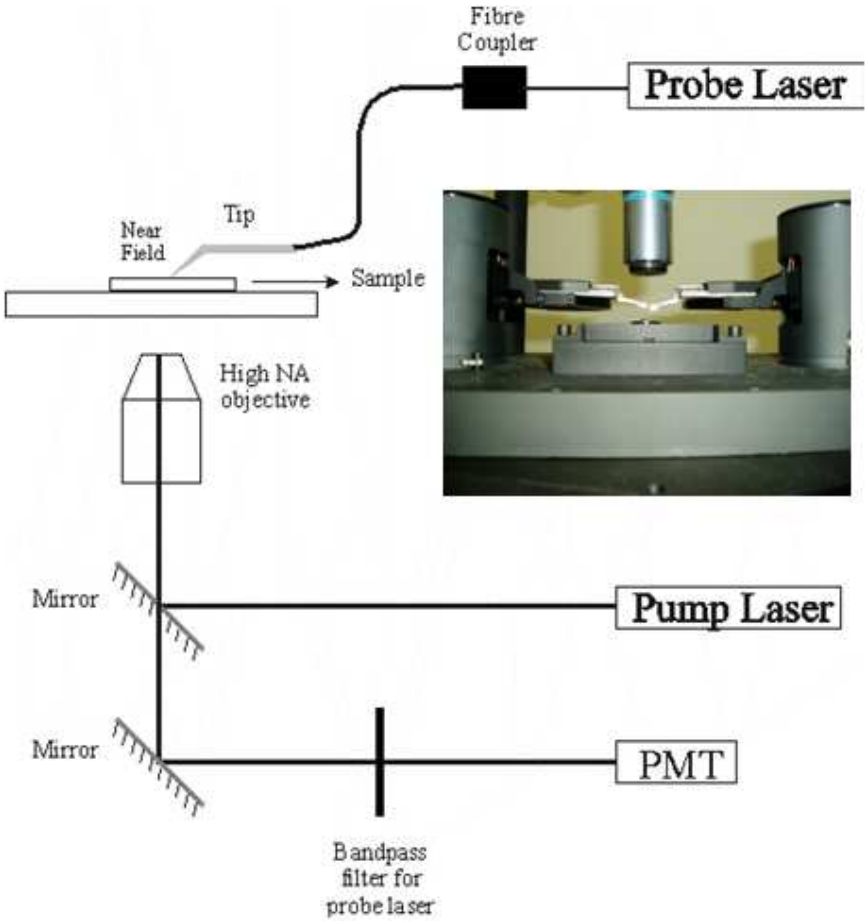

Figure 3.4: *Schematic of the SNOM experiment. Additional laser coupled through the objective, was used as the pump source for the PI-SNOM measurement. Inset shows the optical images of the tips.*

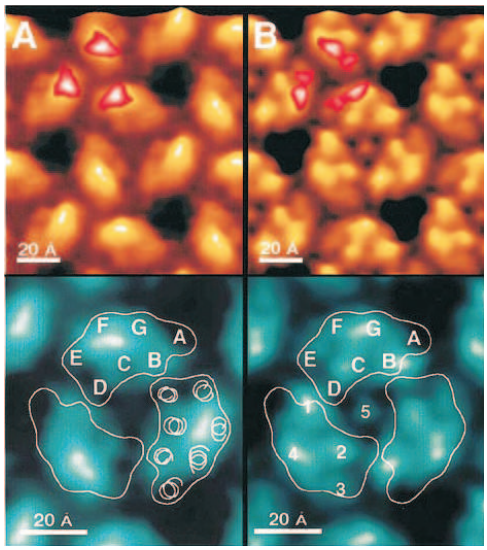

Figure 3.5: *High resolution AFM image of monolayers of bR adapted from Muller et. al.* ***J. Mol. Biol.****, 1999, 285, 1903.*

3.3 Transmission SNOM of bR

The established procedure of growing bR monolayers on quartz substrate was used to obtain a reasonably large patch-coverage ($> 80\%$) with the cytoplasmic side on the substrate [93, 133]. High-resolution atomic force microscopy (AFM) measurements have revealed that the proteins are packed in trimers and these trimers are then packed hexagonally within the purple membrane patches (Fig. 3.5) [136]. The fine structures revealing the trimer arrangements and its hexagonal packing expected from an AFM topography scan [136] are not visible in the present scans due to the large diameter of the SNOM probe (≈ 100 nm). However, the AFM scans in our case was used to identify the bR-patch region and its corresponding thickness. The SNOM probe was coupled to different monochromatic sources and was utilized to study the monolayer bR system.

Considering the standard probe diameter used ($\approx$ 100 nm), the total area enveloped by the beam is 7850 nm^2. The area of each bR molecule, established from crystallographic structure, is around 11.5 nm^2 [137]. Using a packing density of 76% for hexagonal ordering, the no. of trimer structures present within the beam area is $\sim$ 110 and the total number of molecules is $\approx$ 340. The optical response of the narrow confined beam from the SNOM probe essentially arises from these limited set of aligned trimer structures within a single patch. This forms a better probe to ascertain the oscillator strengths of individual molecule rather than the stochastic value measured from a very large number of molecules during absorption measurements done in the quartz liquid cell or on solid films, where the beam area is large ($\approx$ 5 mm^2).

3.3.1 bR on Quartz

In a typical scan of the monolayer, patches of $\approx$ 5.5-6 nm in height and around 0.5-1 μm in diameter were observed. This is in agreement with the earlier results observed by Muller et. al [136]. Fig. 3.6A shows the topographic image of a single PM patch and Fig. 3.6D the corresponding line profile. Fig. 3.6B shows the simultaneous near-field transmission image when λ = 532 nm was coupled to the SNOM probe. Fig. 3.6E is the line profile of the near-field transmission change showing that the transmittance (λ = 532 nm), from the bR-patch corresponded to 99.1% as compared to that of the quartz substrate. Upon introducing an additional pump (λ = 405 nm) through the objective (Fig. 3.4) and scanning at the same location, the transmittance

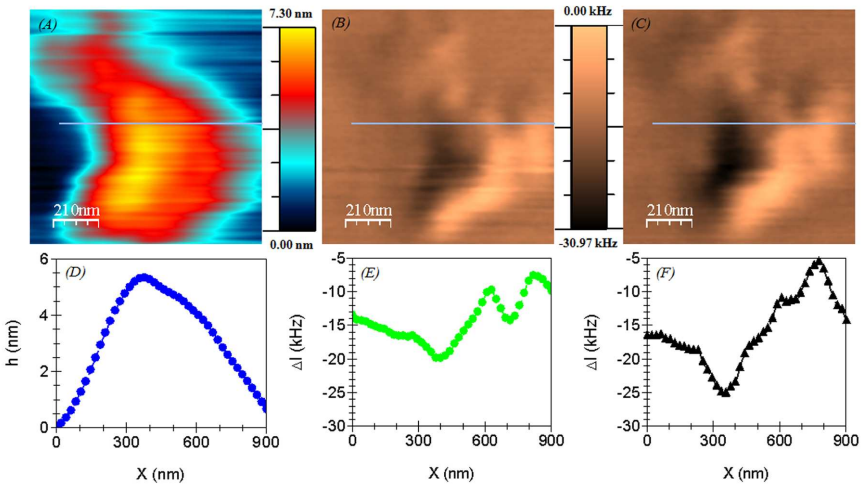

Figure 3.6: *(A) The AFM image, (B) Transmission SNOM image and (C) Pump-Induced Transmission SNOM image of a monolayer of bR patch with $\lambda = 532$ nm through the tip and the pump beam at $\lambda = 405$ nm. The scale is equalized for (B) and (C). Line profiles of the corresponding AFM image (D), SNOM image (E) and Pump-Induced Transmission SNOM image (F). Scan area 1 $\mu m \times 1$ μm.*

decreased further as shown in Fig. 3.6C. The line profile of the PI-SNOM in Fig. 3.6F showed that the near-field transmittance decreased to 98.9%. This increase in absorption is clearly seen in Fig. 3.7 where the average value of the PMT counts is shifted to the lower number (implying that there is reduced transmission through bR monolayer with respect to quartz substrate) upon introducing an additional pump laser ($\lambda = 405$ nm).

While scanning different locations, it was observed that there were regions within the sample where the height of the patches was more than 6 nm. The measured height of these samples were in multiples of 6-7 nm. Hence, these topography structures were attributed to monolayers stacking up to form multilayers. As the thickness of the sample increased, the number of molecules present within the volume of the beam increased. This leads to increased absorption during the SNOM experiments. The corresponding

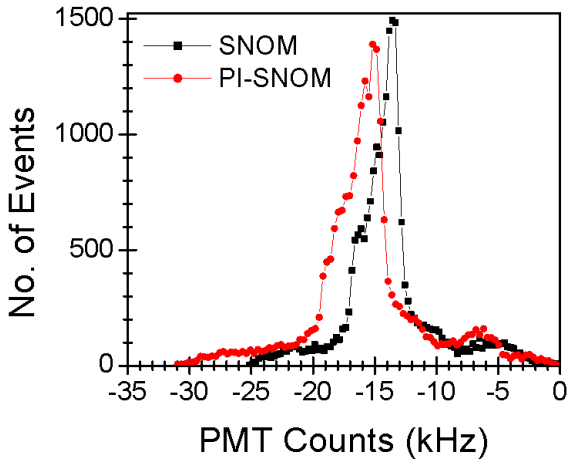

Figure 3.7: *The No. of Events as a function of PMT counts for a monolayer of bR with and without the presence of an additional pump (λ = 405 nm).*

increase in absorption in the PI-SNOM experiments was also observed (Fig. 3.8).

To further confirm that the near-field transmission measurements are related to bR and not due to features arising from the substrate, interfaces and other spurious sources, we performed the near-field transmission experiments with λ = 405 nm as the probe. The changes introduced by the additional pump, λ = 532 nm was also monitored as a proof for self-consistency (Fig. 3.9A). In the absence of any pump, all the molecules are present in the B-state and hence no absorption was seen (Fig. 3.9B). Upon, introducing the pump laser of λ = 532 nm, the photocycle is initiated. This populates the M-state, leading to a finite absorption during the PI-SNOM experiments of $\approx$ 0.15% (Fig. 3.9C). The typical line profiles of the AFM, NSOM and PI-NSOM measurements are shown in Fig. 3.9D, 3.9E and 3.9F.

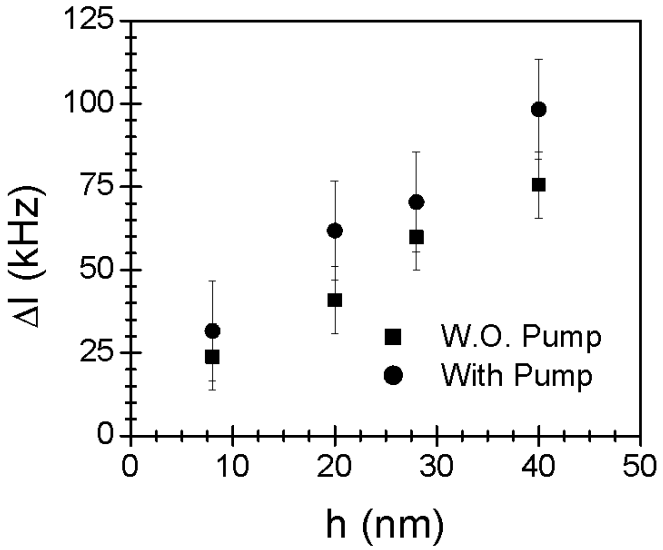

Figure 3.8: *The change in transmission (ΔI=I_0-I) measured as a function of the thickness of bR patch for SNOM and PI-SNOM experiments.*

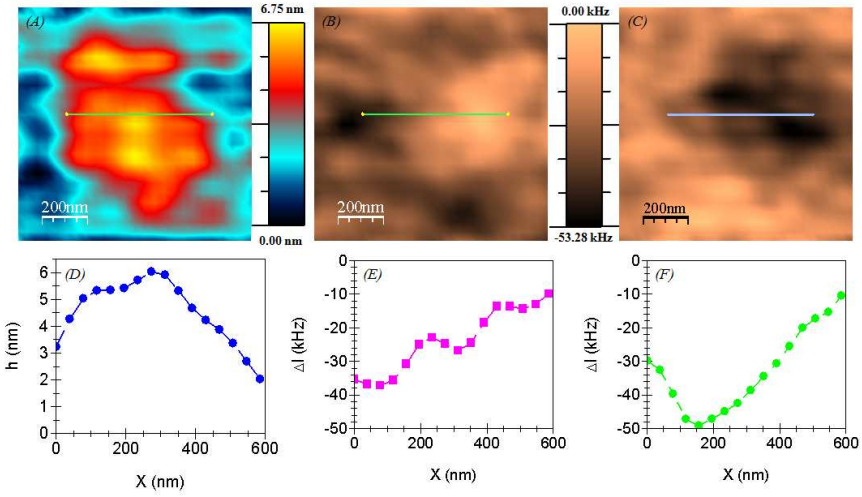

Figure 3.9: *(A) The AFM image, (B) Transmission SNOM image and (C) Pump-Induced Transmission SNOM image of a monolayer of bR patch with λ = 405 nm through the tip and the pump beam at λ = 532 nm. The scale is equalized for (B) and (C). Line profiles of the corresponding AFM image (D), SNOM image (E) and Pump-Induced Transmission SNOM image (F). Scan area 0.75 μm × 0.75 μm.*

3.3.2 bR on Polymer

When, the underlying substrate was modified from quartz to an active layer consisting of conducting polymer (Polyaniline), it was noted that bR was oriented only on the polyaniline (Pani) and not on the underlying quartz substrate. This was confirmed by the absence of any 5-6 nm patches in the topography images. Fig. 3.10A shows the AFM topographic image of bilayer consisting of bR and underlying Pani layer (scan area 1.5 μm $\times$ 1.5 μm). The corresponding SNOM image is shown in Fig. 3.10B. The PI-SNOM on the same area is shown in Fig. 3.10C. The line profiles of the AFM topography, SNOM and PI-SNOM are shown in Fig. 3.10D, 3.10E and Fig. 3.10F. The corresponding decrease in the transmittance of SNOM experiments with $\lambda =$ 532nm is 99.0%. However, in the PI-SNOM measurements with an additional pump with $\lambda = 405$ nm, the transmittance further decreased to 98.4% which is solely attributed to the optically induced changes in the bR layer. This increase in absorption is clearly seen in Fig. 3.11, where the average PMT counts shifted to lower values upon introducing an additional pump laser (λ = 405 nm).

3.4 Discussion

The rate at which a system is excited is proportional to the absolute square of the component of the exciting electric field E along the direction of the absorption dipole moment, μ [138]. The power absorbed by the system is given by

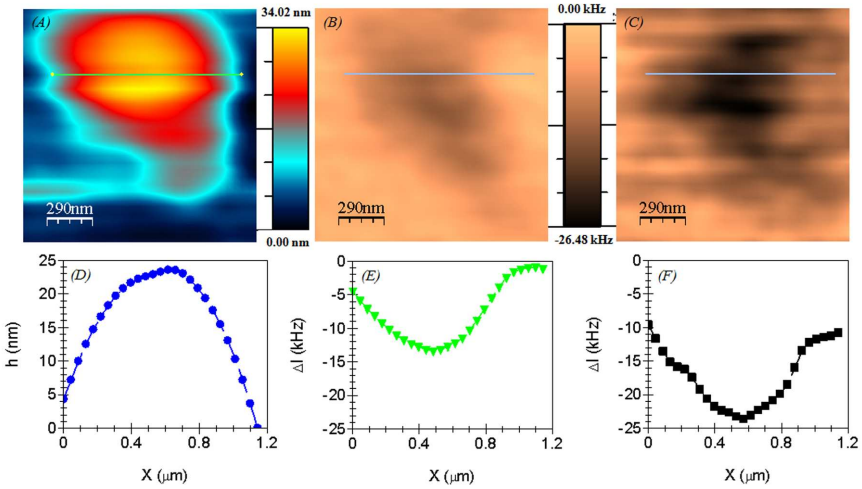

Figure 3.10: *(A) The AFM image, (B) Transmission SNOM image and (C) Pump-Induced Transmission SNOM image of a monolayer of bR patch on a conducting polymer PANI, with λ = 532 nm through the tip and the pump beam at λ = 405 nm. The scale is equalized for (B) and (C). Line profiles of the corresponding AFM image (D), SNOM image (E) and Pump-Induced Transmission SNOM image (F). Scan area 1.5 μm × 1.5 μm.*

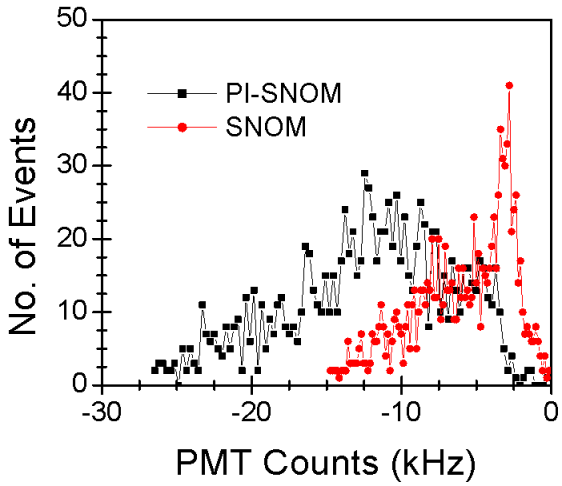

Figure 3.11: *The No. of Events as a function of PMT counts for a monolayer of bR on conducting polymer with and without the presence of an additional pump (λ = 405 nm).*

$$P = \frac{\omega}{2} Im\alpha \left| n_p \cdot E \right|^2 \tag{3.1}$$

where n_p is the unit vector in the direction of the transition-dipole moment, $p = \alpha \cdot E$ and α is the atomic polarizability tensor [138]. Therefore, a monochromatic field with angular frequency ω produces a harmonically oscillating dipole with the same frequency. The geometry adopted by the transition-dipole moment forms the basis for the orientation dependence during absorption process [139]. From the X-ray crystal structure, NMR and linear dichroism studies [69, 140, 141], it is known that the orientation of the retinal chromophore is at an angle with respect to the membrane plane. It is already known, that this retinal chromophore is the moeity which absorbs the light of visible range leading to photocycle. Thus, the transition dipole moment is located on this retinal chromophore (Fig. 3.12). In the procedure adopted by us, bR is oriented with its cytoplasmic side facing the quartz substrate (due to the charge based interaction). Hence, the major component of the transtion-dipole moment, (p) is in the direction of membrane normal (z-direction) which implies that the major component of α is also along the z-direction. The presence of evanescent waves leads to a quazi-stationary electric field (E_x, E_y, E_z) (Fig. 3.12) at the vicinity of the tip [142, 143]. Since the power absorbed by the system scales as the square of the electric field projected along the transition dipole moment [138], the interaction between this quazi-stationary electric field with the tensoral form of the atomic polarizability $(\alpha_x \cdot E_x)^2$, $(\alpha_y \cdot E_y)^2$ and $(\alpha_z \cdot E_z)^2$ results in the enhanced near-field absorption.

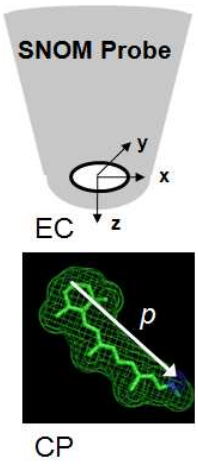

Figure 3.12: *Schematic showing the Electric field emanating from the near-field probe and the orientation of the transition dipole moment on the retinal chromophore with respect to it.*

3.4.1 bR on Quartz

The fraction of molecules entering the photocycle is arbitrary, i.e. the bR population is functionally heterogenous. The percentage of bacteriorhodopsin molecules entering the photocycle after a single laser flash is ambiguous. The accumulation of the intermediates also overlap temporally, which results in an unknown mixture of intermediates present at any time before the completion of the photocycle [144]. But, often a very simple two-state model is good enough to approximate the photochemical conversions of bR [145, 146]. In the simplified two-state model, where the molecules are present in either of the two states, B-state or M-state, with $N_{tot} = N_B + N_M$ is valid at all times, where N_{tot} represents the total number of molecules and N_B & N_M represent the number of molecules in B-state and M-state at any given time. In this model, k_1 represents the photochemical reaction rate from B to M, which is dependent on the actinic light intensity I and its wavelength λ, i.e.,

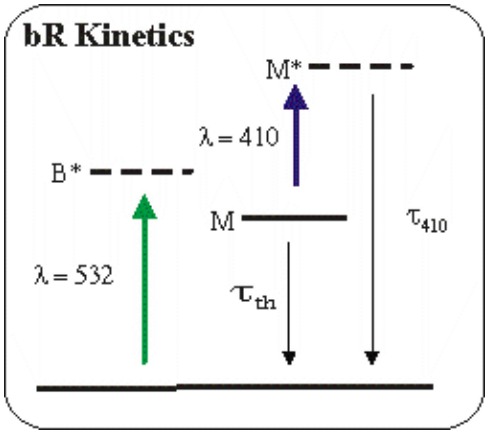

Figure 3.13: *The three state model corresponding to bR kinetics.*

$k_1 = k_1(I, \lambda) = \alpha(\lambda) \cdot I$. While, the M- to B- reaction rate k_2 is indirectly proportional to the M-lifetime τ_M, i.e., $k_2 = \tau_M$, as long as a simple first-order reaction is assumed.

The non-coherency of the photocycles can be characterized by a physical quantity known as the steady state intensity dependent ratio, γ_{SS}, that is given by the number of molecules in the M-state corresponding to the number of molecules in the B-state [147].

$$\gamma_{SS} = \frac{N_M^{SS}}{N_B^{SS}} = \frac{1}{\alpha(\lambda) I \tau_M} \tag{3.2}$$

This steady state population is dependent on the actinic light potential $\alpha(\lambda)I$ and also on the life time (τ_M) of the M-state. This photocycle rate can be modified by the intervention of additional photoexcitation at the appropriate wavelength [148]. For example; upon introducing the additional 410 nm (in our PI-SNOM, pump $\lambda = 405$ nm), the life time, τ_M of the M-state is modified (Fig. 3.13) and hence the time taken for the completion of photocycle is reduced, modifying the steady state ratio, γ_{SS}. This decrease

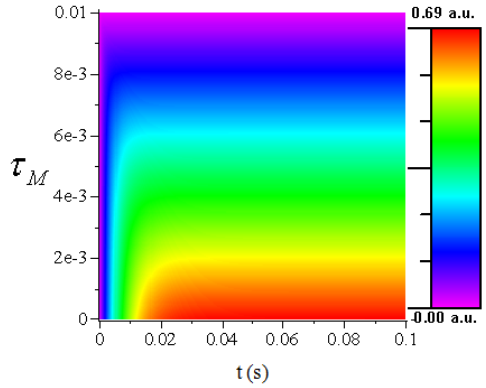

Figure 3.14: *The time (t) taken to reach the steady state value as a function of the life time (τ_M). The color bar represents the steady state ratio, γ_{SS}.*

in the steady state ratio (Fig. 3.14) leads to increased absorption of the PM patch as indeed observed from our PI-SNOM experiments.

The tip-sample interactions are known to modify the flourescence lifetime, [149] depending different situations. These interactions can also modify the transmitted intensity through the sample. The change in the transmission intensity from our near-field experiments can be used to calculate the effective molar absorptivity. The effective molar absorptivity $\epsilon(\lambda$=532 nm), calculated at the centre of the patch, using Beer-Lambert's law was $\sim$ 54.7 $\times$ 10^4 L/mol cm, which is an order of magnitude higher than the value (4.2 $\times$ 10^4 L/mol cm) found in the literature [147, 150]. Similarly, the effective molar absorptivity $\epsilon(\lambda$=405 nm) can also be found. Assuming, the earlier calculated quantum efficiency for photocoversion to be 76%, the total number of molecules present in the M-state is assumed to be 24%. Now, only these molecules absorb during the PI-SNOM experiment with an additional pump laser (λ = 532 nm). The $\epsilon(\lambda$=405 nm) was found to be $\approx$ 38 $\times$ 10^4 L/mol cm, which is also an order of magnitude higher than the values (4.9 $\times$ 10^4

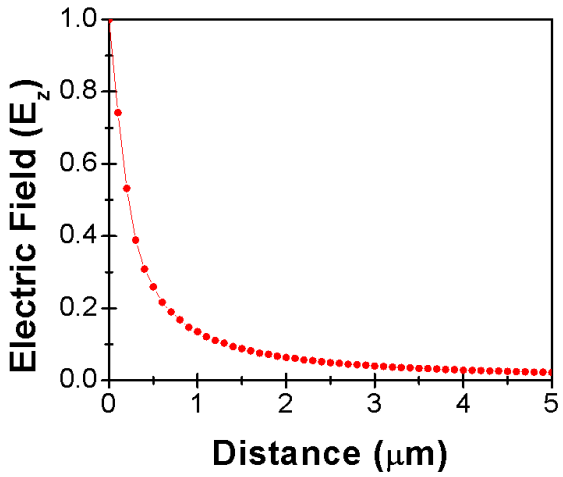

Figure 3.15: *E_z dacay profile away from the tip.*

L/mol cm) found in literature [150]. The higher $\epsilon(\lambda)$ is essentially due to tip-sample interaction.

From these measurements, we can also calculate the quantum efficiency of photo-conversion for a monolayer of bR patch. Assuming that all the bR molecules are either in B-state or in the M-state (a reasonable assumption), The steady state absorption during the PI-SNOM case is representative of all the molecules in ground state, (γ_{SS}, being close to zero), while in the SNOM experiments, γ_{SS} a finite value because of the non-coherency in the photocycle. Now, the ratio between the absorption during the SNOM experiments to that of the PI-SNOM experiments can be used to evaluate the quantum efficiency of the photo-conversion. This quantum efficiency for photo-conversion of bR was estimated to be 76%, is higher than the values in the literature [151].

As the thickness of the sample increased (from monolayers to multilayers), the number of molecules present within the volume of the beam increases leading to increased absorption during the SNOM experiments. This was indeed observed during the measurements, as shown in Fig. 3.8. The corresponding changes in the PI-SNOM experiment were also observed (Fig. 3.8). However, the effective strength of E_z from the tip decays exponentially ($e^{-\eta r}$) (Fig. 3.15) with r, the distance from tip, as SNOM is largely surface sensitive probe [143] and at a distance of about 500 nm from the tip E_z component is absent. Hence, the contribution to the interaction term in the direction of membrane normal decreases as the thickness of the film increases. The absorption from the upper layers of bR patches lying closer to the tip arises from the interaction of its dipole with transverse fields (E_x, E_y) as well as the longitudinal field (E_z), while the absorption of the bR patches lying near the quartz substrate, arises from the interaction of its dipole with the transverse fields (E_x, E_y).

It is known from literature that transmission SNOM based measurements are prone to artifacts [152–154]. The z-motion artifact generates features in the optical image that are highly correlated with the structures in the topographic image. To further confirm that the optical signals measured were due to the sample and not due to artifacts or due to the heating of the tip upon shining an additional laser, experiments were performed in different modes (constant height and constant gap modes), the results of which are summarized in the following table. A detailed description and analysis of these experiments is provided in Appendix B.

Further, to prove that the transmission is due to the presence of bR

Mode	**Probe** λ (nm)	**Pump** λ (nm)	**% Transmission** Error bar $\pm 0.1\%$
Bare Quartz			100
Constant Gap	532	-	99.1
Constant Height	532	-	99.2
Constant Gap	532	405	98.9
Constant Gap	532	570	99.4
Constant Gap	532	670	99.2
Constant Gap	405	-	99.9
Constant Gap	405	532	99.7

Table 3.1: *The effect of different scanning modes and pump on the measured transmission.* ϵ *of the monolayers can be calculated. See text for details.*

on the substrate and not due to artifacts or dust particles, different pump wavelengths were used. A pump of $\lambda = 405$ nm decreases γ_{SS} by decreasing the lifetime of the intermediate M-state, whereas a pump of $\lambda = 570$ nm increases γ_{SS} by populating the intermediate M-state. Finally a pump $\lambda = 670$ nm does not modify γ_{SS} as the intermediates in the bR photocycle do not absorb at significantly at that λ. Hence, the tranmission through the bR patch should be lower when pumped with $\lambda = 405$ nm and higher when pumped with $\lambda = 532$ nm and there is no change in the transmission is similar to the measurements without any pump. This is indeed observed in the measurements as summarized in the above table (See Appendix B).

These results clearly reveal the presence of a transition dipole moment component along z-direction which forms the basis for the near-field interactions (Fig. 3.12) in both the cases (532 nm and 405 nm from the tip). Our estimates indicate that the effective molar absorptivity decreased from a factor of 13 when probed with $\lambda = 532$ nm to a factor of 8 when $\lambda = 405$ nm was used as the probe. Since, the near-field interaction strength depends on

the polarizability α_z and the electric field in the z-direction, the results point to the larger presence of the parallel component of the atomic polarizability (α_z) (along z-direction) in the B-state compared the M-state [155].

3.4.2 bR on Polymer

Upon photoexcitation of bR on Pani substrates, protons are translocated from the cytoplasmic side to the extracellular side [156]. In polyaniline systems, high conductivity has been observed through the protonation of the imine nitrogen atoms in its emeraldine oxidation state [157]. Pani being a good source/sink for protons, has a greater affinity for protons, leading to the depletion of protons in or around the vicinity of bR. The absence of a proton source to the cytoplasmic side of bR, tends to stabilize the bR in the M-state. This increases the life-time of M-state and hence increases the time taken for bR to the complete of the photocycle. Upon introducing an additional pump laser $\lambda = 405$ nm, the photocycle is completed effectively leading to an increase in PI-SNOM measurements. Both, the steady state ratio, γ_{SS} and the calculated quantum efficiency is 63%, are lower than the values observed on the quartz substrate.

3.5 Conclusions

A SNOM based approach was introduced which provides valuable insight on non-fluorescent systems on a single molecule level, such as bR in terms of the orientation and the efficiency of the photocycle on different substrates. The

transmission changes were directly correlated to the electronic processes occurring within bR and the increased absorption in the near-field case was attributed to the additional electric field, (E_z) component. Absorption changes provided quantitative assessment of the photocycle including the distribution of the population densities in the different intermediate states. Spatial and temporal features of the bR photophysical processes were directly studied upon introduction of a pump source corresponding to the specific intermediate state. The comparison of the quantum efficiency for different underlying active substrates gives a measure of the interaction strengths and was utilized to study and control the dynamics of the photophysical processes in bR.

Chapter 4

Electric-field Induced Surface Deformations on Soft Polymer Films

An external electric field modifies both metallic (liquid) and dielectric (visco-elastic) surfaces leading to the formation of different surface patterns. In the metallic liquid case, the electric field deforms the surface leading to a complete intimate contact, whereas in the visco-elastic dielectric case, deformation in the form of periodic patterns appear on the surface. The mechanics of contact, adhesion and friction between solid bodies is an important area of research owing to the underlying scientific challenges. More recently, there has been interest in understanding the contact and adhesion mechanics between two elastic bodies. The formation of self-organized instability structures in a thin liquid film [158–169] and a soft solid polymer film [170–172] is of great interest in diverse scientific and technological applications involving functional

interfaces (adhesion, wetting, optics, etc.) and meso-patterning [164–169], especially with an applied electric field [166–169, 173].

The application of an electric field destabilizes the film surface leading to its deformation, whereas other interactions such as viscosity, surface tension, elastic surface energy and various other interactions act to stabilize the film surface and prevent its deformation. In this chapter, the effects of application of an external electric field on a thin dielectric film, both in parallel and inclined geometry are studied. In parallel geometry, the role of visco-elasticity or rheology in the process of spinodal pattern formation in a thin film destabilized by a field is investigated and the transition from viscous to elastic behavior studied, whereas in the inclined geometry, the role of visco-elasticity in the evolution of the final morphology is studied.

4.1 Parallel Geometry

The physical basis for the deformation of a liquid surface by an electric field has been known for more than a century [174]. Electrohydrodynamic instabilities have been studied for a wide variety of liquids. In a thin-film geometry, research on the film stability is a field of rapidly growing activity due to the fundamental interest in the interactions of liquids near surfaces. As opposed to other interactions, the strength of electrostatic forces can be easily varied and, due to their long-ranged nature, a coupling of electrostatic interactions to dielectric interfaces far from the external surface of the specimen is possible, leading to the formation of patterns.

The effect of electric field in viscous liquid like films is predicted by the

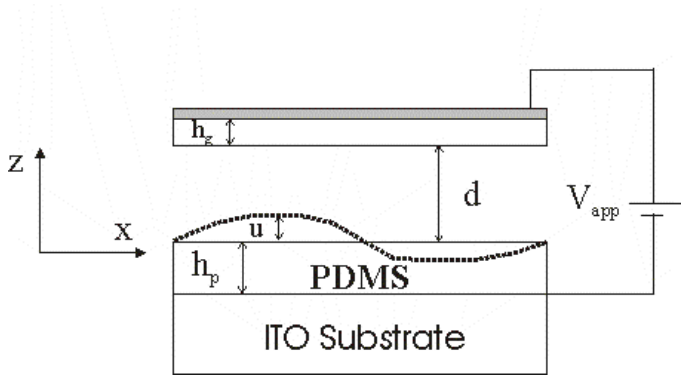

Figure 4.1: *Schematic of the model used to explain the effect of electric fields.*

electrohydrodynamic instability theory. The application of electric field modifies the overall pressure distribution of the system, which is given by [173],

$$p = p_0 - \gamma \frac{\partial^2 h}{\partial x^2} + p_{el}(h) + p_{dis}(h), \tag{4.1}$$

with p_0 being the atmospheric pressure. The second term, the Laplace pressure, stems from the the surface tension γ and the fourth term, the disjoining pressure p_{dis}, arises from dispersive van der Waals interactions. The electrostatic pressure for a given electric field in the polymer film, E_p=$U/(\epsilon_p d$-$(\epsilon_p$-$1)h)$, is given by p_{el}=-$\epsilon_0\epsilon_p(\epsilon_p$-$1)E_p^2$. For high enough values of E_p, only the Laplace and electrostatic terms need to be considered. In a stability analysis, a small sinusoidal perturbation (Fig. 4.1) of the interface with wave number q, growth rate τ^{-1}, and amplitude u is considered: $h(x,t)$=h_0+$ue^{iqx+t/\tau}$. The modulation of h gives rise to a lateral pressure gradient inside the film, inducing a Poiseulle flow j [175]

$$j = \frac{h^3}{3\eta}(-\frac{\partial p}{\partial x}) \tag{4.2}$$

where η is the viscosity of the liquid. The continuity equation enforces mass conservation of the incompressible liquid:

$$\frac{\partial j}{\partial x} + \frac{\partial h}{\partial t} = 0 \tag{4.3}$$

Eqns. 4.1, 4.2 and 4.3 establish a differential equation that describes the dynamic response of the interface to the perturbation. In a linear approximation (to order $O(u)$), a dispersion relation is obtained:

$$\frac{1}{\tau} = -\frac{h_D^3}{3\eta}(\gamma q^4 + \frac{\partial p_{el}}{\partial h} q^2). \tag{4.4}$$

As opposed to the inviscid, gravity-limited case ($\eta^{-1} \propto q$) [4], the viscous stresses lead to a q^2-dependence of η^{-1} in the long-wavelength limit, typical for dissipative systems [176]. Fluctuations are amplified if $\tau > 0$. Since $\frac{\partial p_{el}}{\partial h} < 0$, all modes with $q < q_c = \sqrt{-\frac{1}{\gamma}\frac{\partial p_{el}}{\partial h}}$ are unstable. With time, the fastest growing fluctuation will eventually dominate giving rise to periodic patterns with characteristic wavelength λ, corresponding to the maximum in Eqn. 4.4

$$\lambda = 2\pi\sqrt{\frac{\gamma U}{\epsilon_0 \epsilon_p (\epsilon_p - 1)^2}} E_p^{-\frac{3}{2}} \tag{4.5}$$

$$\lambda \sim E^{-\frac{3}{2}} \tag{4.6}$$

where λ is determined solely by a competition between the destabilizing force and the surface tension, but not by the factors that influence the kinetics, such as high frequency elasticity and viscosity, both of which vary greatly in the CL range of 0-1%. An important point of note is that there

is no lower threshold field for the electrohydrodynamic instability, due to the dissipative character of the viscous drag that opposes the destabilizing electrostatic force. In practice, other destabilizing contributions to the pressure balance in Eqn. 4.2 have to be considered for low values of p_{el}, such as dispersion forces, nucleation effects, etc.

4.2 Inclined Geometry

Recently, a new kind of elastic meniscus instability was reported [170], that develops merely by contacting a glass plate with a thin elastomeric film bonded to a rigid support, i.e., the situation of crack closing in a confined elastic film. The instability was triggered by van der Waals and/or electrostatic interactions near the contact zone of the cover glass, which also manifests in the energy of adhesion, normal stresses and deformation near the contact line. The wavelength (λ) and amplitude (u) of these instabilities are the two most important geometrical features that describe the morphology of the waves. It was observed that the wavelength increases linearly with thickness (h) of the film, but it was relatively independent of either the elastic modulus of the film or the flexural rigidity (D) of the top cover glass.

4.2.1 Interaction Energy

The total potential energy of the system consists of the elastic energy in the film (stabilizing), energy of interaction with the cover beam (manifested in normal stresses causing deformation) and the surface energy of the film (stabilizing, but usually negligible), is given by

$$\Pi_{EL}(u) = \int_V dV W(E) + \int_S \left(\gamma \sqrt{1 + (u_{2,1})^2} - U(u \cdot n) \right) dS \tag{4.7}$$

where $W(E)$ is the strain energy density, E is the strain tensor (gradient of displacements), γ is the surface energy, $U(n \cdot n)$ is the interaction potential between the surface of the film and the external agency such as a contactor or an electric field, u is the displacement vector, n is the outward normal to the surface and V is the volume of the film [171].

$$\Pi_{EL}(u) = \int_V dV W(E) + \int_S \left(\gamma \sqrt{1 + (u_{2,1})^2} \right) dS - \int_S \left(U_0 + F_o u \cdot n + \frac{1}{2} Y (u \cdot n)^2 \right) dS \tag{4.8}$$

Linearization produces $U_0 = U(0)$, $F_o = U'(0)$ and $Y = U''(0)$, where (0) denotes the undeformed film configuration. A full solution of the problem, considering the equilibrium stress fields (consisting of both the elastic and viscous stresses) with appropriate boundary conditions shows that there exists a homogeneous solution. The equilibrium stress field σ in the film satisfies the equilibrium equation $\nabla \cdot \sigma = 0$ in V and the boundary condition on S.

$$\sigma \cdot n = \gamma u_{2,11} n + F_0 n + Y (n \cdot n) n \tag{4.9}$$

There exists a homogeneous solution, which shows periodic deformations of the form $u \sim exp(ikx_1)$. This periodic deformation ensues whenever Y exceeds a critical value,

$$Y > 6.22\mu/h \tag{4.10}$$

The wavenumber ($k = 2\pi/\lambda$) of the instability is independent of both μ and the energy of adhesion. For nearly incompressible materials, and for small values of surface energy ($\gamma/\mu h << 1$), it was shown that [177],

$$hk_c = 2.12 - 2.86(1 - 2\nu) - 2.42(\gamma/\mu h) \tag{4.11}$$

Since, in the elastic case ($\gamma/\mu h << 1$), this produces a linear variation $\lambda = 2.96h$. These instabilities, while profoundly influencing the adhesion/debonding characteristics [178], also provide an attractive route to patterning and morphological control of soft thin films by external interactions. However, intermolecular interactions, being material properties, cannot be easily modulated. Moreover, these interactions are short-ranged and thus even nanometer-scale surface roughness and defects affect the robustness of these patterns. The application of an electric field modulates the morphology, dimensionality, and the adhesive strength of surface patterns.

4.2.2 Electrostatic Energy

An energy functional keeping only the electric field effects as a first approximation was developed and the contribution of van der Waals force was ignored as the changes were observed even at large d (> 100 nm). The electric field produced in the gap (Fig. 4.1) acts to promote morphological changes; in particular, the electric field acts as a destabilizing force. The stabilizing influence in the system, arises from the elastic energy of the nearly

incompressible films. The effective electrostatic energy of the film is [179]

$$\Pi_{ES}(Q,\phi) = \frac{1}{2}CQ^2 - \phi Q \tag{4.12}$$

where C is the effective capacitance of the part of the system of interest, ϕ is the effective voltage drop across the air gap of thickness d and the PDMS film (Fig. 4.1), and Q is the as-yet-undetermined charge stored. For a given voltage ϕ, the charge that builds up in the system minimizes the electrostatic potential energy [180] Π_{ES} and equals $Q{=}\phi/C$. The electrostatic energy in terms of the potential, ϕ can be expressed as

$$\Pi_{ES} = -\frac{1}{2}C\phi^2 \tag{4.13}$$

The effective capacitance per unit area C of the this capacitor is given by

$$C = \frac{\epsilon_0\epsilon_p}{d\epsilon_p + h} \tag{4.14}$$

where $(h + d)$ is the total gap filled partially with a dielectric material (dielectric constant, ϵ_p) to a thickness h and with the air gap d and ϵ_0 is the permittivity of vacuum. Surface deformation increases the film thickness from h to $(h + u)$, where u is the normal displacement of the film surface along the z direction (Fig. 4.1). The local air gap thus changes to $(d - u)$, and the resulting capacitance now is

$$C(u) = \frac{\epsilon_0\epsilon_p}{\epsilon_p d + h - (\epsilon_0 - 1)u} \tag{4.15}$$

It is evident that if $\epsilon_p > 1$ (a condition that is satisfied in PDMS films,

$\epsilon_p = 2.65$), the capacitance increases if the effective film thickness increases by a displacement of the film surface. In reality, the surface deformation u will not be a constant, especially because the film is nearly incompressible. In such a condition, an approximate expression for the effective capacitance can be obtained by using the expression for the capacitance per unit area $C(u)$ as

$$C = \int_A dxdyC(u(x,y)) = \int_A dxdy \frac{\epsilon_0\epsilon_p}{\epsilon_p d + h - (\epsilon_0 - 1)u(x,y)} \tag{4.16}$$

and, consequently, the electrostatic energy for the potential ϕ is now obtained as a functional of $u(x,y)$ as

$$\Pi_{ES}(u) = -\frac{1}{2}\int_A dxdy \frac{\epsilon_0\epsilon_p\phi^2}{\epsilon_p d + h - (\epsilon_0 - 1)u(x,y)} \tag{4.17}$$

which depends on ϕ^2 (not on the sign of ϕ), and A is the area of the film surface. As noted previously, there are two important approximations in writing Eqn. 4.17. The first is that u varies slowly compared with the thickness of the film, and therefore, the approximation using Eqn. 4.16 is not unreasonable. Second, the electrostatic potential distribution is consistently determined by the deformation of the film surface-this higher order effect was neglected. This could possibly be an oversimplification when studying the full nonlinear evolution of the film morphology but is not a serious limitation in the predictions of the critical voltage (to be explained later) for the onset of instability. This is because the deformations in the film before the onset of the electric field-induced instabilities are small, with the consequence that

the changes in electrostatic potential can be neglected.

4.3 Material - Polydimethyl siloxane (PDMS)

A wide variety of viscous and elastic films were prepared by varying the cross linker concentration in the two-part polydimethyl siloxane (PDMS) based elastomer, Sylgard 184 (Corning, USA). The cross linker (CL) percentage (which is usually about 10% for the soft lithography stamps) was increased to obtain increasing ratio of μ (elastic storage modulus) to G$''$ (viscous loss modulus), both of which were characterized by a Bohlin Rheometer. The films with cross-linker concentration, CL $< 1\%$ (μ/G$'' < 1$) corresponded to a liquid regime, whereas the films acquired a substantial permanent, zero-frequency elastic modulus when CL was in excess of 2% (μ/G$'' > 1$). The pre-polymer mix was diluted in n-Hexane for very thin films (1.5 μm - 10 μm) whereas for films thickness in the range of 10 μm - 75 μm the original pre-polymer mix was used. Films of different thickness were obtained by varying the spin coater speed (500 to 4800 rpm). The NIR absorption spectra showed interference features, from which the thickness of the films was calculated. Films were then annealed at 60 °C for 4 hours or 110 °C for 24 hours to obtain uniform films with surface roughness < 10 nm.

4.4 Experimental Procedure

The experimental setup for the electric field (EF) induced pattern formation involved placing the polymer film on the substrate electrode in the parallel

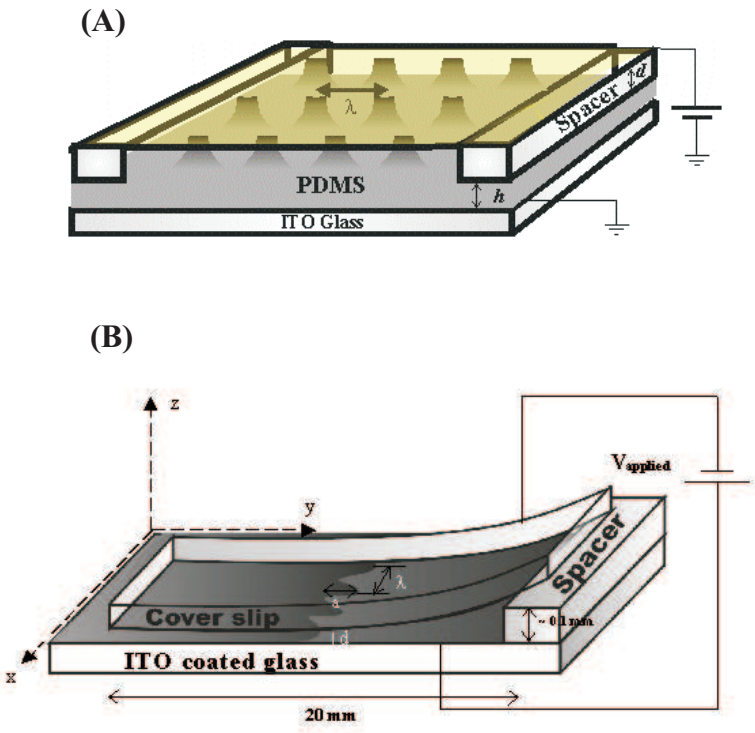

Figure 4.2: *Schematic of the experiments. (A) Parallel geometry and (B) Inclined geometry.*

geometry (Fig. 4.2A) or in the inclined geometry with the counter electrode at a distance controlled by spacers as shown in Fig. 4.2B. Transparent, conducting, pre-cleaned ITO coated glass slides were used as substrates on which the soft cross-linked PDMS films were spin coated. The counter electrode was in the form of a flexible cover glass (18 mm $\times$ 18 mm, thickness $\approx$ 160 μm) or a rigid plate resting on a spacer (controlling the electrode-film distances, 0.03 μm $< d <$ 100 μm) made of a photoresist. The flexible contactor had a semi-transparent gold coating of thickness $\approx$ 50 nm on its top surface. A high voltage supply with controllable ramp-rate ($<$ 0.3 s) was used to apply the voltage between the two electrodes. The patterns were observed under a microscope and the images were captured using a digital camera. The additional voltage drop across the gold coated glass cover slip was accounted for in the calculations of the applied electric field. The total potential applied is the sum of the potential across the elastomeric film and that of the coverslip. Hence, the effective voltage is given by,

$$V_{app} = \phi_{pdms} + \phi_{glass} \tag{4.18}$$

$$\phi_{pdms} = \frac{V_{app}}{1 + (\epsilon_{pdms}/\epsilon_{glass}) * (h_{glass}/h_{pdms})} \tag{4.19}$$

4.5 Electric-field Induced Patterns

In the parallel geometry (Fig. 4.2A), the film surface is undeformed, while in the inclined geometry, a meniscus instability was present at the zone of

contact, prior to the application of electric field. The application of an external electric field causes the surface to deform whose response depends on the moduli of the films and on the geometry of the top contactor (parallel or inclined), and is totally different in each case.

4.5.1 Parallel Geometry

The application of an electric field normal to a surface causes a rippling of the initially flat surface [181]. Capillary waves of a well-defined wavelength grow with time. In the confinement of a plate capacitor, this leads to cylindrical bridges spanning the two capacitor plates with a lateral periodicity that is given by the wavelength, λ of the initially amplified wave spectrum [173]. Since the pattern selection is dominated by the initial phase of the instability, λ is quantitatively described by a linear stability analysis [182].

(a) Viscous Liquid

For all visco-elastic films with a cross-linker (CL) concentration of 1% or less, an array of circular columns packed locally in a hexagonal order appeared on the surface of film regardless of the voltage applied (Fig. 4.3). Their spacing remained constant from the earliest time an order could be detected on the film surface ($\sim$ 100 ms) [183]. Further increase in voltage led to the merger of the pillars and a complete intimate contact with the top contactor formed with time.

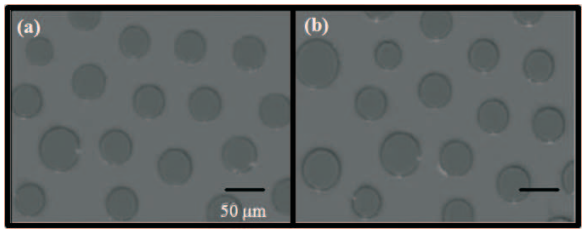

Figure 4.3: *Hexagonally ordered pillars for 0.5% CL concentration. (a) $h = 3\ \mu m$, $d = 2.5\ \mu m$ and $\phi = 60$ Volts and (b) $h = 6.8\ \mu m$, $d = 10\ \mu m$ and $\phi = 120$ Volts.*

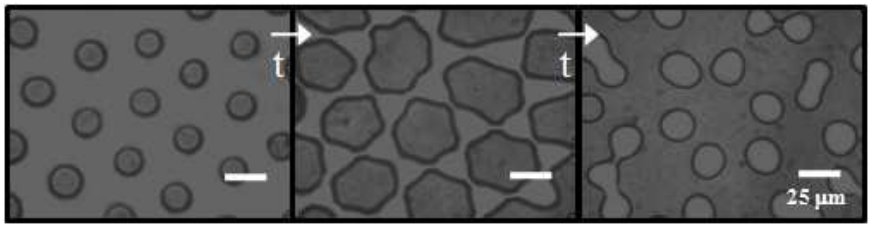

Figure 4.4: *The growth of the hexagonally ordered pillars into isolated voids for 1.5% CL concentration, $h = 3\ \mu m$, $d = 2.5\ \mu m$ and $\phi = 60$ Volts at time, $t \approx 0$ s, $t \approx 5$ s, $t \approx 65$ s.*

(b) Visco-elastic Liquid

The cross-over from the viscous liquid-like behavior to elastic solid-like behavior is continuous, although confined to a narrow range of elastic modulus ($1\% < \text{CL} < 2\%$). Pillars formed initially coalesce rapidly, thus altering the pattern dimensions, density and geometry as shown in Fig. 4.4 for a transition regime visco-elastic film at 1.5% CL. Eventually, the pillar structure (polymer-in-air) is transformed into a pattern of voids surrounded by the polymer (last picture in Fig. 4.4). The kinetics of pillar formation and their coalescence could be hastened by increasing voltage and decreasing viscosity. Upon removal of the electric field, pillar patterns disappeared, but the inverted void-patterns remained robust because of their greater area of adhesion.

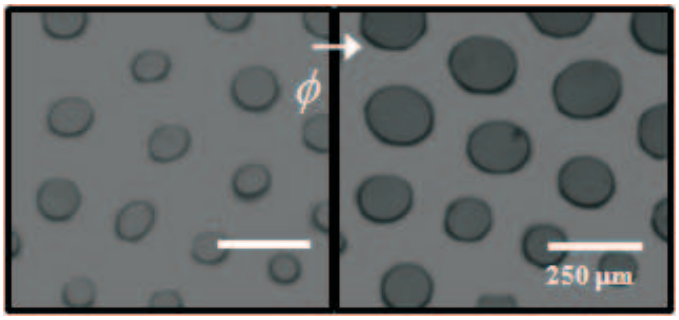

Figure 4.5: *Pillar size growth for 3.5% CL concentration (h = 75.2 μm and d = 50 μm) for external voltage V = 630 V ($\approx V_c$) and when V = 850 V (right side) with a slew rate < 0.3 s.*

(c) Elastic Solid

However, if the CL concentration was increased beyond 2%, the onset of instability now required a minimum critical voltage. The resulting pattern in these soft solid-like films was indistinguishable from the case of liquid-like films with identical morphology of circular pillars packed in a hexagonal lattice (Fig. 4.5).

4.5.2 Inclined Geometry

For all CL values > 3.5%, no pillars were observed even under high electric field. Air breakdown occurs at such high electric fields. In order to further study the effects of electric field, an inclined plane geometry was adopted. This inclined plane geometry produced a fingering instability at the zone of contact (Fig. 4.6), which was determined by the van der Waals interaction. The wavelength of these patterns were found to be $\sim 3h$. The application of electric field beyond a critical value induced changes in the fingering patterns already present. The electric field effects were broadly classified into three

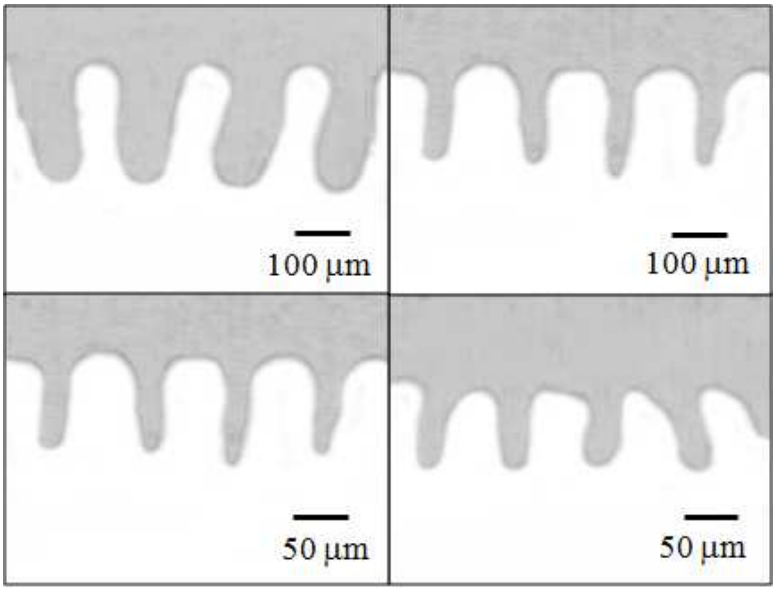

Figure 4.6: *The finger patterns observed prior to the application of the external electric fields for different thickness and shear modulus: clockwise h = 37.2 μm and μ = 3.9 MPa, h = 43.3 μm and μ = 6.9 MPa, h = 29.9 μm and μ = 2.2 MPa, and h = 24.1 μm and μ = 3.0 MPa, respectively.*

different categories: "Pillar Formation", 'Labyrinth Formation" and "Edge Straightening" [179, 184].

(a) Pillar Formation

In case of films with low stiffness parameter (1 MPa $< \mu <$ 4 MPa and 10 μm $< h <$ 100 μm), additional features besides the finger pattern appear in response to electric field beyond a critical value. At low electric fields, the change in the morphology of the initial fingers is not appreciable. However, beyond a critical voltage (ϕ_c), a row of circular pillars emerged ahead of the fingers. Interestingly, the spacing of the pillars is proportional to the wavelength of the adjacent finger-pattern. The first row of pillars form an out-of registry stack with respect to the finger pattern. On further increase

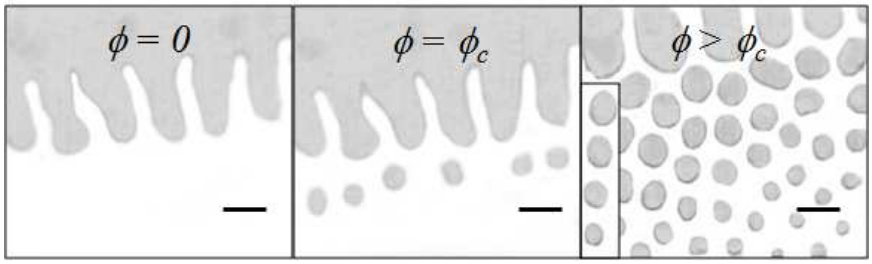

Figure 4.7: *Evolution of the pillars upon application of voltage for film parameters, h = 43.17 μm and μ = 2.17 MPa. Inset shows the decrease in diameter of the pillars as a function of distance away from the line of contact.*

in the voltage, additional rows of pillars appeared, accompanied by gradual increase in the diameter of the existing pillars as depicted in Fig. 4.7. The pillars become increasingly sparse and of decreasing diameter at increasing distance from the original fingers. The inhomogeneity in the electric field due to the inclined plane geometry is the resason for the decrease in the diameter of the pillars away from the fingering pattern. Thse distributed circular pillars appear in a 2-D hexagonal-type arrangement with spacing similar to the wavelength of fingers. The original finger-pattern remains unperturbed by the formation of subsequent pillars. The pillar-pattern also corresponds to a deep metastable state, in the sense that the pillar-formation is an irreversible process.

(b) Labyrinth Formation

The response to electric field for films of intermediate stiffness parameter (4 MPa $< \mu <$ 6 MPa and 10 μm $< h <$ 100 μm) is considerably different. Beyond the critical voltage (ϕ_c), the changes in the ampliltude of the finger patterns are abrupt. The amplitude of the finger-pattern rapidly increased by an order of magnitude (for example from 0.2 to 2 mm) with the wavelength

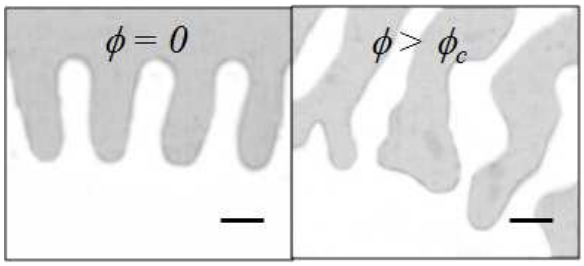

Figure 4.8: *The elongation of the finger pattern leading to the formation of labyrinth patterns for intermediate stiffness parameter films (h = 37.2 μm and μ = 3.9 MPa).*

remaining same for small increases in amplitude. These patterns continued to evolve beyond ϕ_c, the tips of the growing and expanding finger patterns ultimately undergo multiple scissions leading to the formation of patterns with a network of interpenetrating fingers. It was observed that this elongation process is irreversible, i.e., upon switching off the voltage the patterns remain trapped in the local metastable state and no not relax back to the original configuration. Thus, the change in the distance of the contact line and finger pattern is minimal.

(c) Edge Straightening

The response of high stiffness parameter films ($\mu > 6$ MPa and $10\mu\text{m} < h < 100\ \mu\text{m}$) when an exteral electric field is superimposed on it is that of "edge-straightening" where the amplitude of the patterns decreased appreciably above a certain field. Even though there is a change in the amplitude of the instability, there is no discernable change in the wavelength of these fingering instabilities. It was observed that the straightening of the finger-pattern occurs asymmetrically, with the amplitude of the finger decreasing with respect

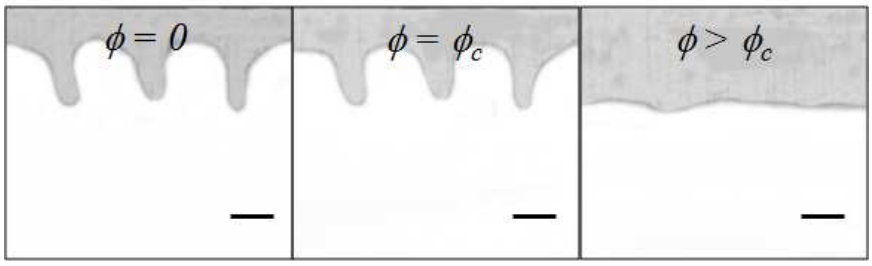

Figure 4.9: *The edge straightening of the finger patterns for film parameters, h = 76.8 μm and μ = 6.9 MPa.*

to a stationary tip. The decrease in amplitude was gradual and the eventual straightening appears in the form of a linear edge around a critical voltage (ϕ_c). Further increase in the voltage resulted in a gradual displacement of this linear edge towards regions of lower electrostatic energy and an effective increase in the contact area. The distance of the fingering pattern from the contact line increased indicating a more intimate contact between the film and the top glass substrate. The "edge-straightening" behaviour was observed to be reversible as the initial small-amplitude fingers reappear on switching-off the electric field, but the recovery time is much longer ($\sim$ 30 min.) because of greatly decreased elastic restoring force as compared to the electric force.

4.6 Discussion

4.6.1 Parallel Geometry

A general visco-elastic film subjected to an external destabilizing field displays two clearly distinct regimes of instability which have wavelengths corresponding to a purely viscous liquid and a purely elastic solid, regardless of

their detailed rheology with a continuous transition between the two regimes. Wavelength in the liquid regime depends on the applied field, film thickness and surface tension in a nonlinear fashion, whereas the wavelength in the solid elastic regime depends linearly on the film thickness independent of the field strength and material properties

(a) Viscous Liquid

The master curve for a purely viscous liquid is shown in Fig. 4.10. This observation is as seen from electrohyrodynamic theory [173], where λ is determined solely by a competition between the destabilizing force and the surface tension, but not by the factors that influence the kinetics, such as high frequency elasticity and viscosity, both of which vary greatly in the CL range of 0-1 %, $\lambda = C[VE^{-3}]^{1/2}$ where, $C = 2\pi[2\gamma/\epsilon_p\epsilon_0(\epsilon_p - 1)^2]^{1/2}$ and $E = V/[(d+h)\epsilon_p - h(\epsilon_p - 1)]$. However, the dynamics of full pillar formation was seen to depend on the CL concentration or visco-elasticity.

(b) Elastic

In the region where γ vanishes, for CL $> 2\%$, the strain energy density depends on the shear modulus (μ) of the film: $W(E)$=1/2($\mu\varepsilon$):E [179]. The elastic energy increases if there is a deformation of the film and hence acts as a stabilizing factor in this system. The total potential energy (for a given voltage ϕ) is a functional of the displacement field and is

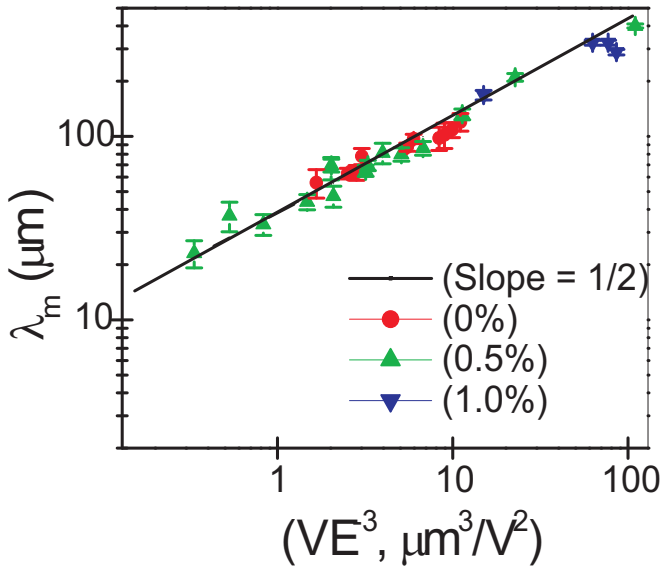

Figure 4.10: *Wavelength, λ vs VE^{-3} in log-log scale for viscoelastic liquid-like films for 0% < CL < 1%, 2.5 μm < h < 75 μm, and d = 30 nm, 2.5 μm, 4 μm, 20 μm , 40 μm, under bias conditions of 5 V < V < 150 V. The line represents the viscous film theory (γ = 19.8 mN/m and ϵ_p = 2.65).*

$$\Pi(u) = \Pi_{ES}(u) + \Pi_{EL}(u) = \int_V dV W(E) - \frac{1}{2}\int_A dxdy \frac{\epsilon_0 \epsilon_p \phi^2}{\epsilon_p d + h - (\epsilon_0 - 1)u(x,y)} \tag{4.20}$$

This energy functional was used to determine the critical voltage required to induce morphological changes. To obtain an analytical expression for the critical voltage, it was assumed that the variation of deformation along the x-direction is much larger than in the y-direction and, hence, the variation along the y-direction is neglected. Within this framework, a linear stability analysis of Eqn. 4.20 was performed. To this end, for a given gap thickness d and voltage ϕ, the homogeneous state of the film comprises $u = 0$, with an additional uniform pressure field p_0 in the film, given by

$$P_0 = \frac{(\epsilon_p - 1)\epsilon_0 \epsilon_p \phi^2}{(\epsilon_p d + h)^2} \tag{4.21}$$

The pressure p_0 in Eqn. 4.21 is obtained by calculating the force per unit area of the film surface exerted by the electric field. For a given d, if ϕ is large enough, this homogeneous state may be unstable to pattern formation. To investigate this, it was assumed that the film surface undergoes a perturbing deformation of the form $u(x)=\alpha_k \cos(kx)$, where k is the wavevector of the perturbation and α_k is its amplitude. In a linear stability analysis, this term was used in Eqn. 4.20 and a condition such that the energy expression up to quadratic order in α_k is negative was obtained. The average electrostatic energy $\langle \Pi_{ES} \rangle$ per unit area of the film is evaluated as

$$\langle \Pi_{ES} \rangle = -\frac{1}{2} \frac{(\epsilon_p - 1)^2 \epsilon_0 \epsilon_p \phi^2}{(\epsilon_p d + h)^2} \tag{4.22}$$

The average elastic energy per unit area for such a deformation field in an incompressible film is [185]:

$$\langle \Pi_{EL} \rangle = \frac{1}{2} \frac{\mu}{h} S(hk) \alpha_k^2 \tag{4.23}$$

where $S(\zeta)$ is the universal function

$$S(\zeta) = \frac{2\zeta(1 + \cosh(2\zeta) + 2\zeta^2)}{\sinh(2\zeta) - 2\zeta} \tag{4.24}$$

The term $\mu S(hk)$ can be interpreted as a wavelength (wavenumber) dependent effective elastic stiffness. The mean total energy per unit film area of the perturbation $u(x)$ is

$$\langle \Pi \rangle = \langle \Pi_{ES} \rangle + \langle \Pi_{EL} \rangle = \frac{1}{2}(\frac{\mu}{h} S(hk) - \frac{(\epsilon_p - 1)^2 \epsilon_0 \epsilon_p \phi^2}{(\epsilon_p d + h)^2})\alpha_k^2 \tag{4.25}$$

If the term in the brackets becomes negative, the perturbation Eqn. 4.22 becomes unstable. The critical value of ϕ that induces instability is the smallest value of ϕ at which some mode (described by a wavenumber k) becomes unstable.

From the definition of S, it is evident that a perturbation wavelength is very small compared with the thickness $hk >> 1$ ($S(\zeta) \rightarrow \infty$, for $\zeta \rightarrow \infty$), and one with wavelength much larger than the film thickness $hk << 1$ ($S(\zeta) \rightarrow \infty$, for $\zeta \rightarrow 0$); both cost large energy penalties. The lowest effective elastic stiffness occurs at an intermediate value of the wavelength corresponding to $hk_c = 2.12$ for which $S(hk_c) = 6.22$. Thus, when the voltage ϕ exceeds a value ϕ_c, the perturbation with wavenumber equal to k_c or equivalently wavelength $\lambda_c \approx 3h$ becomes unstable, where ϕ_c is given by

$$\phi_c^2 = \frac{6.2\mu}{h} \frac{(\epsilon_p d + h)^3}{(\epsilon_p - 2)^2 \epsilon_p \epsilon_0} \tag{4.26}$$

It was indeed observed that the onset of instability in solid films required a critical voltage and pillars were not formed when ϕ was maintained marginally lower than ϕ_c even for several hours. The pillars formed at $\phi > \phi_c$ could extend and contact the flexible-thin contactor for the entire range of experiments where d varied from 2.5 μm to 90 μm. The trend of the ϕ_c values predicted by Eqn. 4.26 with respect to h is observed qualitatively in our measurements shown in Fig. 4.11. When d is small compared to h, ϕ_c

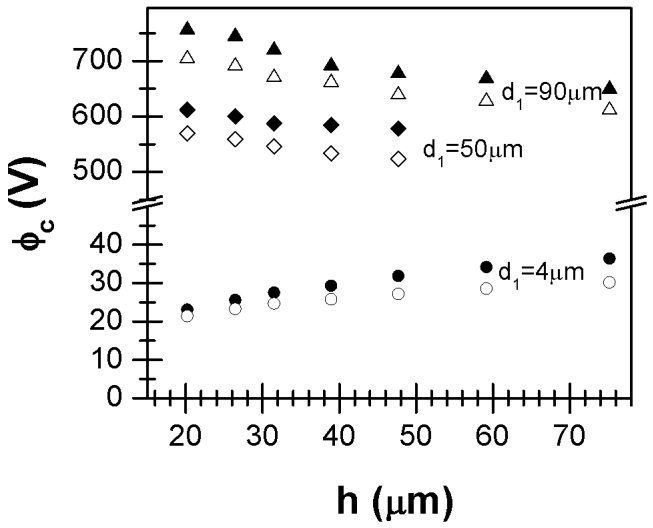

Figure 4.11: *Dependence of critical voltage, ϕ_c on film thickness, h for different values of air gap, d. The hollow and solid symbols represent CL concentrations of 3% and 3.5% respectively.*

increases with h. However, for large values of d, the ϕ_c scales inversely with h. Notwithstanding these qualitative trends, Eqn. 4.26, with $\mu = 0.1$ MPa, quantitatively predicts voltages that are several times larger than the experimental values and are in fact large enough to cause a dielectric breakdown of the polymer and air! In the experiments, elastic pillar formation was observed only when either a flexible top electrode was used where a small bending (~ 2 μm at 500 V; much smaller than the air gap) of the electrode at its center was observed or slightly non-parallel rigid electrode was used. This small bending of the electrode and the lateral field gradient thus created is an essential factor in kick-starting the elastic instability which is a nucleation phenomena at much lower voltages. Interestingly, the wavelength in this regime becomes independent of the applied critical voltage, as well as

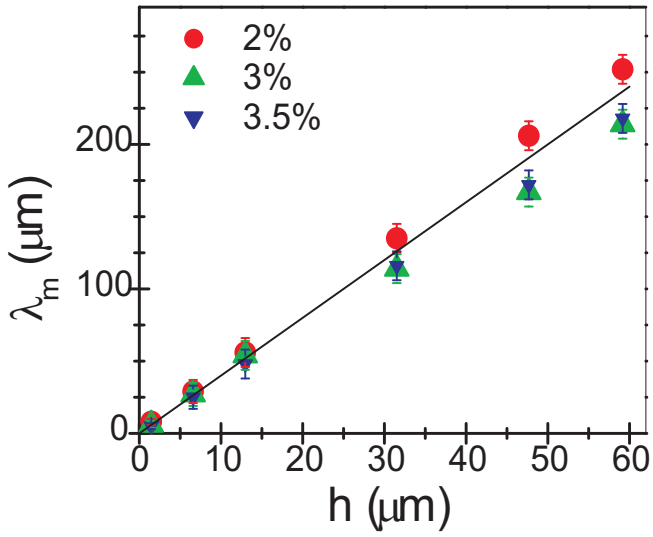

Figure 4.12: *λ formed in solid-like viscoelastic films for different CL concentrations, the line represents the best fit with slope = 4.1.*

the CL concentration or precise level of solid visco-elasticity. For these solid-like films, the wavelength exhibits a linear relationship with the film thickness with a best fit of $\lambda \sim 4h$ (Fig. 4.12). This is reminiscent of the elastic contact instability seen in debonding and peeling of elastic adhesives [170–172].

(c) Visco-elastic

The cross-over from the viscous liquid-like behavior to elastic solid-like behavior is continuous. This is unlike the discontinuous first order transition found in a study of debonding of visco-elastic layers [186]. The above observations were understood from a more general linear stability analysis.

In visco-elastic films, there exists viscous stresses σ^v in addition to equilibrium elastic stresses, given by $\sigma^v = 2\mu\left(\frac{1}{2}\nabla u + \nabla u^T + \frac{\nu}{1-2\nu}\nabla \cdot uI\right) 2\eta[\frac{1}{2}(\nabla \dot{u} + \nabla \dot{u}^T) - \frac{1}{3}\nabla \cdot \dot{u}I]$, where $\dot{()}$ stands for the time derivative, η is the viscosity parameter, and I is the unit tensor.

The homogeneous solution is unstable to periodic deformation of the form $u_j \sim e^{(ikx_1)}u(j)e^{\omega t}$. The solution for ω indicates that there is a mode with wavenumber (k_m) such that the rate of growth (ω) is maximum. An analytical result was derived for (k_m) such that,

$$hk_m = hk_c + \left[0.39\frac{\gamma}{\mu h} - 0.46(1-2\nu)\right]\frac{h}{\mu}(Y - Y_c) \tag{4.27}$$

The following dispersion relation for a visco-elastic thin film with constant viscous and elastic moduli was obtained [177]:

$$(\eta\omega/\mu) = \left[-(\gamma/h\mu)q^2 + (h/\mu)S\right](2qY(q))^{-1} - 1 \tag{4.28}$$

where, $q = k_m h$, $Y(q) = ((1+e^{2q})^2 + 4e^{2q}q^2)(-1 + e^{4q} - 4e^{2q}q)^{-1}$ and $S = (\partial\pi/\partial h) = \epsilon_0\epsilon_p V^2(1-\epsilon_p)^2(d\epsilon_p + h)^{-3}$ where ω is the growth coefficient of instability, k_m is its wave number, γ is surface tension, μ is elastic shear modulus, η is viscosity, d is air gap, h is film thickness, π is excess electric pressure at the interface, ϵ_0 is dielectric permittivity of the free space, ϵ_p is dielectric constant of the polymer (= 2.65) and V is applied voltage. From the above relation, the liquid-like scaling is obtained when the parameter $(\gamma/h\mu)$ is large, whereas the solid-like scaling $\lambda \sim 3h$ is recovered for small $(\gamma/h\mu)$. While, in the visco-elastic case, the scaling of wavelength with the film thickness, $\lambda = nh$, with $n > 4$, is also found intermediate to the liquid-like and the solid-like films as predicted by Eqn. 4.28 (Fig. 4.13).

Fig. 4.14 shows the wavelength obtained from Eqn. 4.28 which adequately describes the features of transition from the liquid-like behavior at low ($<\sim$ 10 Pa) elastic modulus to elastic solid-like behavior at moderately high values

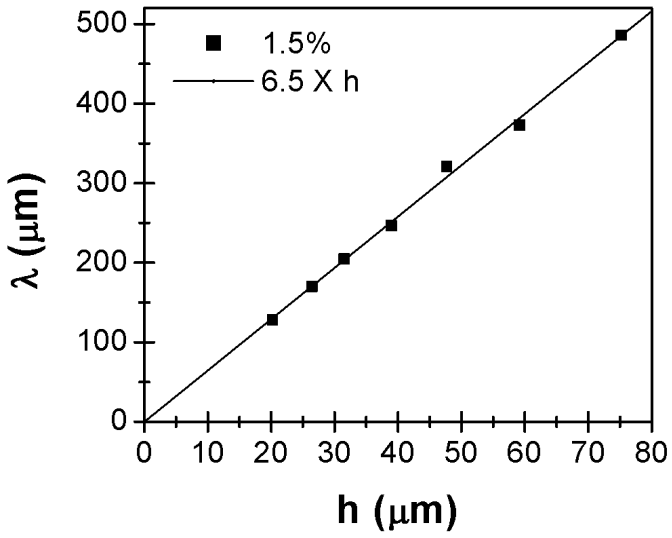

Figure 4.13: *λ formed in viscoelastic films for 1.5% CL concentration, the line represents the best fit with slope = 6.4.*

($>\sim$ 1000 Pa). Interestingly, the wavelength in all cases is independent of viscosity as predicted by Eqn. 4.28. Further, in both the liquid-like and the solid-like regimes, it also becomes independent of the elastic modulus, which remains important only in the transition regime. Basically, in the liquid-like regime, surface tension is the dominant stabilizing mechanism, whereas in the solid-like regime, the elastic strain dominates. The transition is thus governed both by surface tension and elasticity in the form of the parameter, $(\gamma/h\mu)$. Further, in the solid-like regime, λ is solely governed by the pattern that minimizes the elastic energy penalty [170–172, 177, 187] and the film viscosity merely governs the dynamics of pattern formation [177].

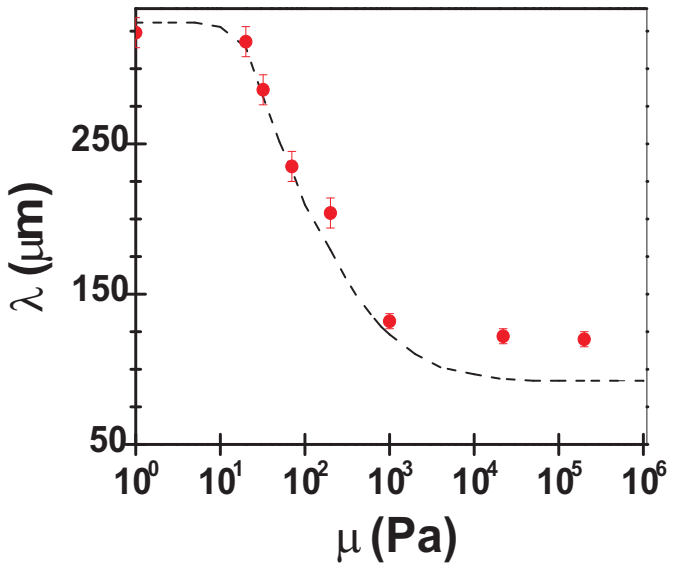

Figure 4.14: *Transition between the liquid-like and the solid-like regimes with predictions of Eqn. 4.28 for $h = 31.5$ μm, $d = 50$ μm; $V = 30$ V for liquid-like films and V_c for solid-like films.*

4.6.2 Inclined Geometry

The instability induced by the electric potential, when it exceeds a critical value occurs at the same wavelength ($\lambda \sim 3h$) as that induced by the van der Waals forces (meniscus instability). Thus, morphological changes induced by the electric field have similar spacing to that of the other adhesive interactions, including the van der Waals interaction. This observation is also in line with the linear stability analysis [170, 171, 177, 185], which predicts the length scale of the elastic contact instability to be independent of the decay behavior of the adhesive force.

Because of the crack-like geometry in our experimental setup, it is evident that $\epsilon_p d + h \approx h$ (because $d \sim$ 10-50 nm, $h \sim 10$ μm, $\epsilon_p = 2.65$), and thus [179] from the previous expression (Eqn. 4.26),

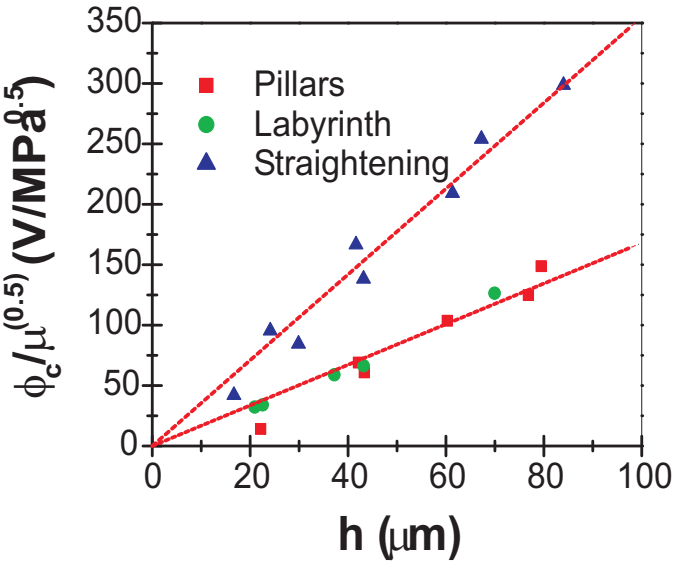

Figure 4.15: *Plot of experimentally obtained $\phi_c/\sqrt{\mu}$ as a function of h from measurements of films of different h and μ values.*

$$\phi_c = \left(\frac{6.22}{(\epsilon_p - 1)^2 \epsilon_0 \epsilon_p}\right) h\sqrt{\mu} \tag{4.29}$$

The critical voltage necessary to induce morphological changes increases linearly with the thickness h of the film, and has a weaker dependence on the shear modulus of the film as $\sqrt{\mu}$. Fig. 4.15 shows the linear dependence of $\phi_c/\sqrt{\mu}$ as a function of film thickness, h. Interestingly, the case of pillar formation has a different slope, $(d(\phi_c/\sqrt{\mu})/dh)$ compared to the cases corresponding to the edge straightening and finger elongation (Fig. 4.15). This difference is due to the geometry of the initial fingers. Even though their functional dependence on the film parameters such as film thickness and shear modulus is not modified, the energy magnitude changes.

(a) Morphology Evolution

While the electrostatic energy promotes the increase of the contact area between the film and the contactor, the resulting morphology depends on two forces, both of which act to oppose morphological changes the elastic restoring forces in the film and the bending energy of the contactor.

The final morphological structure depends on which of the two opposing forces are stronger. If the elastic stiffness parameter of the film and, consequently, the elastic energy penalty in the film are smaller than the energy penalty of the contactor bending, then the increase of contact area should occur by the deformation of the film surface, keeping the curved contactor in essentially the same configuration as before the application of the electric field. In the experiments, this scenario was seen in the case of the pillar-formation regime for relatively small values of film stiffness. In this case, the initial areas of contact complete with the fingers are preserved, while pillars emerge ahead of the fingers. It is therefore evident that the contactor undergoes very little additional deformation in this case by the application of electric field. As seen from the morphological phase diagram, it was noted that the regime of small μ/h indeed produces pillar-like morphology when subjected to an external electric field.

On the other hand, in very stiff films (with large μ/h ratios), the contact area can be increased by deforming the contactor, rather than the film, so as to effectively move the contact line toward the spacer; i.e., the average y-coordinate of the contact line increases (Fig. 4.2). Again, the regions of large μ/h do correspond to the edge straightening. For the intermediate values

of the stiffness parameter μ/h, which is larger in the pillar-formation regime but smaller than the edge straightening regime, the contactor bending energy penalty is comparable with the elastic energy penalty of the film. Thus, the contactor bends together with elongation of finger patterns, giving rise to labyrinth patterns, to gain the electrostatic energy.

(b) Hysteresis

This irreversibility refers to the lack of recovery of the original finger patterns upon switching off the applied voltage. This phenomenon is due to the short-range van der Waals and other contact adhesive forces. The inclusion of short-range adhesive forces, after the formation of contact zones, generates metastable local minima in the energy landscape, which pins an already formed structure. Thus, after the formation of intimate contact zones, the structures already formed by the electric field can persist whenever the adhesive interactions are sufficient to maintain adhesion. Metastablity of adhesive zones, notwithstanding their higher energy, is also known to be responsible for the observed persistence of patterns in peeling and debonding experiments. The patterns once formed at elastic contact continue to adhere and elongate over much larger gap distances during the withdrawal or pulloff of the contactor [178]. The morphological patterns are thus trapped in a metastable local minimum of the energy, even though the global minimum of the energy after switching off the electric field is a flat film.

The driving force for the recovery and relaxation of the patterns after removal of the electric field or the contactor is the stored elastic energy of the film. In the case of films with a small stiffness parameter that show pillar

formation, these elastic forces are weak and are unable to move over the energy barrier that produces metastability. When the film stiffness parameter is large (resulting in edge-straightening effects upon the application of the electric field), the elastic forces are strong enough to drive the system back to its original configuration of finger patterns. In the intermediate case, the elastic forces provide for a partial recovery, but the system may get trapped in a metastable local energy minimum configuration intermediate to the original configuration and the one induced by the electric field.

4.7 Conclusions

The effects of visco-elasticity and an external electric field on thin polymeric films have been studied, both in parallel geometry and in inclined geometry. In parallel geometry, a visco-elastic film subjected to an external destabilizing field displays two clearly distinct regimes of instability which have wavelengths corresponding to a purely viscous liquid and a purely elastic solid, regardless of their detailed rheology. The transition between the two regimes of long and short waves is confined to a narrow zone of a parameter, $(\gamma/\mu h)$. Wavelength in the liquid-like regime depends on the applied field, film thickness and surface tension in a nonlinear fashion, whereas the wavelength in the solid-like elastic regime depends linearly on the film thickness independent of the field strength and material properties. However, the kinetics of instability is influenced by rheology. An important difference between a liquid-like film and a solid-like film is the presence of a critical voltage required to engender the pillar formation in the latter case.

In inclined geometry, a critical voltage was required to engender morphology change. It was found that three distinct types of electric-field-induced pattern morphologies were possible depending on the stiffness and thickness of the films. These include edge straightening (which reduces the dimensionality of the patterns), labyrinth formation (which maintains the dimensionality of the pattern), and pillar formation (which converts a 1D pattern into a 2D pattern). These patterns were explained by the physics of electric field induced contact instabilities. The irreversibility of these patterns formed upon application of an external electric field was attributed to the local energy minimums present in the energy landscape.

Chapter 5

Summary

The optical activity, photoelectric signals and the effect of local electrostatic environment on the photophysical activity of a protein - retinal complex, Bacteriorhodopsin was investigated in the first half of the thesis. The response of soft polymeric films to an applied electric field leading to a surface deformation was investigated in the latter part of the thesis.

The functionality of protein in film form was further investigated by measuring photoelectric signals from it. Upon photoexcitation of bR, the electrical signals were measured across the polymer layer with two lateral electrodes. In essence, the changes in the polymer layer was temporary or prolonged depending on the polymer layer used. The polymer layer can act as an antenna to pick up charge fluctuations from the adjacent bR layer. The thickness of the bR films were reduced from multilayers to monolayers and photoelectric signals from these layers were observed. This concept of passive and active biomolecular signal transduction can possibly be used to probe the internal processes of the biomolecules and also utilized for various sensing activities.

The optical activity of monolayers of bR was characterized using a transmission mode scanning near-field optical microscopy. Optical constants such as the molar absorptivity, quantum efficiency for photoconversion were obtained from these measurements. The molar absorptivity values were higher than those observed from the absorption spectroscopy measurements due to the fact that all the molecules present within the beam area are oriented and also due to the additional interaction of the near-field tip to the retinal chromophore, that has its transition dipole moment oriented at an angle with the membrane normal. The transmission signals from pump induced near-field scans were used to study and control the dynamics of the population in respective intermediate states. Further, the local electrostatic environment of bR was modified by modifying the underlying substrate to see its effects on the quantum efficiency of photoconversion. The transmission SNOM based technique used in this thesis, can be used for studying the structure-property relationships of various other non-flourescent proteins.

Soft polymeric films deform upon the application of an electric field to give rise to hexagonally ordered pillars. The wavelength of these periodic pillars in the liquid-like case depended on the applied voltage and the surface tension, which acted as the stabilizing force, whereas in the solid-like case, the wavelength of these periodic patterns was independent of the applied voltage, as long as it exceeded a critical value. Further, in inclined-plane geometry, the application of electric field modified the pre-existing morphological patterns. The morphology of final patterns depended on the elastic shear modulus of the films.

The understanding of the various parameters that govern the deformation

of thin films upon application of the electric field was used to deform a liquid alloy. Upon application of an electric field, the alloy droplet deformed and could make contact with the top electrode. The extent of movement, could be controlled by the electric field applied. This concept was used to make contacts to bR based devices, where the liquid alloy was used as the top contact instead of the aluminium electrode. Photoelectric signals were observed, when the alloy made contact with the bR based device [188]. These results highlight the possibility of using this alloy as an alternative to other conventional contacts for molecular devices.

Near-field microsocpy is a powerful tool to study the structure and function (optical activity) of various molecules in their native environment. These measurements (flourescence or transmission) can be used to study the activity on a single molecule level. The photoelectrical activity of various biomolecules can be studied and a clear correlation can be established between molecular events and electrical measurements beyond just observing the ensemble averaged electrical signatures. The conducting polymer network can be used as an underlying layer upon which various biomolecules (proteins, neural networks and various cells) can be oriented and their electrical signatures studied in an non-invasive manner.

Appendix A

The electric field surrounding from the near-field probe was simulated using the software, OPTIFDTD 8.0, from Optiwave. This software uses the finite difference time domain (FDTD) method to calculate the propagation of the electromagnetic wave. This approach is based on a direct numerical solution of the time-dependent Maxwell's curl equation. The software uses central difference approximations for the numerical derivaties in space and time, both having second-order accuracy.

The layout of the near-field probe is shown in Fig. A.1. The values used for the near field probe is as follows: the probe consisting of the core (n = 1.45) and cladding (n=1.6) of a coaxial bragg fiber, with an outer coating of Aluminium (thickness = 250 nm), whose refractive index was assumed using the Lorentz-Drude model. The tapering angle used was $\sim$ 14, which is the standard taper angle used in the near-field probes.

The simulation parameters are as follows. A transverse magnetic (TM) plane wave (λ = 532 nm) was used as the source, which was propagating along the z-direction. The mesh sizes were 100 nm both along x-axis and and along y-axis. The time step was 0.2 fs and the running time of the simulation was for 3000 steps.

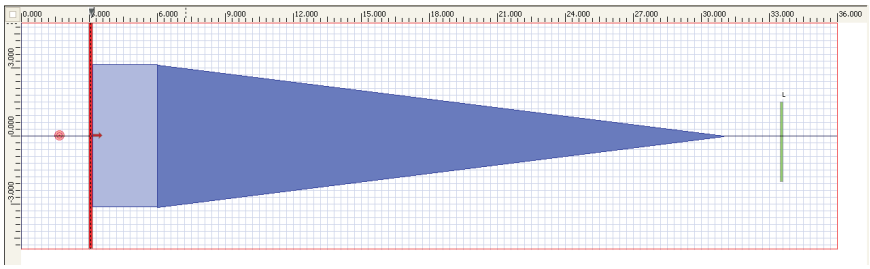

Figure A.1: *The schematic layout of the near-field probe used for simulation.*

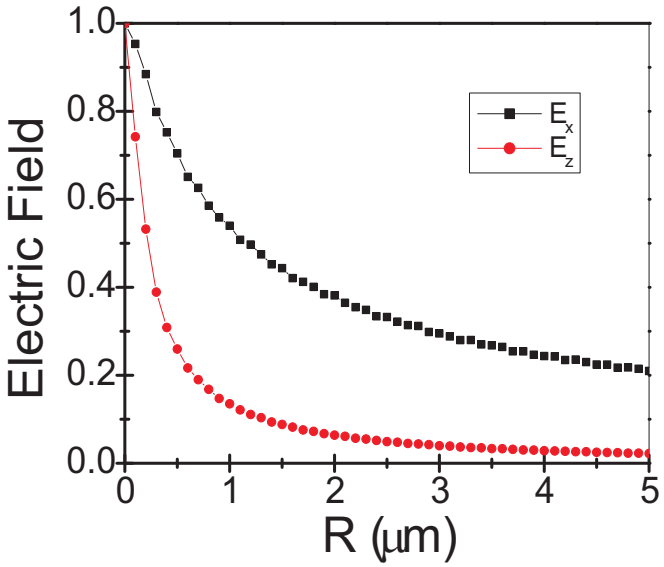

Figure A.2: *Longitudinal E_z and Transverse E_x component of the field as a function of distance from the tip.*

The output of this simulation consists of both E_x and E_z. The E_z profile is the longitudinal component of the field while E_x is the transverse component of the field. Fig. A.2 shows the exponential decay of E_z from the tip, whereas the E_x decay is due to the point source like nature of the tip.

The simulations carried out using this software replicate the earlier observed results.

Appendix B

To confirm that the transmission changes obtained is due to bR molecules, many control experiments were performed.

(a) Constant Gap and Constant Height Mode

In order to get an artifact free transmission image, Hecht et. al have suggested that first SNOM be done by constant gap mode to identify regions of interest and then SNOM be done in constant height mode. They have suggested that the constant height mode scans be carried out by retracting the tip by a small distance, usually > than the topographical feature and carrying out the raster scanning. In our case, the constant height mode scans were done by retracting the tip by $\sim$ 15 nm (greater than the monolayer height), and then raster scanning the sample. Figure B.1 shows the results of both constant gap mode and constant height mode. The change in transmitted intensities observed in Fig. B.1(C) and (D) are essentially similar, confirming that the observed changes are essentially due to absorption by the bR patch and not due to topological artifacts.

To prove that the additional decrease in SNOM transmission during pump experiments, ($\lambda = 405$ nm), is due to the changes to bR photocycle and not

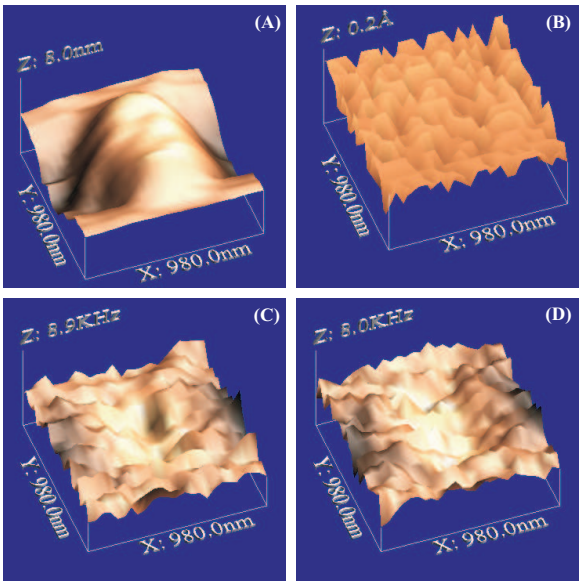

Figure B.1: *(A) and (B) The AFM image in constant gap mode and constant height mode. (C) and (D) Transmission SNOM image in constant gap mode and constant height mode. The scale is equalized in both the cases. Scan area 1 μm × 1 μm.*

due to tip heating caused by the pump laser, transmission SNOM experiments were performed with different pump λs.

(b) Transmission SNOM with pump λ = 570 nm

When λ = 570 nm was used as the pump and transmission SNOM experiments were carried out with probe λ = 532 nm, the transmission decreased from 99.1% to 99.4%, as seen in Fig. B.2. This is due to the fact that pumping bR monlecules with λ = 570 nm perturbs the photocycle by depleting the ground state (B-state), whose absorption is centered around 570 nm. Since, the no. of molecules in ground state is lower, this leads to a lower absorption and higher transmission when probed with λ = 532 nm as indeed seen in our experiments.

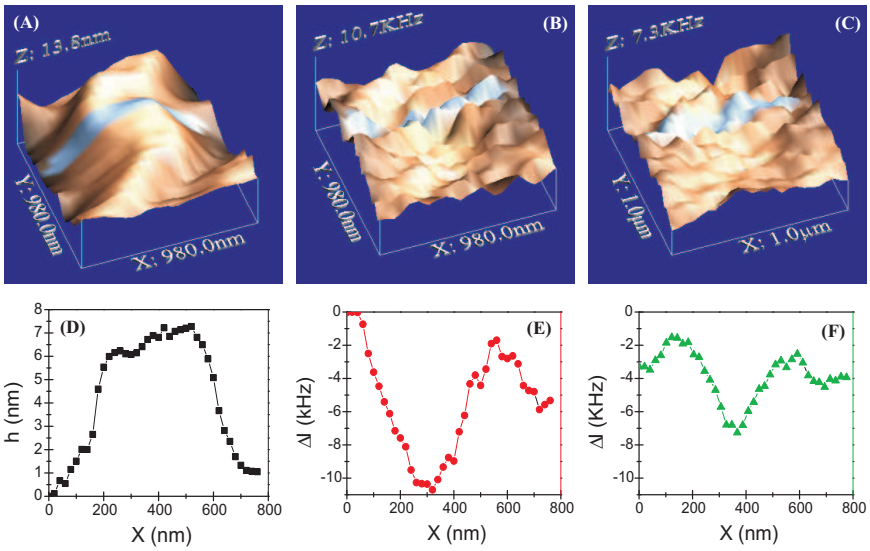

Figure B.2: *(A) The AFM image, (B) Transmission SNOM image and (C) Pump-Induced Transmission SNOM image of a bR patch with λ = 532 nm through the tip and the pump beam at λ_{max} = 570 nm. The scale is equalized for (B) and (C). Line profiles of the AFM, SNOM and PI-SNOM images in (C), (D) and (F). Scan area 1 μm × 1 μm.*

(b) Transmission SNOM with pump λ = 670 nm

When a pump λ = 670 nm is used, it does not modify the photocycle of bR. The no. of molecules present in B- and M- states remain the same. The presence of an additional pump can modify the tip sample interaction. But, as seen in Fig. B.3 both (C) and (D) are similar, showing that, the pump λ = 670 nm, neither causes change to the photocycle efficiencies nor does perturb the tip-sample interaction, leading us to conclude that an additional pump laser does not modify the tip-sample interaction.

The above control experiments in different modes (constant gap and height) and different pump λ, clearly show that the transmission changes measured were due to the bR molecules. The results from constant gap and constant height modes were similar, showing that the observed transmission

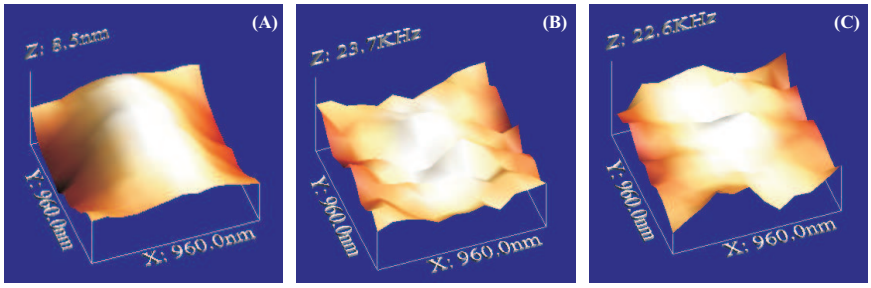

Figure B.3: *(A) The AFM image, (B) Transmission SNOM image and (C) Pump-Induced Transmission SNOM image of a monolayer of bR patch with λ = 532 nm through the tip and the pump beam at λ_{max} = 670 nm. The scale is equalized for (B) and (C). Scan area 1 μm × 1 μm.*

changes were due to the bR molecules. Further, experiments with different pumps show that the tip-sample interactions are not modified by the presence of additional pump and transmission changes arising in the respective cases were due to the pump induced changes to the bR photocycle.

Appendix C

The formatiion and subsequent evolution of the pillars upon applying an external voltage was observed using a CCD camera. The data was recorded in the form of a avi file, from which each and every frame was cut and was used for further analysis. A typical video file, which has been converted into frames is shown in Fig. C.1. Typically, for every experiment, such video files were recorded and image files were extracted from it.

The wavelength of the patterns was obtained by doing a fourier transform of the images obtained from the avi files. A representative FFT of the image is shown in Fig. C.2. The FFT shows spots similar to the diffraction patterns observed from a hexagonally ordered crystal, with the spacing between corresponding to the wavelength of the pillar patterns.

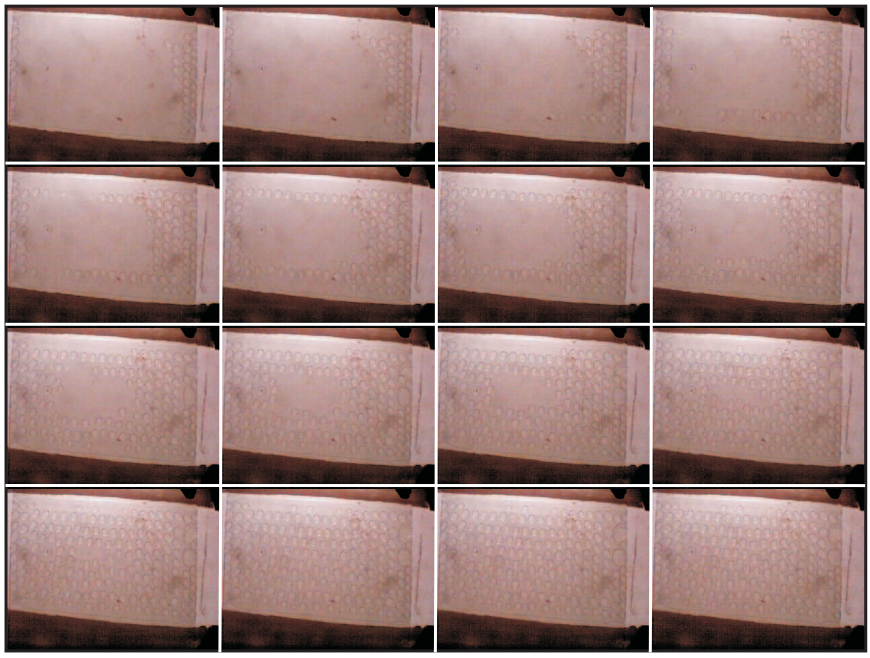

Figure C.1: *Frames selected from a video file showing the evolution of pillars. The images represent every 200^{th} frame. The frame rate of the CCD camera used was 30 fps.*

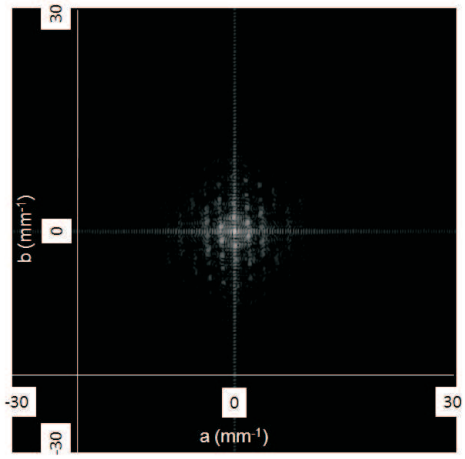

Figure C.2: *FFT image of a periodic pillar structure.*

Bibliography

[1] A. J. Heeger; Nobel Lecture: Semiconducting and metallic polymers: The fourth generatin of polymeric materials, *Rev. Mod. Phys.*, **2001**, *73*, 681–700.

[2] A. J. Heeger; Semiconducting and metallic polymers: The fourth generatin of polymeric materials (Noble Lecture), *Angew. Chemie. Int. Ed.*, **2001**, *40*, 2591–2611.

[3] W. P. Su; J. R. Schrieffer; A. J. Heeger; Solitons in polyacetylene, *Phys. Rev. Lett.*, **1979**, *42*, 1698–1701.

[4] W. P. Su; J. R. Schrieffer; A. J. Heeger; Soliton excitations in polyacetylene, *Phys. Rev. B*, **1980**, *22*, 2099–2111.

[5] W. P. Su; J. R. Schrieffer; Soliton dynamics in polyacetylene, *Proc. Natl. Acad. Sci. USA*, **1980**, *77*, 5626–5629.

[6] J-L. Bredas; R. R. Chance; R. Silbey; Theoretical studies of charged defect states in doped polyacetylene and polyparaphenylene, *Mol. Cryst. Liq. Cryst.*, **1981**, *77*, 319–332.

[7] A. J. Heeger; S. Kivelson; J. R. Schrieffer; W. P. Su; Solitons in conducting polymers, *Rev. Mod. Phys.*, **1988**, *60*, 781–850.

[8] K. Fesser; A. R. Bishop; D. K. Campbell; Optical absorption from polarons in a model of polyacetylene, *Phys. Rev. B*, **1983**, *27*, 4804–4825.

[9] J-P. Farges, *Organic Conductors: fundamentals and application;* Marcel Dekker, 1994.

[10] C. K. Chiang; S. C. Gau; R. Fincher Jr.; Y. W. Park; A. G. MacDiarmid; A. J. Heeger; Polyacetylene, (CH)$-x$: n-type and p-type doping and compensation, *Appl. Phys. Lett.*, **1978**, *33*, 18–20.

[11] H. Shirakawa; E. J. Louis; A. G. MacDiearmid; C. K. Chiang; A. J. Heeger; Synthesis of electrically conducting organic polymers: halogen derivatives of polyacetylene, (CH)$-x$, *J. Chem. Soc. Chem. Commun.*, **1977**, pages 578–580.

[12] C. K. Chiang; C. R. Fincher Jr.; Y. W. Park; A. J. Heeger; H. Shirakawa; E. J. Louis; S. C. Gau; A. G. MacDiarmid; Electrical conductivity in doped polyacetylene, *Phys. Rev. Lett.*, **1977**, *39*, 1098–1101.

[13] P. J. Nigrey; A. G. MacDiarmid; A. J. Heeger; Electrochemistry of polyacetylene, $(CH)_x$: electrochemical doping of (CH)$-x$ films to the metallic state, *J. Chem. Soc. Chem. Commun.*, **1979**, *93*, 594–595.

[14] C. Jones; P. M. Jordan; A. G. Chaudhry; M. Akhtar; Stereospecificity of hydrogen removal from the four methylene bridges in haem biosynthesis: specific incorporation of the 11 *pro*-S hydrogen of porphobilinogen into haem, *J. Chem. Soc. Chem. Commun.*, **1979**, pages 96–97.

[15] R. D. Bach; D. H. Lucast; Stereochemistry of concerted 1,2-vinyl migration to a developing carbenium-ion centre, *J. Chem. Soc. Chem. Commun.*, **1979**, pages 593–594.

[16] A. G. MacDiarmid; A. J. Epstein, *Conjugated polymeric materials: Opportunities in electronics, optical electronics, molecular electronics;* Kluwer Academic, Dordrecht, 1990.

[17] F. Wudl; R. O. Angus Jr.; F. L. Lu; P. M. Allemand; D. J. Vachon; M. Nowak; Z. X. Liu; H. Schaffer; A. J. Heeger; Poly-p-phenyleneamineimine: synthesis and comparison to polyaniline, *J. Am. Chem. Soc.*, **1987**, *109*, 3677–3684.

[18] A. G. Macdiarmid; J. C. Chiang; A. F. Richter; A. J. Epstein; Polyaniline: a new concept in conducting polymers, *Synth. Met.*, **1987**, *18*, 285–290.

[19] P. W. Anderson; Absence of diffusion in certain random lattices, *Phys. Rev.*, **1985**, *109*, 1492–1505.

[20] J. W. Blatchford; A. J. Epstein; Resource letter EPA-1: Electronic polymers and their applications, *Am. J. Phys.*, **1996**, *64*, 120–135.

[21] R. S. Kohlman; J. Joo; A. J. Epstein, *Physical properties of polymes handbook;* AIP Press.

[22] R. S. Kohlman; A. J. Epstein, *Handbook of Conjugated polymers;* Marcel Dekker, New York.

[23] D. Baeriswyl; D. K. Campbell; S. Mazumdar, *Conjugated conducting polymers;* Springer-Verlag, Berlin.

[24] E. M. Conwell; Transport in Trans-polyacetylene, *IEEE Transactions on Electrical Insulation*, **1987**, *EI-22*, 591–627.

[25] N. F. Mott; E. Davis, *Electronic processes in non-crystalline materials;* Clarendon Press, Oxford.

[26] P. Sheng; Fluctuation-induced tunneling conduction in disordered materials, *Phys. Rev. B*, **1980**, *21*, 2180–2195.

[27] J. L. Bredas; R. Silbey, *Conjugated Polymers;* Kluwer Academic Publishers, Dordrecht, 1991.

[28] Bayer AG; *European Patent*, **1988**, *03339340.*

[29] L. Groenendaal; F. Jonas; D. Freitag; H. Pielartzik; J. R. Reynolds; Poly(3,4-ethylenedioxythiophene) and its Derivatives: Past, present, and future, *Adv. Mater.*, **2000**, *12*, 481–494.

[30] F. Jonas; L. Schrader; Conductive modifications of polymers with polypyrroles and polythiophenes, *Synth. Met.*, **1991**, *41-43*, 831–836.

[31] G. Heywang; F. Jonas; Poly(alkylenedioxythiophene)s - new, very stable conducting polymers, *Adv. Mater*, **1992**, *4*, 116–118.

[32] I. Winter; C. Reese; J. Hormes; G. Heywang; F. Jonas; The thermal ageing of poly(3,4-ethylenedioxythiophene). An investigation by X-ray absorption and X-ray photoelectron spectroscopy, *Chem. Phys.*, **1995**, *194*, 207–213.

[33] M. Dietrich; J. Heinze; G. Heywang; F. Jonas; Electrochemical and spectroscopic characterization of polyalkylenedioxythiophenes, *J. Electroanal. Chem.*, **1994**, *369*, 87–92.

[34] Bayer AG; *European Patent*, **1993**, *533671.*

[35] Bayer AG; *European Patent*, **1995**, *686662.*

[36] F. Jonas; G. Heywang; Technical applications for conductive polymers, *Electrochim. Acta*, **1994**, *39*, 1345–1347.

[37] F. Jonas; J.T. Morrison; 3,4-polyethylenedioxythiophene (PEDT): Conductive coatings technical applications and properties, *Synth. Met.*, **1997**, *85*, 1397–1398.

[38] J. Ouyang; C.-W. Chu; F.-C. Chen; Q. Xu; Y. Yang; High-Conductivity Poly(3,4-Ethylenedioxythiophene):Poly(styrenesulfonate) film and its application in polymer optoelectronic devices, *Adv. Funct. Mater.*, **2005**, *15*, 203–208.

[39] M. X. Chen; Printed electrochemical devices using conducting polymers as active materials on flexible substrates, *Proc. IEEE*, **2005**, *93*, 1339–1347.

[40] Q. Peng; Z. Y. Lu; Y. Huang; M. G. Xie; D. Xiao; D. C. Zou; Novel light-emitting polymers derived from fluorene and maleimide, *J. Mater. Chem.*, **2003**, *13*, 1570–1574.

[41] D. Chirvase; Z. Chiguvare; M. Knipper; J. Parisi; V. Dyakonov; J. C. Hummelen; Temperature dependent characteristics of poly(3 hexylthiophene)-fullerene based heterojunction organic solar cells, *J. App. Phys.*, **2003**, *93*, 3376–3383.

[42] H. Rost; J. Ficker; J. S. Alonso; L. Leenders; L. McCulloch; Air-stable all-polymer field-effect transistors with organic electrodes, *Synth. Met.*, **2004**, *145*, 83–85.

[43] Y. Cao; A. Andreatta; A. J. Heeger; P. Smith; Influence of chemical polymerization conditions on the properties of polyaniline, *Polymer*, **1989**, *30*, 2305–2311.

[44] N. Kuramoto; A. Tomita; Chemical oxidative polymerization of dodecylbenzenesulfonic acid aniline salt in chloroform, *Synth. Met.*, **1997**, *88*, 147–151.

[45] M. R. Gandhi; P. Murray; G. M. Spinks; G. G. Wallace; Mechanism of electromechanical actuation in polypyrrole, *Synth. Met.*, **1995**, *73*, 247–256.

[46] K. Okabayashi; F. Goto; K. Abe; T. Yoshida; Electrochemical studies of polyaniline and its application, *Synth. Met.*, **1987**, *18*, 365–370.

[47] R. H. Baughman; Conducting polymer artificial muscles, *Synth. Met.*, **1996**, *78*, 339–353.

[48] S. Chao; M. S. Wrighton; Characterization of a solid-state polyaniline-based transistor: water vapor dependent characteristics of a device employing a poly(vinyl alcohol)/phosphoric acid solid-state electrolyte, *J. Am. Chem. Soc.*, **1987**, *109*, 6627–6631.

[49] D. Nilsson; T. Kugler; P. Svensson; M. Berggren; An all-organic sensor-transistor based on a novel electrochemical transducer concept printed electrochemical sensors on paper, *Sens. Actuators B*, **2002**, *86*, 193–197.

[50] Z. Zhu; J. T. Mabeck; C. Zhu; N. C. Cady; C. A. Batt; G. G. Malliaras; A simple poly(3,4-ethylene dioxythiophene)/poly(styrene sulfonic acid) transistor for glucose sensing at neutral pH, *Chem. Commun.*, **2004**, pages 1556–1557.

[51] K. Krishnamoorthy; R. S. Gokhale; A. Q. Contractor; A. Kumar; Novel label-free DNA sensors based on poly(3,4-ethylenedioxythiophene, *Chem. Commun.*, **2004**, pages 820–821.

[52] D. A. Bernards; G. G. Malliaras; G. E. S. Toombes; S. M. Gruner; Gating of an organic transistor through a bilayer lipid membrane with ion channels, *Appl. Phys. Lett.*, **2006**, *89*.

[53] J. Lu; N. J. Pinto; A. G. MacDiarmid; Apparent dependence of conductivity of a conductiong polymer on an electric field in a field effect transistor configuration, *J. Appl. Phys.*, **2002**, *92*, 6033–6038.

[54] A. J. Epstein; F.-C. Hsu; N.-R. Chiou; V. N. Prigodin; Electric-field induced ion-leveraged metal-insulaton transition in conducting polymer-based field effect devices, *Curr. Appl. Phys.*, **2002**, *2*, 339–343.

[55] D. Nilsson; M. Chen; T. Kugler; T. Remonen; M. Armgarth; M. Berggren; Bi-stable and dynamic current modulation in electrochemical organic transistors, *Adv. Mater.*, **2002**, *14*, 51–54.

[56] M. Chen; D. Nilsson; T. Kugler; M. Berggren; T. Remonen; Electric current rectification by an all-organic electrochemical device, *Appl. Phys. Lett.*, **2002**, *81*, 2011–2013.

[57] M. Abidian; D. Kim; D. C. Martin; Conducting-Polymer nanotubes for controlled drug release, *Adv. Mater.*, **2006**, *18*, 405–409.

[58] J. Yang; K. Lipkin; D. C. Martin; Electrochemical fabrication of conducting polymer poly(3,4-ethylenedioxythiophene) (PEDOT) nanofibrils on microfabricated neural prosthetic devices, *J. Biomater. Sci. Polymer Edn.*, **2007**, *18*, 1075–1089.

[59] X. Cui; J. F. Hetke; J. A. Wiler; D. J. Anderson; D. C. Martin; Electrochemical deposition and characterization of conducting polymer polypyrrole/PSS on multichannel neural probes, *Sens. Actuators, B*, **2001**, *93*, 8–18.

[60] K. Hyodo; Electrochromism of conducting polymers, *Electrochim. Acta.*, **1994**, *39*, 265–272.

[61] M.-A. De Paoli; G. Casalbore-Miceli; E. M. Girotto; W. A. Gazotti; All polymeric solid state electrochromic devices, *Electrochim. Acta.*, **1999**, *44*, 2983–2991.

[62] P. Somani; A. B. Mandale; S. Radhakrishnan; Study and development of conducting polymer-based electrochromic display devices, *Acta. Mater.*, **2000**, *48*, 2859–2871.

[63] C. Arbizzani; A. Bongini; M. Mastragostino; A. Zanelli; G. Barbarella; M. Zambianchi; Polyalkylthiophenes as electrochromic materials: A comparative study of poly(3-methylthiophenes) and poly(3-hexylthiophenes), *Adv. Mater.*, **1995**, *7*, 571–574.

[64] S. A. Sapp; G. A. Sotzing; J. R. Reynolds; High contrast ratio and fast-switching dual polymer electrochromic devices, *Chem. Mater.*, **1998**, *10*, 2101–2108.

[65] W. Stoeckenius; Bacterial rhodopsins: Evolution of a mechanistic model for the ion pumps, *Protein Sci.*, **1999**, *8*, 447–459.

[66] R. R. Birge; Nature of the primary photochemical events in rhodopsin and bacteriorhodopsin, *Biochim. Biophys. Acta*, **1990**, *1016*, 293–327.

[67] U. Haupts; J. Tittor; D. Oesterhelt; Closing in on bacteriohrodopsin: Progress in understanding the molecule, *Annu. Rev. Biophys. Biomol. Struct.*, **1999**, *28*, 367–399.

[68] N. Grigorieff; T. A. Ceska; K. H. Downing; J. M. Baldwin; R. Henderson; Electron-crystallographic refinement of the structure of bacteriorhodopsin, *J. Mol. Biol.*, **1996**, *259*, 393–421.

[69] H. Luecke; B. Schobert; H.-T. Richter; J.-P. Cartailler; J. K. Lanyi; Structure of bacteriorhodopsin at 1.55 A resolution, *J. Mol. Biol.*, **1999**, *291*, 899–911.

[70] J. K. Lanyi; Molecular mechanism of ion transport in bacteriorhodopsin: Insights from crystallographic, spectroscopic, kinetic and mutational studies, *J. Phys. Chem. B*, **2000**, *104*, 11441–11448.

[71] H. Trissl; Photoelectric measurements of purple membranes, *Photochem. Photobiol.*, **1990**, *51*, 793–818.

[72] A. Maeda; Photoelectric measurements of purple membranes, *Israel J. Chem.*, **1995**, *35*, 387–818.

[73] T. Althaus; W. Eisfeld; R. Lohrmann; M. Stockburger; Photoelectric measurements of purple membranes, *Israel J. Chem.*, **1995**, *35*, 227–818.

[74] L. Zheng; J. Herzfeld; NMR studies of retinal proteins, *J. Bioenerg. Biomembr.*, **1992**, *24*, 139–146.

[75] A. Albeck; N. Friedman; M. Sheves; M. Ottolenghi; Role of retinal isomerizations and rotations in the photocycle of bacteriorhodopsin, *J. Am. Chem. Soc.*, **1986**, *108*, 4614–4618.

[76] J. M. Fang; J. D. Carriker; V. Balogh-Nair; K. Nakanishi; Evidence for the necessity of double bond (13-ene) isomerization in the proton pumping of bacteriorhodopsin, *Photochem. Photobiol.*, **1983**, *105*, 5162–5164.

[77] B. Honig; T. Ebrey; R. H. Callender; U. Dinur; M. Ottolenghi; Photoisomerization, energy storage, and charge separation: A model for light energy transduction in visual pigments and bacteriorhodopsin, *Proc. Natl. Acad. Sci. USA*, **1979**, *76*, 2503–2507.

[78] N. B. Gillespie; K. J. Wise; L. Ren; J. A. Stuart; D. L. Marcy; J. Hillebrecht; Q. Li; L. Ramos; K. Jordan; S. Fyvie; R. R. Birge; Characterization of the branched-photocycle intermediates P and Q of bacteriorhodopsin, *J. Phys. Chem. B*, **2002**, *106*, 13352–13361.

[79] A. Der; L. Keszthelyi, Eds., *Bioelectronic applications of photochromic pigments;* NATO Science Series: Life Sciences, IOS, Amsterdam.

[80] L. Keszthelyi; P. Ormos; Electric signals associated with the photocycle of bacteriorhodopsin, *FEBS Lett.*, **1980**, *109*, 189–193.

[81] L. Keszthelyi; P. Ormos; Displacement current on purple membrane fragments oriented in a suspension, *Biophys. Chem.*, **1983**, *18*, 397–405.

[82] M. Holz; M. Lindau; M. P. Heyn; Distributed kinetics of the charge movements in bacteriorhodopsin, *Biophys. J.*, **1988**, *53*, 623–933.

[83] S. Y. Liu; Light-induced currents from oriented purple membrane, *Biophys. J.*, **1990**, *57*, 943–950.

[84] H.-W. Trissl; The concept of chemical capacitance, *Biophys. J.*, **1987**, *52*, 141.

[85] P. Ormos; S. Hristova; L. Keszthelyi; The effect of pH on proton transport by bacteriorhodopsin, *Biochim. Biophys. Acta*, **1985**, *809*, 181–186.

[86] S. Y. Liu; T. G. Ebrey; Photocurrent measurements of the purple membrane oriented in a polyacrylamide gel, *Biophys. J.*, **1988**, *54*, 321–329.

[87] F. Boucher; S.G. Taneva; S. Elouatik; M. Dery; S. Messaoudi; E. Harvey-Girard; N. Beaudoin; Reversible inhibition of proton release activity and the anesthetic-induced acid-base equilibrium between the 480 and 570 nm forms of bacteriorhodopsin, *Biophys. J.*, **1996**, *70*, 948–961.

[88] J.-P. Wang; S.-K. Yoo; L. Song; M. A. El-Sayed; Molecular mechanism of the differential photoelectric response of bacteriorhodopsin, *J. Phys. Chem. B*, **1997**, *101*, 3420–3423.

[89] J.-P. Wang; L. Song; S.-K. Yoo; M. A. El-Sayed; A comparison of the photoelectric current responses resulting from the proton pumping process of bacteriorhodopsin under pulsed and CW laser excitations, *J. Phys. Chem. B*, **1997**, *101*, 10599–10604.

[90] K. Koyama; N. Yamaguchi; T. Miyasaka; Antibody-mediated bacteriorhodopsin orientation for molecular device architectures, *Science*, **1994**, *265*, 762–765.

[91] K. Koyama; N. Yamaguchi; T. Miyasaka; Molecular organization of bacterio-rhodopsin films in optoelectronic devices, *Adv. Mater.*, **1995**, *7*, 590–594.

[92] B. Robertson; E. P. Lukashev; Rapid pH change due to bacteriorhodopsin measured with a tin-oxide electrode, *Biophys. J.*, **1995**, *68*, 1507–1517.

[93] J.-A. He; L. Samuelson; L. Li; J. Kumar; S. K. Tripathy; Bacteriorhodopsin thin film assemblies, immobilization, properties and applications, *Adv. Mater.*, **1999**, *11*, 435–446.

[94] T. Dyukova; B. Robertson; H. Weetall; Optical and electrical characterization of bacteriorhodopsin films, *Biosystems*, **1997**, *41*, 91–98.

[95] T. Miyasaka; K. Koyama; Rectified photocurrents from purple membrane Langmuir-Blodgett films at the electrode-electrolyte interface, *Thin Solid Films*, **1992**, *210*, 146–149.

[96] L. Keszthelyi; Orientation of membrane fragments by electric field, *Biochim. Biophys. Acta*, **1980**, *598*, 429–436.

[97] R. A. Brizzolara; A method for patterning purple membrane using self-assembled monolayers, *Biosystems*, **1995**, *35*, 131–140.

[98] J.-A. He; L. Samuelson; L. Li; J. Kumar; S. K. Tripathy; Oriented bacteriorhodopsin/polycation multilayers by electrostatic layer-by-layer assembly, *Langmuir*, **1998**, *14*, 1674–1679.

[99] L. M. Ellerby; J. S. Cohan; B. Dunn; M. A. El-Sayed; J. S. Valentine; J. I. Zink S. Wu; Bacteriorhodopsin encapsulated in transparent sol-gel glass: a new biomaterial, *Chem. Mater.*, **1993**, *5*, 115–120.

[100] Z. Chen; A. Lewis; H. Takei; I. Nebenzahl; Bacteriorhodopsin oriented in polyvinyl alcohol films as an erasable optical storage medium, *Appl. Opt.*, **1991**, *30*, 5188–5196.

[101] R. Jonas; Y. Koutalos; T. G. Ebrey; Purple membrane: surface charge density and the multiple effect of pH and cations, *Photochem. Photobiol.*, **1990**, *52*, 1163–1177.

[102] Y. Kimura; M. Fujiwara; A. Ikegami; Anisotropic electric properties of purple membrane and their change during the photoreaction cycle, *Biophys. J.*, **1984**, *45*, 615–625.

[103] Y. Shen; C. R. Safinya; K. S. Liang; A. F. Ruppert; K. J. Rothschild; Stabilization of the membrane protein bacteriorhodopsin to 140 C in two-dimensional films, *Nature*, **1993**, *366*, 48–50.

[104] M. Born; E. Wolf, *Principles of Optics;* Cambridge University Press, Cambridge, 7^{th} ed., 1999.

[105] R. C. Dunn; Near-field scanning optical microscopy, *Chem. Rev.*, **1999**, *99*, 2891–2927.

[106] E. H. Synge; A suggested model for extending microscopic resolution into the ultra-microscopic region, *Philos. Mag.*, **1928**, *6*, 356–362.

[107] D. Pohl; Optical stethoscopy: Image recording with resolution $\lambda/20$, *Phil. Trans. R. Soc. Lond. A*, **2004**, *362*, 701–717.

[108] E. A. Ash; G. Nicholls; Super-resolution aperture scanning microscope, *Nature*, **1972**, *237*, 510–512.

[109] D. Pohl; W. Denk; M. Lanz; Optical stethoscopy: Image recording with resolution $\lambda/20$, *Appl. Phys. Lett.*, **1984**, *44*, 651–653.

[110] U. Drig; D. W. Pohl; F. Rohner; Near-field optical-scanning microscopy, *J. Appl. Phys.*, **1986**, *59*, 3318–3327.

[111] A. Drezet; M. J. Nasse; S. Huant; J. C. Woehl; The optical near-field of an aperture tip, *Europhys. Lett.,*, **2004**, *66*, 41–47.

[112] A. G. Manoj and K. S. Narayan; Voltage-controlled spectral tuning of photoelectric signals in a conducting polymer-bacteriorhodopsin device, *Appl. Phys. Lett.*, **2003**, *83*, 3614–3616.

[113] A. G. Manoj and K. S. Narayan; Opto-electrical processes in a conducting polymerbacteriorhodopsin system, *Biosens. Bioelectron.*, **2004**, *19*, 1067–1074.

[114] G. Decher; J. D. Hong; J. Schmitt; Buildup of ultrathin multilayer films by a self-assembly process: III. Consecutively alternating adsorption of anionic and cationic polyelectrolytes on charged surfaces, *Thin Solid Films*, **1992**, *210*, 831–835.

[115] J. T. Stricker; A. D. Gudmundsdottir; A. P. Smith; B. E. Taylor; M. F. Durstock; Fabrication of organic thin-film transistors using layer-by-layer assembly, *J. Phys. Chem B*, **2007**, *111*, 6322–6326.

[116] A. Der; L. Keszthelyi; Charge motion during the photocycle of bacteriorhodopsin, *Biochemistry (Moscow)*, **2001**, *66*, 1234–1248.

[117] F. T. Hong; Molecular Sensors based on photoelectric effect of bacteriorhodopsin: Origin of differential responsivity, *Mater. Sci. Eng., C)*, **1997**, *4*, 267–285.

[118] J. Xua; P. Bhattacharya; G. Varo; Monolithically integrated bacteriorhodopsin/semiconductor opto-electronic integrated circuit for a biophotoreceiver, *Biosens. Bioelectron.*, **2004**, *19*, 885–892.

[119] I. Lee; E. Greenbaum; S. Budy; J. R. Hillebrecht; R. R. Birge; J. A. Stuart; Photoinduced surface potential change of bacteriorhodopsin mutant D96N measured by scanning surface potential microscopy, *J. Phys. Chem. B*, **2006**, *110*, 10982–10990.

[120] Y. Jin; N. Friedman; M. Sheves; T. He; D. Cahen; Bacteriorhodopsin (bR) as an electronic conduction medium: Current transport through bR-containing monolayers, *Proc. Natl. Acad. Sci. U.S.A.*, **2006**, *103*, 8601–8606.

[121] S. K. M. Jonsson; J. Birgerson; X. Crispin; G. Greczynski; W. Osikowicz; A. W. Denier van der Gon; W. R. Saleneck; M. Fahlman; The effects of solvents on the morphology and sheet resistance in poly(3,4-ethylenedioxythiophene)polystyrenesulfonic acid (PEDOTPSS) films, *Synth. Met.*, **2003**, *139*, 1–10.

[122] Y. Haba; E. Segal; M. Narkis; G. I. Titelman; A. Seigmann; PolyanilineDBSA/polymer blends prepared via aqueous dispersions, *Synth. Met.*, **2000**, *110*, 189–193.

[123] M. G. Han; S. K. Cho; S. G. Oh; S. S. Im; Preparation and characterization of polyaniline nanoparticles synthesized from DBSA micellar solution, *Synth. Met.*, **2002**, *126*, 53–60.

[124] G. Varo; J. K. Lanyi; Distortions in the photocycle of bacteriorhodopsin at moderate dehydration, *Biophys. J.*, **1991**, *59*, 313–322.

[125] J. Heberle; J. Riesle; G. Thiedemann; D. Oesterhelt; N. A. Dencher; Proton migration along the membrane surface and retarded surface to bulk transfer, *Nature*, **1994**, *370*, 379–382.

[126] J. Heberle; N. A. Dencher; Surface-bound optical probes monitor protein translocation and surface potential changes during the bacteriorhodopsin photocycle, *Proc. Natl. Acad. Sci. U.S.A.*, **1992**, *89*, 5996–6000.

[127] S. Weiss; Flourescence spectroscopy of single biomolecules, *Science*, **1999**, *283*, 1676–1683.

[128] W. E. Moerner; M. Orrit; Illuminating single molecules in condensed matter, *Science*, **1999**, *283*, 1670–1676.

[129] A. Yildiz; J. N. Forkey; S. A. McKinney; T. Ha; Y. E. Goldman; P. R. Selvin; Myosin V walks hand-over-hand: Single fluorophore imaging with 1.5-nm localization, *Science*, **2003**, *300*, 2061–2065.

[130] E. Barkai; Y. Jung; R. Silbey; Theory of single-molecule spectroscopy: Beyond the ensemble average, *Annu. Rev. Phys. Chem.*, **2004**, *55*, 457–507.

[131] A. Janshoff; M. Neitzert; Y. Oberdorfer; H. Fuchs; Force spectroscopy of molecular systems - Single molecule spectroscopy of polymers and biomolecules, *Angew. Chem. Int. Ed.*, **2000**, *39*, 3213–3237.

[132] E. Betzig; R. J. Chichester; Single molecules observed by near-field scanning optical microscopy, *Science*, **1993**, *262*, 1422–1425.

[133] T. He; N. Friedman; D. Cahen; M. Sheves; Bacteriorhodopsin monolayers for optoelectronics: orientation and photoelectric response on solid supports, *Adv. Mater.*, **2005**, *17*, 1023–1027.

[134] J. H. Cheung; W. B. Stockton; M. F. Rubner; Molecular-level processing of conjugated polymers. 3. Layer-by-layer manipulation of polyaniline via electrostatic interactions, *Macromolecules*, **1997**, *30*, 2712–2716.

[135] I. Horcas; R. Fernndez; J. M. Gomez-Rodrguez; J. Colchero; J. Gomez-Herrero; A. M. Baro; WS×M: A software for scanning probe microscopy and a tool for nanotechnology, *Rev. Sci. Instrum.*, **2007**, *78*, 013705.

[136] D. J. Muller; H-J. Sass; S. A. Muller; G. Buldt; A. Engel; Surface structures of native bacteriorhodopsin depend on the molecular packing arrangement in the membrane, *J. Mol. Biol.*, **1999**, *285*, 1903–1909.

[137] R. Henderson; J. M. Baldwin; T. A. Ceska; F. Zemlin; E. Beckmann; K. H. Downing; Model for the structure of bacteriorhodopsin based on high-resolution electron cryo-microscopy, *J. Mol. Biol.*, **1990**, *213*, 899–929.

[138] L. Novotny and B. Hecht, *Principles of Nano-optics.;* University Press, Cambridge, 2006.

[139] H. Kuzmany, *Solid-state Spectroscopy an Introduction.;* Springer-Verlag, Berlin, 1998.

[140] A. S. Ulrich; A. Watts; I. Wallat; M. P. Heyn; Distorted Ssructure of the retinal chromophore in bacteriorhodopsin resolved by 2H-NMR, *Biochemistry*, **1994**, *33*, 5370–5375.

[141] S. W. Lin; R. A. Mathies; Orientation of the protonated retinal Schiff base group in bacteriorhodopsin from absorption linear dichroism, *Biophys. J.*, **1989**, *56*, 653–660.

[142] J. A. Veerman; M. F. Garcia-Parajo; L. Kuiper; N. F. Van Hulst; Single molecule mapping of the optical field distribution of probes for near-field microscopy, *J. Microsc.*, **1998**, *194*, 477–482.

[143] D. Courjon; C. Bainier; Near field microscopy and near field optics, *Rep. Prog. Phys.*, **1994**, *57*, 989–1028.

[144] L. Zimanyi; Analysis of the bacteriorhodopsin photocycle by singular value decomposition with self-modeling: A critical evaluation using reaslistic simulated data, *J. Phys. Chem. B*, **2004**, *104*, 7183–7192.

[145] D. Oesterhelt; B. Hess; Reversible photolysis of the purple complex in the purple membrane of Halobacterium halobium, *Eur. J. Biochem.*, **1973**, *37*, 316–326.

[146] N. Hampp; C. Brauchle; D. Oesterhelt; Bacteriorhodopsin wildtype and variant aspartate-96→aspargine as reversible holographic media, *Biophys. J.*, **1990**, *58*, 83–93.

[147] A. Seitz; N. Hampp; Kinetic optimization of bacteriorhodopsin films for holographic interferometry, *J. Phys. Chem. B*, **2000**, *104*, 7183–7192.

[148] K. Ohno; R. Govindjee; T. G. Ebrey; Blue light effect on the proton pumping by bacteriorhodopsin, *Biophys. J.*, **1983**, *43*, 251–254.

[149] C. Girard; O. L. F. Martin; A. Dereux; Molecular lifetime changes induced by nanometer scale optical fields, *Phys. Rev. Lett.*, **1995**, *75*, 3098–3101.

[150] N. Hampp; Bacteriorhodopsin as a photochromic retinal protein for optical memories, *Chem. Rev.*, **2000**, *100*, 1755–1776.

[151] R. Govindjee; S. P. Balashov; T. G. Ebrey; Quantum efficiency of the photochemical cycle of bacteriorhodopsin, *Biophys. J.*, **1990**, *58*, 597–608.

[152] B. Hecht; H. Bielefeldt; D. W. Pohl; L. Novotny; H. Heinzelmann; Influence of detection conditions on near-field optical imaging, *J. Appl. Phys.*, **1998**, *84*, 5873–5882.

[153] B. Hecht; H. Bielefeldt; Y. Inouye; D. W. Pohl; L. Novotny; Facts and artifacts in near-field optical microscopy, *J. Appl. Phys.*, **1997**, *81*, 2492–2498.

[154] B. Hecht; B. Sick; U. P. Wild; V. Deckert; R. Zenobi; O. J. F. Martin; D. W. Pohl; Scanning near-field optical microscopy with aperture probes; Fundamentals and applications, *J. Chem. Phys.*, **2000**, *112*, 7761–7774.

[155] N. Arun; K. S. Narayan; Monitoring intermediate states of bacteriorhodopsin monolayers using near-field optical microscopy, *Submitted*.

[156] N. Arun; K. S. Narayan; Conducting polymers as antennas for probing biophysical activities, *J. Phys. Chem. B*, **2008**, *112*, 1564–1569.

[157] A. J. Epstein; J. M. Ginder; F. Zuo; R. W. Bigelow; H. S. Woo; D. B. Tanner; A. F. Richter; W. S. Huang; A. G. MacDiarmid; Insulator-to-metal transition in Polyaniline, *Synth. Met.*, **1987**, *18*, 303–309.

[158] G. Reiter; Dewetting of thin polymer films, *Phys. Rev. Lett.*, **1992**, *68*, 75–78.

[159] A. Oron; S. H. Davis; S. G. Bankof; Long-scale evolution of thin liquid films, *Rev. Mod. Phys.*, **1997**, *69*, 931–980.

[160] R. Xie; A. Karim; J. F. Douglas; C. C. Han; R. A. Weiss; Spinodal dewetting of thin polymer films, *Phys. Rev. Lett.*, **1998**, *81*, 1251–1254.

[161] A. Sharma; R. Khanna; Pattern formation in unstable thin liquid films, *Phys. Rev. Lett.*, **1998**, *81*, 3463–3466.

[162] U. Thiele; M. G. Velarde; K. Neuffer; Dewetting: film rupture by nucleation in the spinodal regime, *Phys. Rev. Lett.*, **2001**, *87*, 016104.

[163] R. Seemann; H. Mantz; K. Jacobs; K. R. Mecke; R. Blossey J. Becker; G. Grun; Complex dewetting scenarios captured by thin-film models, *Nat. Mater.*, **2003**, *2*, 59–63.

[164] S. Y. Chou; L. Zhuang; L. Guo; Lithographically induced self-construction of polymer microstructures for resistless patterning, *Appl. Phys. Lett.*, **1999**, *75*, 1004–1006.

[165] A. Sehgal; V. Ferreiro; J. F. Douglas; E. J. Amis; A. Karim; Pattern-directed dewetting of ultrathin polymer films, *Langmuir*, **2002**, *18*, 7041–7048.

[166] E. Schaffer; T. Thurn-Albrechet; T. P. Russell; U. Steiner; Electrically induced structure formation and pattern transfer, *Langmuir*, **2000**, *403*, 874–877.

[167] E. Voicu; E. Schffer; Z. Lin; T. P. Russell; U. Steiner M. D. Morariu; N; Hierarchical structure formation and pattern replication induced by an electric field, *Nat. Mater*, **2003**, *2*, 48–52.

[168] N. Wu; L. F. Pease III; W. B. Russel; Toward large-scale alignment of electrohydrodynamic patterning of thin polymer films, *Adv. Funct. Mater*, **2006**, *16*, 1992–1999.

[169] N. E. Voicu; S. Harkema; U. Steiner; Electric-field-induced pattern morphologies in thin liquid films, *Adv. Funct. Mater*, **2006**, *16*, 926–934.

[170] A. Ghatak; M. K. Chaudhury; V. B. Shenoy; A. Sharma; Meniscus instability in a thin elastic film, *Phys. Rev. Lett.*, **2000**, *85*, 4329–4332.

[171] V. B. Shenoy; A. Sharma; Pattern formation in a thin solid film with interactions, *Phys. Rev. Lett.*, **2001**, *86*, 119–1122.

[172] W. Monch; S. Herminghaus; Elastic instability of rubber films between solid bodies, *Europhys. Lett.*, **2001**, *53*, 525–531.

[173] E. Schaffer; T. Thurn-Albrecht; T. P. Russell; U. Steiner; Electrohydrodynamic instabilities in polymer films, *Europhys. Lett.*, **2001**, *53*, 518–524.

[174] J. W. Swan; Stress and other effects produced in resin and in a viscid compound of resin and oil by electrification, *Proc. R. Soc. (Lond.)*, **1897**, *62*, 38–46.

[175] A. Vrij; Possible mechanism for the spontaneous rupture of thin, free liquid films, *Discuss. Faraday Soc.*, **1966**, *42*, 23–33.

[176] M. C. Cross; P. C. Hohenberg; Pattern formation outside of equilibrium, *Rev. Mod. Phys.*, **1993**, *65*, 851–1112.

[177] V. B. Shenoy; A. Sharma; Stability of a thin elastic film interacting with a contactor, *J. Mech. Phys. Solids*, **2002**, *50*, 1155–1173.

[178] J. Sarkar; V. B. Shenoy; A. Sharma; Patterns, forces, and metastable pathways in debonding of elastic films, *Phys. Rev. Lett.*, **2004**, *93*, 018302.

[179] N. Arun; J. Sarkar; A. Sharma; V. B. Shenoy; K. S. Narayan; Electric-field induced morphological transitions in elastic contact instability of soft solid films, *J. of Adh.*, **2007**, *83*, 513–534.

[180] D. J. Griffiths, *Introduction to Electrodynamics;* Prentice-Hall, Englewood Cliffs, NJ, 3^{rd} ed.

[181] J. R. Melcher, *Field-Coupled Surface Waves;* MIT Press, Cambridge MA, 1963.

[182] S. Harkema; U. Steiner; Hierarchical patterns formation in thin polymer films using an electric field and vapor sorption, *Adv. Funct. Mater.*, **2005**, *15*, 2016–2020.

[183] N. Arun; A. Sharma; P. S. G. Pattader; I. Banerjee; H. M. Dixit; K. S. Narayan; Electric field induced patterns in soft visco-elastic films: From long waves of viscous liquids to short waves of elastic solids, *Phys. Rev. Lett.*, **2009**, *102*, 254502.

[184] N. Arun; A. Sharma; V. Shenoy; K. S. Narayan; Electric-field-controlled surface instabilities in soft elastic films, *Adv. Mater.*, **2006**, *18*, 660–663.

[185] V. B. Shenoy; A. Sharma; Surface instability of soft films with coupled tension-shear interactions, *J. Appl. Phy.*, **2003**, *94*, 6376–6385.

[186] J. Nase; A. Lindner; C. Creton; Pattern formation during deformation of a confined viscoelastic layer: From a viscous liquid to a soft elastic solid, *Phys. Rev. Lett.*, **2008**, *101*, 074503.

[187] J. Sarkar; A. Sharma; V. B. Shenoy; Electric-field induced instabilities and morphological phase transitions in soft elastic films, *Phys. Rev. E*, **2008**, *77*, 031604.

[188] M. Bag; D. Gupta; N. Arun; K. S. Narayan; Deformation of metallic liquid drop by electric field for contacts in molecular -organic electronics, *Proc. R. Soc. A*, **2009**, *465*, 1799–1808.